

FY17 Report for Instrumentation Development for the Transient Testing Program

C. Jensen, K. Condie, N. Woolstenhulme,
T. Unruh, E. Larsen, R. Skifton, P. Calderoni,
J. Svoboda (retired)
Idaho National Laboratory

A. Fleming, Z. Hua, H. Ban
University of Pittsburgh

M. Reichenberger, J. Roberts, M. Harrison, D.
Nichols, W. Fu, K. Kellogg, J. Hewitt, D. McGregor
Kansas State University

September 2017

The INL is a U.S. Department of Energy National Laboratory
operated by Battelle Energy Alliance



DISCLAIMER

This information was prepared as an account of work sponsored by an agency of the U.S. Government. Neither the U.S. Government nor any agency thereof, nor any of their employees, makes any warranty, expressed or implied, or assumes any legal liability or responsibility for the accuracy, completeness, or usefulness, of any information, apparatus, product, or process disclosed, or represents that its use would not infringe privately owned rights. References herein to any specific commercial product, process, or service by trade name, trade mark, manufacturer, or otherwise, does not necessarily constitute or imply its endorsement, recommendation, or favoring by the U.S. Government or any agency thereof. The views and opinions of authors expressed herein do not necessarily state or reflect those of the U.S. Government or any agency thereof.

FY17 Report for Instrumentation Development for the Transient Testing Program

**C. Jensen, K. Condie, N. Woolstenhulme, T. Unruh,
E. Larsen, R. Skifton, P. Calderoni, J. Svoboda (retired)**
Idaho National Laboratory

A. Fleming, Z. Hua, H. Ban
University of Pittsburgh

**M. Reichenberger, J. Roberts, M. Harrison, D. Nichols,
W. Fu, K. Kellogg, J. Hewitt, D. McGregor**
Kansas State University

**September 2017
Idaho National Laboratory
Idaho Falls, Idaho 83415**

<http://www.inl.gov>

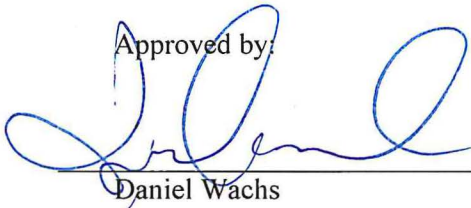
**Prepared for the
U.S. Department of Energy
Office of NA
Under DOE Idaho Operations Office
Contract DE-AC07-05ID14517**

FY17 Report for Instrumentation Development for the Transient Testing Program

INL/EXT-17-43444

September 2017

Approved by:



Daniel Wachs

National Technical Director for Transient Testing

9/28/17

Date

FOREWORD

This report details the technical activities and accomplishment carried out under the in-pile instrumentation work package supporting the transient testing program. These activities were performed in direct support of cross-cutting transient testing experiment objectives. The purpose of this report is to provide a complete summary of all work, which is of particular interest to nuclear irradiation test experimenters and in-pile instrumentation engineers with emphasis on transient testing applications. Development activities are focused on devices to perform online measurement of neutron flux, temperature, and mechanical behaviors in nuclear fuels experiments. A brief summary of activities and accomplishments is first provided for each major activity. Detailed reports are presented in appendices.

CONTENTS

| | |
|--|----|
| FOREWORD | v |
| 1. Technical Summary of FY17 Activities | 1 |
| 1.1 Neutron Flux/Energy Deposition – Micro-Pocket Fission Detector <i>INL-KSU</i> | 1 |
| 1.2 Temperature – Infrared Thermography – <i>INL-Pitt</i> | 2 |
| 1.3 Temperature – Cladding Thermocouples – INL | 2 |
| 1.4 Mechanical Behavior (Coolant Dynamics) – Boiling Detector – INL | 3 |
| Appendix A - Micro-Pocket Fission Detector Development for TREAT Experiments | A1 |
| Appendix B – Infrared Pyrometry Development for TREAT Experiments | B1 |
| Appendix C – Development of a Custom Infrared Pyrometer System for TREAT Experiments | C1 |
| Appendix D – Cladding Thermocouples for Transient Irradiation Experiments | D1 |
| Appendix E – Development of an In-Pile Boiling Detector System Based on Measurement of Electrical Impedance | E1 |

FY17 Report for Instrumentation Development for the Transient Testing Program

1. Technical Summary of FY17 Activities

With the resumption of transient testing at the Transient Reactor Test (TREAT) facility at Idaho National Laboratory (INL), a full recovery and cutting-edge transient testing capability also requires a well-coordinated and innovative instrumentation development and qualification program to support future objectives^a. With this goal, the fuel safety research program is actively pursuing the Research, Development, and Demonstration (RD&D) of several cross-cutting, advanced instrument technologies to meet near-term experiment programmatic goals while establishing the base measurement capabilities (state-of-the-art) for next-generation experimentation. As part of these efforts, two key university partnerships have been formed with Kansas State University (KSU) and the University of Pittsburgh (UPitt). Brief summaries of FY17 accomplishments follow for each primary activity follows. Detailed reports for each activity are provided in the appendices.

1.1 Neutron Flux/Energy Deposition – Micro-Pocket Fission Detector *INL-KSU*

The Micro-Pocket Fission Detector (MPFD) is a potentially high impact instrument that can measure online, local neutron flux in the TREAT reactor, a challenge that few instruments can meet. The goal of this activity is to adapt and develop the MPFD for TREAT applications with a particular focus on surviving and measuring peak flux levels in TREAT. See Appendix A for a detailed report of all activities.

- The results of survivability testing and simulations indicate the modifications to the MPFD sensor design are likely necessary to prevent sensor failure from fission-fragment heating in maximum TREAT flux levels. Additional experimental data from irradiation of highly enriched MPFD samples at the KSU TRIGA reactor and from natural uranium MPFD samples deployed at TREAT will help to confirm this conclusion.
- A calibration plan for the MPFD has been developed based on techniques employed by CEA of France and a preliminary calibration attempt was performed. The calibration process is expected to evolve to suit needs. A detailed MPFD model has been created using Geant4 and used to estimate the MPFD response in a TREAT-like spectrum.
- Current-mode electronics were developed to support high flux measurement in TREAT. Prototype electronics have been received at KSU and are undergoing testing.

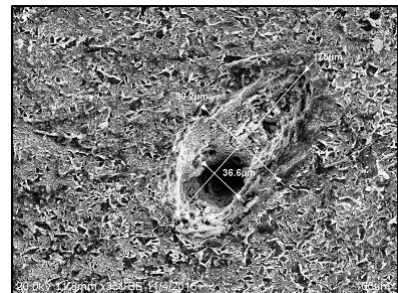


Figure 1. Post-pulse SEM image of the defect in the uranium coating.

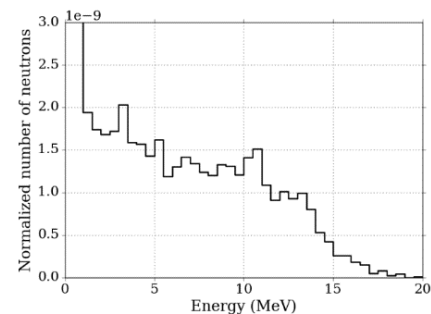


Figure 2. Predicted MPFD pulse-height distribution generated using Geant4.

^a C.B. Jensen, "Strategic Plan for Instrumentation Development and Qualification for the Transient Testing Program," INL/LTD-17-43144, August 2017.

1.2 Temperature – Infrared Thermography – INL-Pitt

Infrared (IR) pyrometry offers non-contact, high-temperature, and fast time response capability for temperature measurement on cladding surfaces, representing a leap beyond current state-of-the-art approaches using thermocouples to reduce measurement uncertainties. The specific goals of this activity are to: (1) experimentally explore and potentially qualify customized commercial pyrometer systems for in-pile use at INL including both active and passive systems, and (2) Design, build, and test a custom pyrometer device with enhanced features for in-pile applications including a response time of < 1 ms. See Appendices B and C for a detailed report of all activities at INL and Pitt, respectively.

- An optical fiber line including feedthrough has been fabricated and successfully tested for transmitting infrared radiation through high pressure boundaries at high temperatures.
- The detailed calibration procedure for customized commercial active pyrometer system has been well-defined to enable needed adaption for experiment installation. A design of experiments setup was built to support all testing of pyrometer systems. A study for the active pyrometer was performed finding high sensitivity to alignment for a given calibration and defined sensitivity ranges for alignment requirements. The active pyrometer demonstrated capability to measure emissivity changes in the target.
- Blackbody furnace testing capability was installed along with optical fiber end processing capability at HTTL. A passive commercial pyrometer system has been procured and is ready for evaluation to compare performance with the active pyrometer.
- Custom pyrometer design uses lock-in signal processing in a novel fashion to provide improved signal-to-noise ratio with < 1 ms response time. Proof-of-concept experimental studies have shown the feasibility of the approach to progress to the next stages of complete system prototype setup and testing.

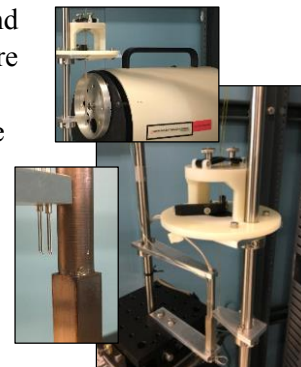


Figure 3. (Top) Blackbody furnace installed for calibration (Left) Sapphire IR collection and target surface; (Right) Additive manufactured test stand for characterization studies.

1.3 Temperature – Cladding Thermocouples – INL

Thermocouple measurements of cladding surface temperature represents state-of-the-art for transient testing applications, however, INL currently lacks experience with welding thermocouples to cladding materials. The activity has the goal of determining the ideal approach to attaching thermocouples to Zr-based claddings. See Appendix C for a detailed report of all activities.

- The ideal configuration for pool water conditions for fast transient testing was determined to be 0.005” sized thermocouple wire welded to the cladding surface to form an integral junction with the cladding.
- Thermocouple junctions were formed using precision laser welding for joining 0.005” Type K thermocouple wire and testing showed good performance of lead wires and junctions at Pressurized Water Reactor (PWR) water conditions. Special consideration for thermocouple-Zr material compatibility was found to be an issue requiring further detailed exploration.

1.4 Mechanical Behavior (Coolant Dynamics) – Boiling Detector – INL

An impedance-based measurement for detecting phase change in water (boiling detector) has been developed to help address uncertainties for transient boiling, along with the IR pyrometer. The goal for this activity is to qualify a sensor design to measure coolant phase change in PWR conditions in TREAT with emphasis on film boiling void structure and boiling event timing. See Appendix D for a detailed report of all activities.

- A complete boiling detector system has been developed and nearly^b qualified for deployment in in-pile measurement in a PWR water capsule. The system includes sensor, electrical circuit design and setup, and data acquisition and processing software that will interface with the TREAT experiment DAS
- An electrically insulating coating was discovered that has been tested and performed well in PWR conditions to enhance detection capabilities.
- A unique high-speed imaging station has been built and utilized to perform a design of experiments study to characterize the performance of the sensor related to RIA boiling needs. Results show that the sensor is most sensitive to the presence of void of the parameters studied with good sensitivity to a film boiling void geometry. Sensor response has been tested to show expected response times better than < 1 ms.

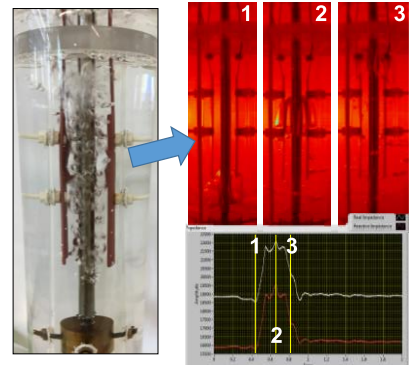


Figure 4. (Left) Boiling in the high speed visual boiling setup; (Right) Results for measured impedance and corresponding images showing bubble propagation

^b In-pile testing in TREAT required to establish performance in radiation environment

Appendix A

Micro-Pocket Fission Detector Development for TREAT Experiments

2017 Annual Report

M. Reichenberger, J. Roberts, M. Harrison, D. Nichols,
W. Fu, K. Kellogg, J. Hewitt, D. McGregor

*Semiconductor Materials and Radiological Technologies Laboratory
Kansas State University*

Table of Contents

| | | |
|-------|---|----|
| 1. | Summary of MPFD Sensor Development Efforts | 1 |
| 2. | Estimate of TREAT MPFD Survivability | 1 |
| 2.1 | MPFD Fissile Material Evaluation at Kansas State University | 2 |
| 2.1.1 | MPFD Sample Substrate Fabrication..... | 2 |
| 2.1.2 | Sample Irradiation and Post-Irradiation Examination..... | 3 |
| 2.1.3 | Preparation for Pulse Testing of 93% Enriched MPFD Samples..... | 5 |
| 2.1.4 | Modeling MPFD Substrate Heating..... | 7 |
| 2.2 | MPFD Samples for IGR/TREAT Irradiation..... | 8 |
| 3. | Sensor Calibration and Predictive Model | 9 |
| 3.1 | MPFD Calibration Plan..... | 10 |
| 3.2 | Calibration Test in Piercing Beam Port at the KSU TRIGA Mk. II Reactor | 12 |
| 4. | Sensor Design Refinements and Optimization..... | 14 |
| 5. | Detector Electronics | 15 |
| 6. | Achievements and Future Outcomes | 16 |
| 7. | Appendices | 16 |
| 7.1 | Appendix A – Current TREAT MPFD Design..... | 16 |
| 7.2 | Appendix B – Summary of Relevant MPFD Projects..... | 17 |
| 7.2.1 | NEUP (NEET) Enhanced Micro-Pocket Fission Detector (MPFD) for High Temperature Reactors (INL, KSU, CEA) | 17 |
| 7.2.2 | NEUP (NEAMS) A Transient Reactor Physics Experiment with High Fidelity 3-D Flux Measurements for Verification and Validation (KSU) | 17 |
| 7.2.3 | NEUP IRP Advanced Instrumentation for Transient Reactor Testing (UW, ISU, KSU, OSU, INL, CEA) | 17 |
| 7.2.4 | NEUP IRP Computational & Experimental Benchmarking for Transient Fuel Testing (OSU, UMich, MIT, TerraPower, HTTP, ORNL, ANL, INL) | 18 |
| 7.2.5 | DOE NEET TREAT Baseline Instrumentation Development (INL)..... | 18 |
| 7.2.6 | US-ROK INERI Radiation Hardened Readout Circuit Design for High Temperature Micro-Pocket Fission Detectors Operating in Harsh Environments (INL, KAERI, KAIST, Sejong University) | 18 |
| 7.2.7 | SBIR Advanced Manufacturing of Micro-Pocket Fission Detector (MPFD)..... | 18 |
| 7.3 | Appendix C – Schedule of Important TREAT-MPFD Related Dates | 19 |
| 7.4 | Appendix D – Schematics..... | 20 |
| 8. | References | 22 |

1. Summary of MPFD Sensor Development Efforts

Micro-Pocket Fission Detectors (MPFDs) offer a unique opportunity to measure neutron flux within the Transient REActor Test (TREAT) facility at Idaho National Laboratory (INL). The extreme environment of TREAT experiments present several challenges that inhibit instrument deployment. The design of MPFDs includes characteristics that make them well-suited for applications at TREAT, including:

- Fast, real-time detection of neutron a flux;
- Robust design for high pressure and high temperature resistance;
- Compact design allowing for multiple sensors in a compact design and relatively unobtrusive implementation;
- Flexibility to tune material design to measure different neutron spectra and flux magnitudes.

However, opportunities exist to predict and improve the behavior of MPFD sensors in TREAT experiments. Research has been initiated to develop MPFD technologies for initial deployment and continued optimization for in-core neutron flux measurements at TREAT. During the first year of research, particular focus has been given to general detector development supporting ongoing deployments, electronics development, and enhanced production capabilities. Additional research included investigations on the survivability of MPFDs in high flux environments and characterization methods for MPFDs.

Experimental and modeling efforts have provided valuable insight into the energy deposition of fission fragments in MPFDs. These results are being used to evaluate temperature thresholds for sensors that are part of present deployment efforts, and to improve the design of sensors in the future.

Calibration methods under development to provide quantifiable flux data and associated uncertainties from the MPFDs measurements. The calibration process will include both modeling and experimental components still under development. Preliminary experimental calibration has not produced acceptable results due to sensor malfunctions. Absolute and relative calibration methods will be used to improve the quality of the measured data provided by MPFDs in the future.

An electronic support system has been developed for use with MPFD arrays of up to 4 channels. The system supports both pulse-mode and current-mode operation for low- and high-flux applications respectively. In the past, stand-alone NIM modules were used to operate prototypical MPFDs. The design and fabrication of an off-the-shelf electronics support system greatly enhanced the deployment of MPFDs at TREAT and other facilities. Software was also developed to provide an interface between the MPFD user and electronics support system.

All of the lessons of the present work are being used to improve the MPFD design for future deployments. New materials are under investigation to help mitigate the effects of fission fragment energy deposition. Calibration processes are continually improving the quality of data generated from MPFDs. Finally, improvements to the electronic support system are accelerating characterization efforts and enabling innovation to occur at a much faster pace than in the past by providing a sturdy foundation from which to conduct experiments with these developmental sensors.

2. Estimate of TREAT MPFD Survivability

The TREAT reactor is designed to generate large transient fluxes for a variety of irradiation testing experiments. Peak powers generated during short pulses approach 20 GW with a neutron flux of approximately 10^{17} n·cm⁻²·s⁻¹. Real-time monitoring of these unique core conditions during transient operations can be accomplished with MPFDs. However, the high fluxes associated with the pulses in the TREAT core present thermodynamic concerns given the amount of energy released within MPFDs in such a short amount of time.

MPFDs operate on the principle of measuring the ionization of fission fragments in the gas chamber of the detector, illustrated in Fig. 2.1. However, only one fission fragment enters into the gas chamber, the other being emitted in the opposite direction, into the fissile layer and metallic substrate. If each fission that occurs in an MPFD results in a fission fragment energy deposition of 85 MeV in the substrate on average, and assuming each MPFD has approximately 0.5 ug of natural uranium deposited on it, a 100 ms long pulse in the TREAT reactor at $10^{17} \text{ n} \cdot \text{cm}^{-2} \cdot \text{s}^{-1}$ flux will produce approximately 4.6×10^6 fissions in an MPFD, depositing $6.3 \times 10^{-5} \text{ J}$ of energy in the substrate over a 100 ms duration, sufficient to heat and melt the entire uranium layer many times over.

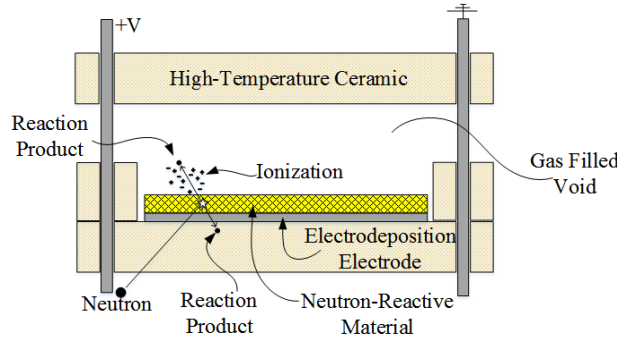


Fig. 2.1 One fission fragment deposits energy into the substrate materials after each fission, heating the substrate at high interaction rates.

The previous estimate makes several simplifying assumptions and neglects heat transfer so it is not yet clear if this large energy deposition will have an adverse effect on detector performance. However, the rapid heating could be detrimental to the integrity of the MPFD fissile material deposition.

2.1 MPFD Fissile Material Evaluation at Kansas State University

Five MPFD substrate samples were prepared, pre-analyzed and then subjected to a pulse in the central thimble of the K-State TRIGA Mark II reactor to a peak power of 1.58 GW to study how these layers are effected by large transient neutron fluxes. After being allowed to decay to safer radiation levels, the sample substrates and coatings were inspected by scanning electron microscope (SEM) to identify any changes to their surface morphology.

2.1.1 MPFD Sample Substrate Fabrication

MPFD fabrication began with alumina wafers sent out for micro-machining and polishing. Upon return, a 50 Å titanium layer was evaporated onto the unmasked surfaces, followed by a 500 Å layer of platinum. Five samples were randomly selected from the larger batch of samples following metals deposition and uranium deposition via electrodeposition. This was performed by dissolving uranyl nitrate in ammonium nitrate, and then applying an alternating negative bias to the metal electrode of the alumina substrate of the MPFD [1]. Monitoring the current over time provided a means by which to monitor total deposition of uranium onto the platinum surface. As the amount of material increased, the resistance also increased, thus lowering the current, as illustrated in Fig. 2.2. These electrodepositions resulted in a layer of approximately 0.5 µg of natural uranium onto an MPFD, according to alpha-particle counting results.

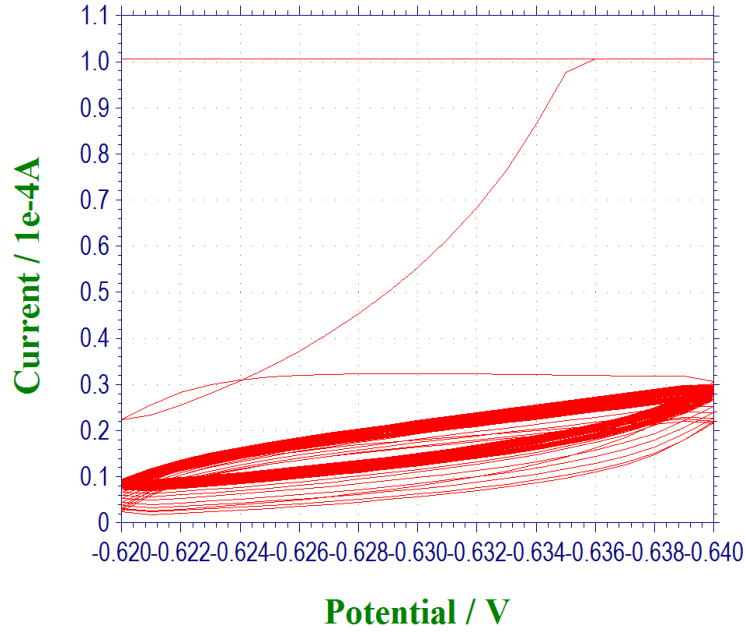


Fig. 2.2 Example I/V plot of an electrodeposition. This plot taken for Sample #3 in this study

Once electrodeposition had been completed for all samples, the samples were dried and inspected in the scanning electron microscope (SEM), illustrated in Figure 1.2 and 1.3, and x-ray fluorimeter (XRF) to observe composition spatially. Finally, the alpha-particle activity for each sample was counted for several hours in an alpha-particle counting chamber to quantify the uranium mass.

2.1.2 Sample Irradiation and Post-Irradiation Examination

The five MPFD fissile material substrates were then packaged in plastic bags and inserted into the central thimble of the K-State TRIGA Mark II nuclear reactor. The reactor was pulsed to a peak power of 1.58 GW corresponding to a peak neutron flux of approximately $1.5 \times 10^{17} \text{ n} \cdot \text{cm}^{-2} \cdot \text{s}^{-1}$ (based on a linear extrapolation of the total neutron flux of $2.3 \times 10^{13} \text{ n} \cdot \text{cm}^{-2} \cdot \text{s}^{-1}$ the KSU TRIGA reactor at 250 kWth). The samples were removed from the central thimble and after decaying to a safer handling level of activity, the samples were assayed with a HPGe and found to be emitting primarily ^{72}Ga activity. The samples were then re-imaged in the SEM to determine whether any surface morphology changes had occurred from the pulse, illustrated in Figure 1.4. Post-pulse analysis disclosed that surface features were altered by the pulse. The most obvious and compelling evidence was found in a large defect on Sample 1, roughly 160 μm in length, shown Fig. 2.3.

Table 1. Deposited uranium mass estimates as given by alpha-particle counting experiments.

| Sample | Sample alpha-particle activity (Ci) | Uranium mass estimate (μg) | Error (%) |
|--------|---------------------------------------|---|-----------|
| 1 | $5.97\text{E-}13 \pm 2.02\text{E-}14$ | 0.84 ± 0.03 | 3.38 |
| 2 | $2.78\text{E-}13 \pm 1.05\text{E-}14$ | 0.39 ± 0.01 | 3.79 |
| 3 | $3.57\text{E-}14 \pm 4.16\text{E-}15$ | 0.05 ± 0.01 | 11.63 |
| 4 | $2.67\text{E-}13 \pm 1.22\text{E-}14$ | 0.38 ± 0.02 | 4.58 |
| 5 | $3.29\text{E-}13 \pm 1.17\text{E-}14$ | 0.46 ± 0.02 | 3.56 |

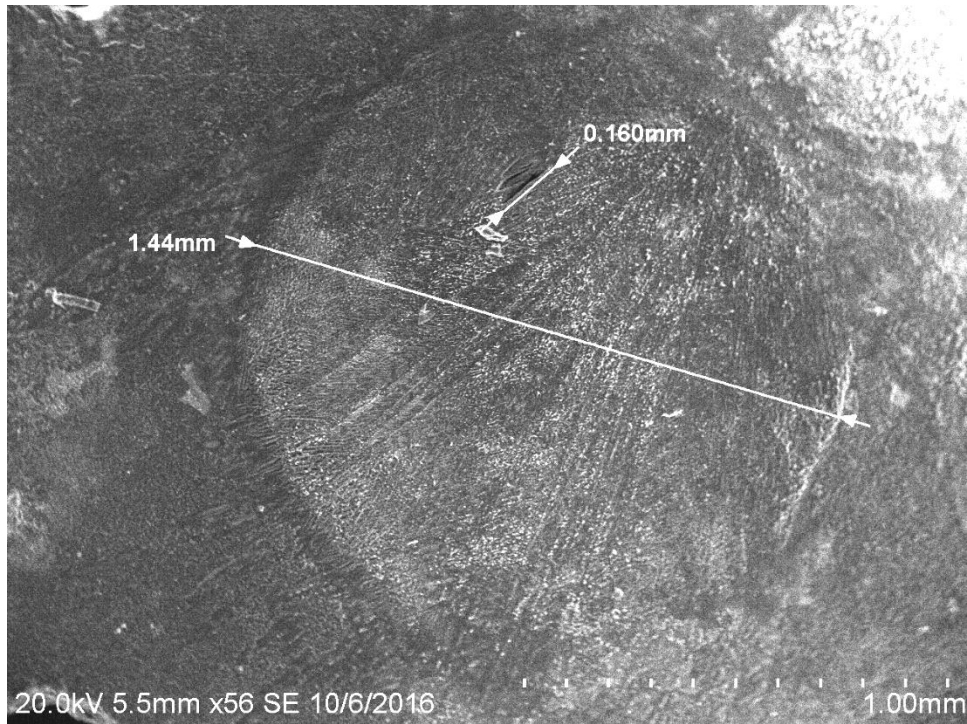


Fig. 2.3 Pre-pulse SEM image of the uranium coating of Sample 1.

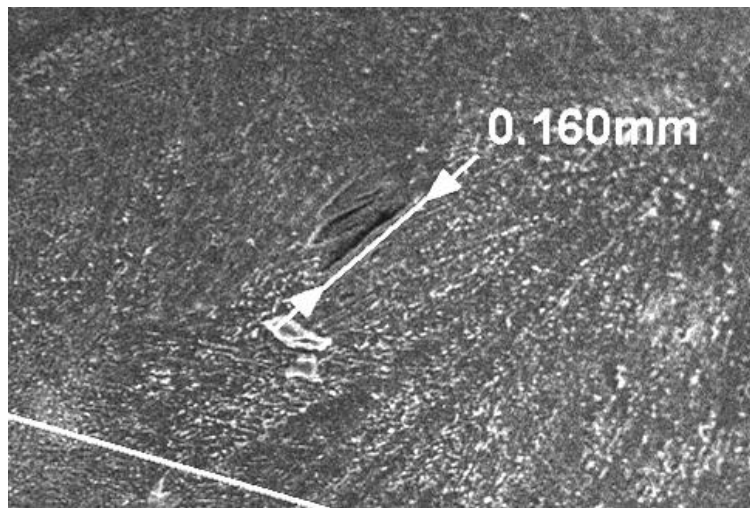


Fig. 2.4 Enlargement of the defect in Fig. 2.3.

The same defect is shown post-pulse in Fig. 2.5. Note that the thin layers that appear to bridge over the hole in Fig. 2.4 appear to now have melted down into the hole of the alumina substrate. XRF analysis of this defect and others like it was attempted, but with no reliable results to report. The geometry of these holes impedes reliable x-ray collection, thus making quantitative analysis of the composition of the materials within these defects quite difficult.

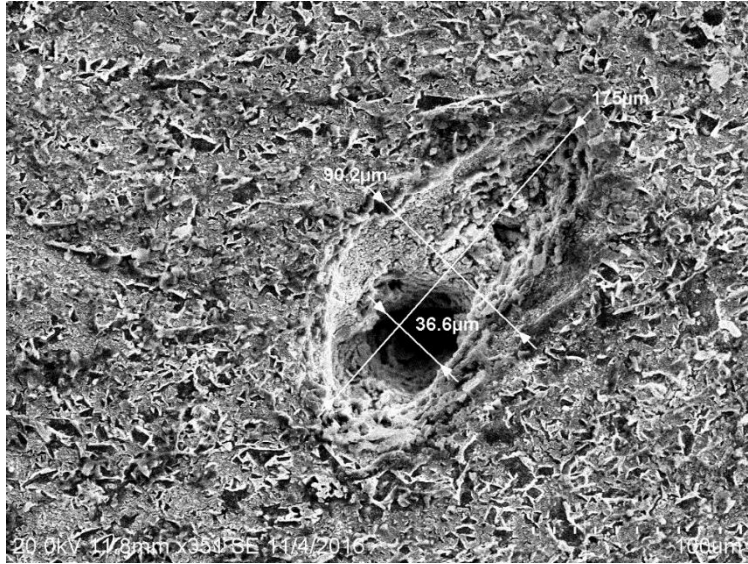


Fig. 2.5 Post-pulse SEM image of the defect in the uranium coating of Sample 1.

Regions in which no underlying substrate defects were present did not change in appearance. The key conclusion to be drawn from this study is that substrate defects can cause titanium/platinum melting during periods of high neutron fluxes. This is a direct result following from one or both causes: (1) additional local deposition of uranium at the defect caused by higher electric fields near the defect geometry which results in increased local fission rates and higher localized heat production and (2) the overhanging volumes of titanium/platinum are partially thermally removed from the bulk, decreasing their ability to rapidly carry away heat deposited by fission fragments. As such, it is important that MPFD substrates are carefully inspected for defects before electrodeposition. Any substrate found to have a defect compromising the planar uniformity of the deposition field should be removed from the batch. This approach should reduce and perhaps eliminate the micro-melt due to the flux transients.

While the approach described above addresses the concerns for TRIGA-type pulses, it is important to note the differences between TRIGA and TREAT transients. Flux magnitudes are higher in TREAT and are sustained for a longer period of time than a TRIGA transient which presents considerable concerns for the integrity of MPFDs. Computation simulation is recommended for first order approximation to determine how MPFDs might react in such an environment. Alternatively, MPFD samples were prepared with more sensitive fissile depositions to increase the fission rate during a TRIGA pulse.

2.1.3 Preparation for Pulse Testing of 93% Enriched MPFD Samples

Other research at KSU made available 93% enriched uranyl nitrate which was used to electrodeposit five MPFD sample substrates. Irradiation of highly enriched MPFD samples increases the fission rate in the sample because of the larger cross-section of the material compared to the natural uranium used for other MPFD deployments. This increase in fission rate acts to simulate the higher flux that MPFDs will experience during a TREAT pulse compared to a TRIGA pulse at KSU. The samples were evaporated with 1.5-mm diameter 50Å/500Å titanium/platinum electrodes by electron beam evaporation. Then, electrodeposition was used to deposit the fissile material for each sample [1]. Alpha-particle spectrometry was used to measure the fissile mass for each sample, summarized in Table 2. The specific activity of 93% enriched uranium of 7.0 E-5 Ci/g was used to calculate the mass of fissile material after measuring the activity of each sample [2].

Table 2. Alpha-particle spectrometry was used to measure the mass of fissile material on each MPFD disk sample for TRIGA testing.

| Sample | Activity (Ci) | Fissile Mass (g) | Error (%) |
|---------------|------------------------------------|------------------------------------|-----------|
| NEAMS.PROD.78 | $3.43\text{E-}11 \pm 1\text{E-}13$ | $0.49 \text{ E-}6 \pm 2\text{E-}9$ | 0.4 |
| NEAMS.PROD.73 | $8.13\text{E-}11 \pm 2\text{E-}13$ | $1.16\text{E-}6 \pm 3\text{E-}9$ | 0.3 |
| NEAMS.PROD.60 | $1.89\text{E-}11 \pm 5\text{E-}14$ | $0.27\text{E-}6 \pm 0.7\text{E-}9$ | 0.3 |
| NEAMS.PROD.39 | $4.21\text{E-}11 \pm 2\text{E-}13$ | $6.01\text{E-}7 \pm 2\text{E-}9$ | 0.4 |
| NEAMS.PROD.51 | $7.41\text{E-}11 \pm 1\text{E-}13$ | $1.06\text{E-}6 \pm 1\text{E-}9$ | 0.1 |

Five MPFD samples with HEU depositions were extracted from the process and chosen to be studied in depth to better estimate the damaging effects one might expect from in-core TREAT reactor use. The chosen samples had visible surface defects in the substrates and non-uniform uranium depositions and were selected based on the observations discussed in section 2.1.2. Each sample was inspected and carefully recorded in an SEM followed by XRD imaging to determine uranium distribution. Generally, uranium deposition was found to be thickest near electrode edges, confirming the earlier hypothesis that electrode edges would cause greater electric fields, thereby increasing uranium deposition rates. These samples were then sent to INL for 3D surface mapping shown in Fig. 2.6 and Fig. 2.7. These samples will be tested in a similar manner to the previously irradiation MPFD disks and examined for damage.

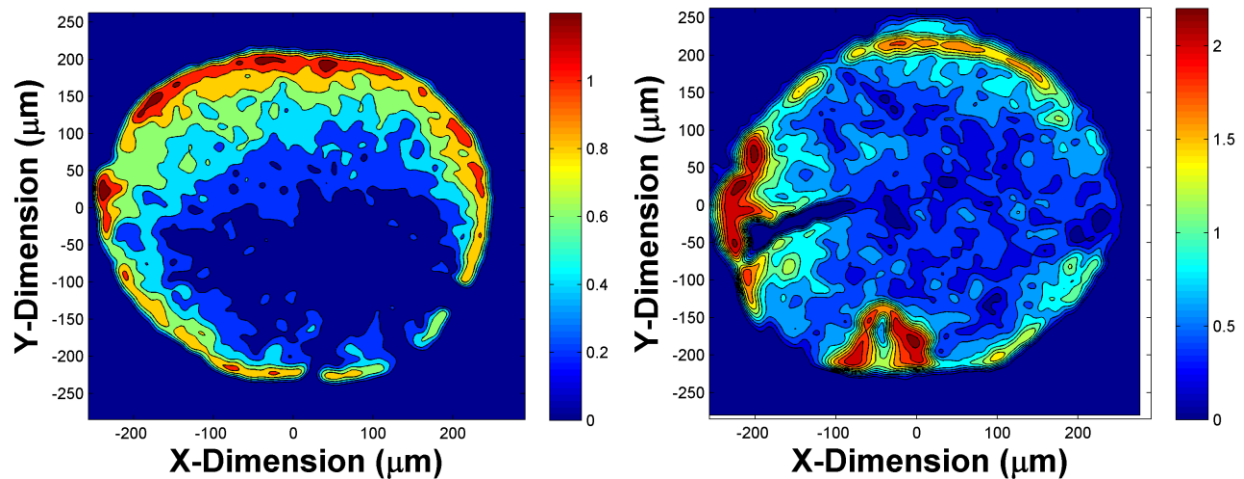


Fig. 2.6 Contour plots of relative uranium XRD signal strength across the surfaces of Samples 1 (left) and 2 (right). Sample 2 has a large substrate crack at the 8 o'clock to 9 o'clock position on its surface that can be seen in the plot.

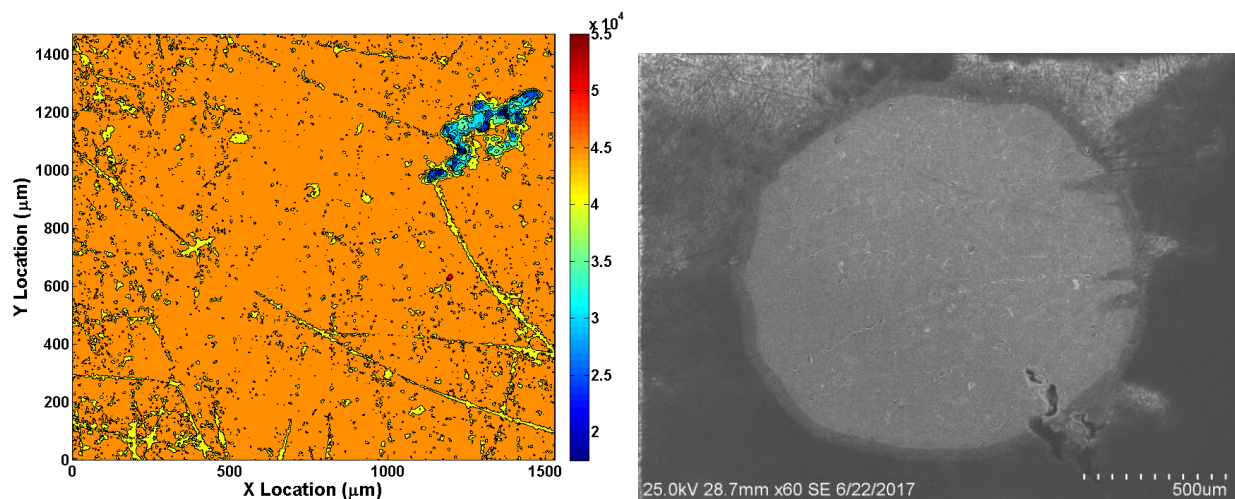


Fig. 2.7 Example surface map of Sample 3 (left) and its corresponding SEM image (right). Using the substrate crack in the bottom right of the SEM image, one can note that the orientation of the surface map is roughly 90 degrees rotated with respect to the SEM image.

2.1.4 Modeling MPFD Substrate Heating

The present version of the MPFD was computationally determined to generate too much heat to survive in-core application in the TREAT reactor. Simplified models of the heat generation and conduction processes in MPFDs during irradiation were developed using MATLAB. The development of the code was done in stages and checked for consistency along the way. First, the most probable pair of fission fragments (^{93}Sr and ^{140}Xe) were determined from known ^{235}U fission data, their initial kinetic energies were determined (100.53 MeV and 67.47 MeV respectively) and their differential energy loss curves determined using TRIM in each of the materials present in the MPFD construction; those being uranium oxide, platinum, titanium and aluminum oxide.

The XRD data and known uranium mass were utilized to estimate uranium oxide thickness across the surface. This was mapped into the voxelated volume to be simulated, along with the known Pt, Ti and Al_2O_3 geometries. Fissions were sampled throughout the uranium oxide volume and emission angles of the fission fragments sampled at random. The track of each fission fragment (FF) was computed, then energy deposition in each voxel along the tracks computed from FF chord length and which FF traversed the chord. Energy deposition calculations accounted for material type of the voxels and the entry energy of the FF. Total energy deposition distributions were computed for a large number of fissions, then normalized to be per fission.

In the next phase of simulation, the average energy deposition per fission distribution values were utilized as heat generation rates, scaled for current flux and detector efficiency values. The heat transfer portion of the simulation stepped through time, generating and conducting heat according to the flux profiles of the TRIGA and TREAT reactors. Conductivity and heat capacity values for each voxel are varied according to voxel material and temperature.

The heat transfer simulation was limited to conduction in solids only. Radiative heat losses at the surfaces were neglected as were phase changes. While radiative heat transfer becomes significant at high temperatures, the cavities within which the MPFD layers reside during a pulse are quite reflective and emissive due to their material of construction (Al_2O_3). This means that while significant quantities of heat would be emitted from the uranium oxide surface layer, nearly as much heat would be re-entering the surface due to reflection and re-emission by the cavity walls. The validity of this assumption is unconfirmed at this point and should be investigated in the future to determine if the simulation results will be affected.

Finally, since phase change (melting) is the phenomenon we seek to determine where and when it might occur, these occurrences are therefore considered the end point of the simulation. All results beyond the solid material reaching its melting point are certainly not invalid, but irrelevant.

Highly enriched uranium (93% ^{235}U) versions of the sample MPFDs as well as natural uranium (0.711% ^{235}U) and depleted uranium (0.22% ^{235}U) versions were simulated in TRIGA pulses and TREAT transients. It was found that all samples are expected to reach their melting points during a maximal TRIGA pulse as constructed with HEU. In fact, scaling the TRIGA pulse to 1% or even less of maximum was necessary to avoid melting. If constructed of natural uranium, the samples would most likely fully melt across their entire surface in a maximal TREAT pulse-transient, likely spawling material into their cavities. At present, the simplest solution to this problem appears to be the utilization of DU (depleted uranium) and scale down the deposited quantity of uranium in the construction of MPFDs for TREAT use. However, this option will reduce the sensitivity.

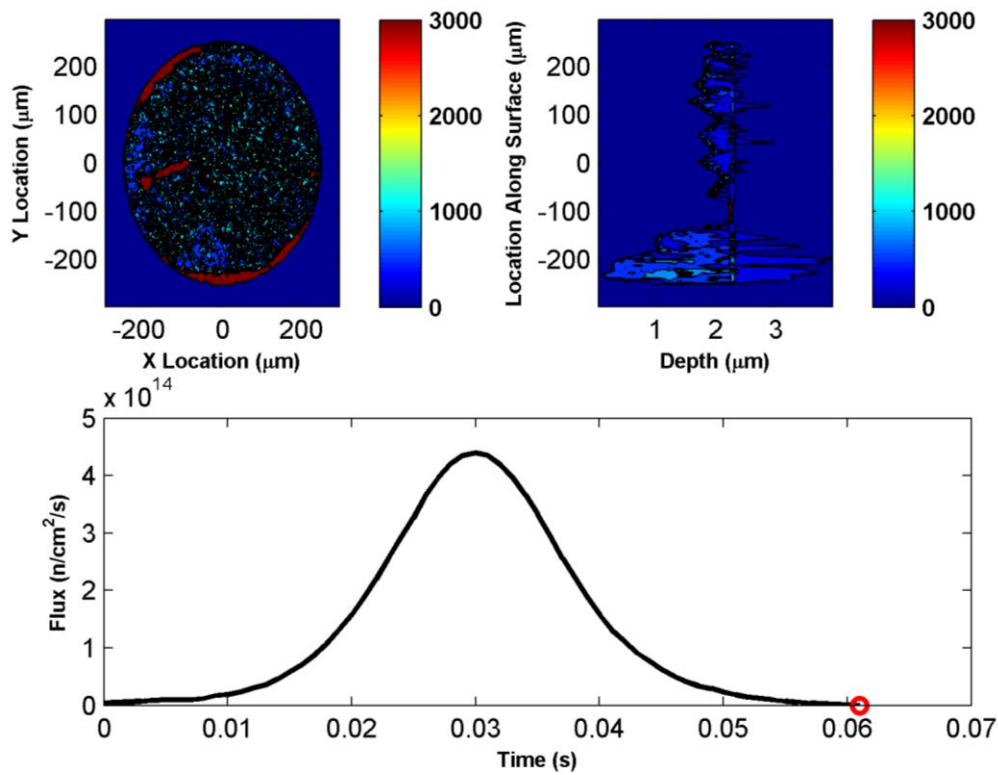


Fig. 2.8 Surface (upper left) and cross-sectional (upper right) contour plots of temperature after a 1% of maximum TRIGA pulse for Sample 1 as constructed with HEU. The bottom plot shows where in the pulse the two contour plots fit.

2.2 MPFD Samples for IGR/TREAT Irradiation

An opportunity to irradiate MPFD disks at the IGR reactor in Kazakhstan was also supported by this work. Four MPFD disks were identified as possible irradiation candidates. The four disks were previously evaporated and electrodeposited in a similar manner to the HEU disks, however natural uranium was used. Alpha-particle spectrometry was used to measure the activity of each MPFD sample, and a specific activity of $7.1 \text{ E-}7 \text{ Ci/g}$ was used to calculate the mass of fissile material deposited on each sample, summarized in

Table 3 [2]. The samples are being held until further instruction for potential IGR or TREAT pulsing is possible.

Table 3. Alpha-particle spectrometry was used to measure the mass of fissile material on each MPFD disk sample selected for possible IGR testing.

| Sample | Activity (Ci) | Fissile Mass (g) | Error (%) |
|---------------|------------------|------------------|-----------|
| NEAMS.PROD.4 | 6.02E-13 ± 9E-15 | 8.47E-7 ± 1.3E-8 | 1.50 |
| NEAMS.PROD.5 | 6.76E-13 ± 9E-15 | 9.52E-7 ± 1.3E-8 | 1.39 |
| NEAMS.PROD.7 | 6.33E-13± 9E-15 | 8.91E-7 ± 1.3E-8 | 1.46 |
| NEAMS.PROD.45 | 6.51E-13± 9E-15 | 9.18E-7 ± 1.3E-8 | 1.41 |

3. Sensor Calibration and Predictive Model

The successful deployment of MPFDs will require a combination of simulation via computational models and experimental measurements. Computational models can provide estimated sensitivities and methods to optimize geometries and reactants for particular applications. However, the measurements made by MPFDs must be of direct value for understanding the neutronic environment in TREAT. To connect an MPFD signal to an underlying physical quantity (e.g., a fission rate) requires calibration, and hence, a major effort has been initiated to developing and demonstrating a calibration plan for MPFDs.

Past work examined the response of MPFDs located within a Multi-State Environment Rodlet Transient Test Apparatus (Multi-SERTTA) deployed in the TREAT reactor [3]. The response of MPFDs loaded with various reactants was modeled using MCNP, with source terms defined via a multi-step process. The analysis confirmed that for the thin reactant layers characteristic of MPFDs, spatial self-shielding is negligible. The reactants considered included natural U, 93% enriched U, Th-232, and Pu-242. For the particular configuration modeled, the predicted sensitivity of MPFDs loaded with these reactants are summarized in Table 4 in both absolute and relative units. The latter (right column) is the expected fission rate per flux, per microgram of reactant.

Table 4 Simulated sensitivity of MPFDs with different coating materials.

| Material | Sensitivity (cm ²) | Sensitivity (cm ² / ug) |
|----------------|--------------------------------|------------------------------------|
| Natural U | 2.84 x 10 ⁻⁹ | 1.29 x 10 ⁻⁹ |
| 93% enriched U | 4.04 x 10 ⁻⁷ | 1.12 x 10 ⁻⁷ |
| Th-232 | 1.68 x 10 ⁻¹¹ | 4.65 x 10 ⁻¹² |
| Pu-242 | 7.69 x 10 ⁻¹⁰ | 2.06 x 10 ⁻¹⁰ |

As part of that same work, an initial study of the energy deposition by fission fragments in the MPFD gas pocket was performed, shown in Fig. 3.1.

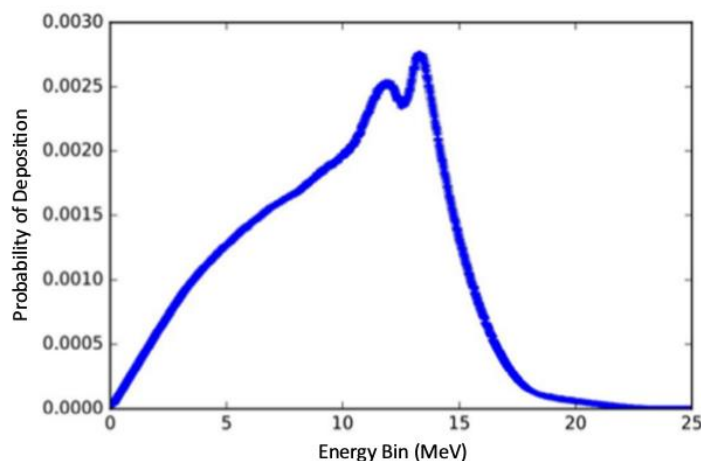


Fig. 3.1 Representative distribution of energy deposited by fission-fragments from previous simulation [3].

The distribution shown in Fig. 3.1 suggests that (1) a large amount of energy can be deposited in the chamber gas, and (2) only a small fraction of fragments deposit a small amount of energy and hence, a conservative discriminator setting may be used to filter background and electronic noise without significant signal losses. The ongoing work to model MPFDs focuses on three key topics:

- 1) Verifying past work with independent models
- 2) Predicting the response of MPFDs within a characteristic TREAT spectrum
- 3) Constructing a model for optimization of MPFD geometries and reactants

Presently, points (1) and (2) have been addressed.

3.1 MPFD Calibration Plan

To calibrate MPFDs, an absolute calibration technique used by CEA in France to calibrate sub-miniature fission chambers will be adopted. Absolute calibration is defined in terms of an effective mass:

$$m_{\text{eff}}(\text{LLD}) = C(\text{LLD})/R,$$

where C is the measured count rate (s^{-1}) at a particular lower-level discriminator setting LLD and R is the (true) fission rate per unit mass ($\text{s}^{-1}\text{g}^{-1}$). If m_{eff} is parameterized as a function of LLD, then the true fission rate can be determined in various environments. However, to determine R requires that the flux spectrum and magnitude is characterized precisely.

Because preliminary calibration will be performed at Kansas State University, the ideal environment for calibration is the KSU TRIGA Mark II reactor, which provides several in- and out-of- core locations for irradiation. Additional calibration at TREAT should be considered after a robust calibration method has been demonstrated at KSU.

A complete array of MPFDs will be calibrated simultaneously. First, a location will be selected, e.g., an existing flux-probe penetration in the reactor core or the penetrating beam port. Thereafter, a set of mock-up arrays loaded with various foils in place of the MPFD reactant will be irradiated for a given period under fixed conditions. The MPFD array to be calibrated will then be irradiated in the same location, with count rates measured as a function of LLD.

To determine the true fission rate, a spectrum-unfolding technique will be used. The activation foils to be deployed include Au-197 (with and without Cd), In-115 (with and without Cd), Al-27, and, potentially, Rh-103 and enriched U (with and without Cd). This selection of foils provides continuous coverage between 0.06 eV and 12.5 MeV. Part of the unfolding process will involve estimated the flux spectrum via

a computational model. A model of the KSU reactor exists and will be applied for this purpose. Past work used MCNP for modeling the response of MPFDs in various neutronic environments. Here, a complementary model was constructed using Geant4 based on the dimensions reported previously [3], illustrated in Fig. 3.2.

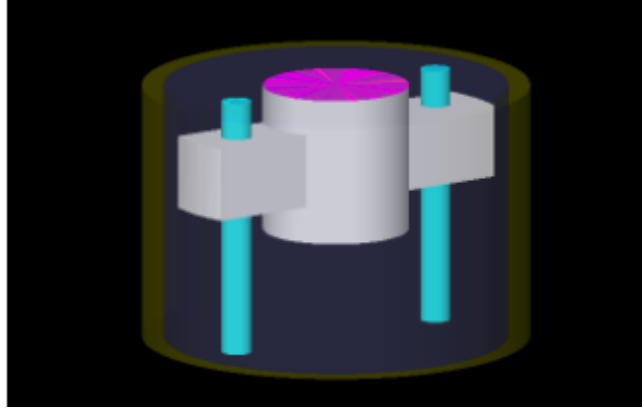


Fig. 3.2 Visualization of the Geant4 model used to estimate the MPFD response in a TREAT-like spectrum

To estimate the MPFD response in a TREAT-like spectrum (and, hence, to confirm previous results [3]) source spectrum was constructed based on the flux spectrum reported previously [3]. For simplicity, the neutron source was modeled as an isotropic planar source incident on the reactant layer. Of course, this is not equivalent to the source term present when embedded into the Multi-SERTTA vehicle (as was modeled previously [3]), but it provides at least a degree of confirmation.

The predicted pulse-height distribution, shown in Fig. 3.3, includes two features that warrant explanation relative to the spectrum shown in Fig. 3.1. First, the distribution in Fig. 3.3 does not vanish at the lowest channels. This may be explained by the fact the Geant4 model includes more physics than is believed to be accounted for in the MCNP6 model used to generate Fig. 3.1. An ongoing study aims to establish the precise cause of the discrepancy. Second, the overall magnitude of the distribution shown in Fig. 3.3 is much smaller than the spectrum in Fig. 3.1. This difference can be explained by the fact that the results of Fig. 3.3 are based on a *neutron* source rather than a fission-fragment source, and, hence, the overall sensitivity of the device to neutrons is built into the results. The lowest energy channel (which includes zero energy deposition) has a very large number of events because most neutrons do not lead to any energy deposition in the gas as they pass through the system without interacting, a consequence of the low sensitivity of MPFDs.

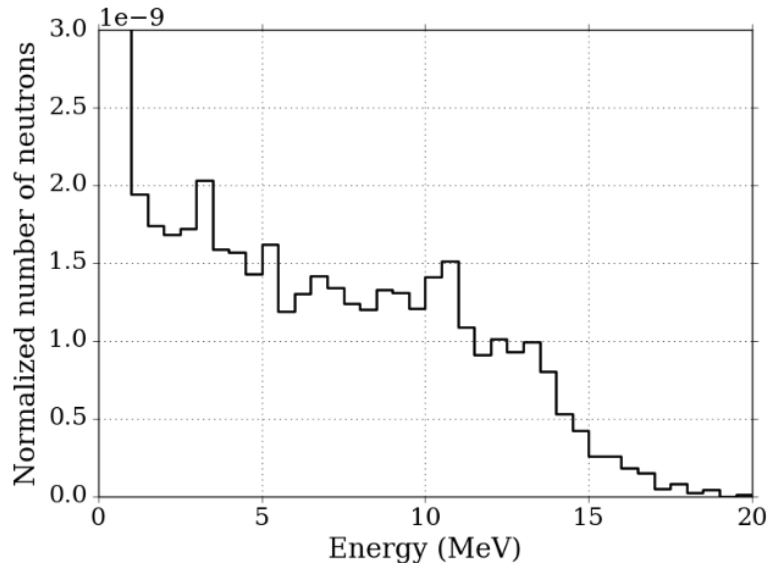


Fig. 3.3 Predicted MPFD pulse-height distribution generated using Geant4.

Future work will be performed to support deployment of the mock-up MPFDs and to analyze the results of foil activation. In addition, work will continue to develop the Geant4 model and to understand the various approximations made by its physical models.

3.2 Calibration Test in Piercing Beam Port at the KSU TRIGA Mk. II Reactor

A four-node MPFD calibration array was assembled with two MPFDs utilizing HEU and two utilizing natural uranium. The MPFD samples were selected from disks that were previously electrodeposited, and whose masses were close to one another based on alpha-particle spectrometry, summarized in Table 5. This test array was utilized to perform operational testing on the current-mode electronics (described in sec. 5) as well as for experimental validation of the piercing port model that predicted the response for each of the four nodes.

Table 5. Alpha-particle spectrometry was used to measure the mass of fissile material on each MPFD disk used to construct the first MPFD calibration array.

| Location | Material | Sample | Activity (Ci) | Fissile Mass (g) | Error (%) |
|------------|----------|---------------|--------------------------------------|------------------------------------|-----------|
| 3 (top) | 93% HEU | NEAMS.PROD.58 | $5.08\text{E-}11 \pm 0.8\text{E-}13$ | $7.25\text{E-}7 \pm 0.1\text{E-}8$ | 0.2 |
| 2 | Nat. U | NEAMS.PROD.12 | $5.70\text{E-}13 \pm 8\text{E-}15$ | $8.01\text{E-}7 \pm 1.2\text{E-}8$ | 1.5 |
| 1 | Nat. U | NEAMS.PROD.18 | $5.70\text{E-}13 \pm 8\text{E-}15$ | $8.03\text{E-}7 \pm 1.2\text{E-}8$ | 1.4 |
| 0 (bottom) | 93% HEU | NEAMS.PROD.72 | $5.15\text{E-}11 \pm 2\text{E-}13$ | $7.35\text{E-}7 \pm 0.3\text{E-}8$ | 0.3 |

Each of the four MPFDs were assembled with 1-cm spacing between each detector node. The MPFD nodes were centered about the ‘fuel region’ of the array when deployed in the grid-plate penetrations at the KSU TRIGA Mk. II research nuclear reactor. Therefore, the neutron flux experienced by all four MPFDs should be very similar for in-core testing where nodes with the same fissile coating are mirrored about the

central axial plane of the reactor. The location of each node with respect to the bottom on the MPFD array is summarized in Table 6.

Table 6. The location of each MPFD in the calibration test array was recorded relative from the bottom of the encapsulating tube, 1 cm spacing was maintained between nodes.

| Node | Location from bottom of tube (cm) |
|-------------|--|
| 3 | 36.86 |
| 2 | 35.86 |
| 1 | 34.86 |
| 0 | 33.86 |

Initially, an in-core position was to be used for the calibration test. However, during an initial deployment of the calibration array, erratic behavior was observed. Upon inspection of the array, it was determined that water had leaked into the array. The internals of the array were then dried at 100°C under rough vacuum for more than 24 hours before being re-filled with argon gas. The piercing beam port was then used to test the calibration method because it is a dry port to avoid issues with water leakage when testing in the reactor pool. The high-flux in the piercing beam port compared to other beam ports increased the expected interaction rate for each MPFD. Experimental determination of the neutron energy profile has been conducted for other research at KSU ([4] DE-NE0008305), enabling the calculation of the expected interaction rate for each MPFD in the calibration array with the reactor operated at 250 kWth, summarized in Table 7. The MPFD array was inserted 3 feet into the piercing beam port. After setting the electronic support system parameters (LLD: 200 mV, Bias: +400V, Gain: 5, Shaping Time: 0.25 μ s, BLR: 420 mV), the noise level was observed to peak at 40 mV and the pulsar (amplitude 1) yielded a 180 mV pulse. The reactor power was increased to 250 kWth for approximately 2.5 hours, neutron-induced pulses were observed, a pulse-height spectrum was collected from Ch. 0, and the count-rate was logged for all four channels. The neutron-induced pulse, shown in Fig. 3.4, is a typical example based on results from previous experiments.

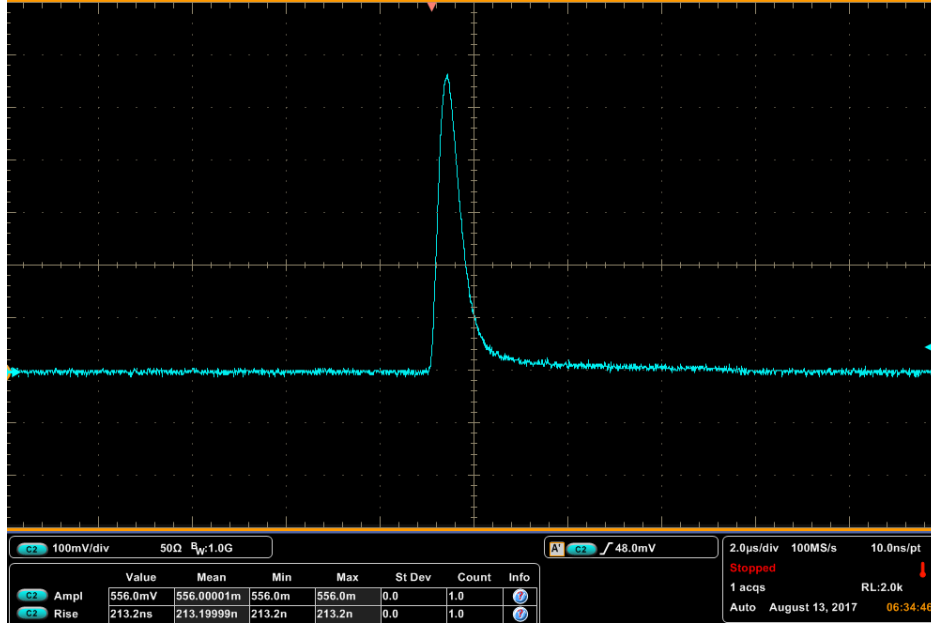


Fig. 3.4 Neutron-induced pulses were observed to have typical amplitude and shape compared to previous MPFD testing.

After collecting count rate data for all four channels throughout the entire irradiation period, the counts from each channel were summed (removing count spikes from noise) to determine the total number of counts during the experiment. The average count rate (cpm) was calculated by dividing the total number of counts by the total irradiation time from the first count, until the end of data collection (154 minutes). The data collected from this preliminary calibration attempt, summarized in Table 7, was inconclusive, but does suggest that there was damage to this particular MPFD test array. To determine if the array still functions properly, another test will be conducted wherein the array is deployed once again into the reactor core. The higher flux of the in-core position will then be used to determine if the relative response rate of each node corresponds to the expected relative count rate based on fissile mass.

Table 7. The interaction rate for each MPFD was calculated and compared to the experimental count rate in the piercing beam port (250.0 kWth reactor power).

| Node | Expected Interaction Rate (fpm) | Observed Count Rate (cpm) | Count Rate Error (cpm) |
|------|---------------------------------|---------------------------|------------------------|
| 3 | 145.41 ± 18.79 | 5.3 | 0.2 |
| 2 | 2.90 ± 0.33 | 63.8 | 0.6 |
| 1 | 3.33 ± 0.40 | 44.3 | 0.5 |
| 0 | 155.34 ± 19.84 | 120.7 | 0.9 |

4. Sensor Design Refinements and Optimization

The objectives of this and future work require the fabrication of numerous MPFD disks for testing survivability in high-flux environments and calibration experiments. The previous method for fabrication of disks and spacers used in the construction of MPFDs was prohibitively expensive on a per-unit basis. An effort was made to reduce the fabrication costs of MPFD components while also reducing the surface

roughness of the MPFD disks. Alumina wafers were sourced directly from Coors Tek Engineered Ceramics. Whole wafers were purchased at a discount compared to the unit cost incurred by previous fabrication methods. Additionally, superior polishing methods were employed by the supplier to yield a smoother surface finish. However, a lower purity alumina material (99.6% vs 99.9%) was required to meet the other fabrication demands. Ten 99.6% alumina, 4-in. diameter, 0.50-mm thick wafers were ordered to support the fabrication of additional disks and spacers for the continued efforts of this project.

Wafer-level processing enhances the quality and reduces fabrication time for MPFDs. Multiple alumina wafers can be evaporated with contacts before being sent to Synova, where a laser MicroJet system will be used to machine disks and spacers [5]. The disks will first be cut using the same geometry as the MPFDs which are planned for deployment. However, this system will enable the fabrication of enhanced disk and spacer designs. Therefore, modeling efforts are being conducted to determine if modifications to the MPFD geometry can be made to improve functionality of the sensors.

Other research of MPFD development at KSU indicates that a strong relationship exists between sensor functionality and fill gas pressure. A brief study of the impact of gas pressure on MPFD functionality is being conducted during the remaining period of performance of the present work, however a more in-depth study of this phenomenon should be considered to recommend gas pressure for upcoming deployments.

Although progress is being made to enhance the functionality and manufacturability of MPFDs, wafer-scale processing is only just beginning. The knowledge gained from the alumina wafer fabrication methods explored in the present work should be expanded upon, and new substrate materials should be considered. Materials such as sapphire, silicone-carbide, diamond, and silicon are of particular interest, but other materials may also provide specific benefits. Consideration of advanced manufacturing techniques such as very large-scale integration (VLSI) and 3-dimensional printing should be the focus for the optimal production of MPFDs to support the long-term demands of TREAT experimentation.

5. Detector Electronics

The high flux of TREAT transient experiments necessitated the development of current-mode support electronics for MPFDs. The typical pulse-mode electronics can still be used at low powers, and for calibration, but at very high interaction rates, pulse-mode operation is not possible due to sensor paralysis. The same electronics manufacturer was used for pulse-mode development and for current-mode development due to the familiarity of the designers with the electronics system and MPFD sensors. The current-mode development was initiated to expand the MPFD-4 NIM module to support a current-mode preamplifier. The current-mode preamplifier converts the current measurement from the cathode of the detector to a digital frequency for high-fidelity transmission to the counting system ($100\text{ }\mu\text{A} = 10\text{ MHz}$). The system was designed to support up to 0.100 mA on each channel, and to recorder 4,000 samples on each of 4 channels with a pre-register for tracking of fast transients. A triggered threshold was used to initiate the recording of data into a buffer which also includes data preceding the trigger therefore allowing the trigger threshold to be set near the peak expected current and preventing false-triggering while still allowing for the capture of the full transient. Time resolution between 0.25 and 4 ms per bin was integrated to support both fast and slow transients. A similar physical interface was developed (D-sub 9 detector input with 2x Cat7 RJ49 jacks) in order to simplify deployment in tandem with pulse-mode electronics. The same MPFD-4 NIM module can be used in pulse-mode and current-mode (switchable via USB). A prototype current-mode system was developed by Mesytec GmbH & Co. KG and delivered to KSU for benchtop testing.

Before benchtop testing could commence, the software interface for MPFD testing was modified to support current-mode operation. Controls and indicators were added to the LabView® VI corresponding to the new current-mode commands (see MPFD-4 data sheet V10 or later). The integrated pulsar was used to confirm the functionality of both the VI and the hardware in the laboratory. Older MPFD-4 NIM modules

can be sent back to the manufacture for upgrade to support current-mode operation, and all future from the manufacturer will include current-mode and pulse-mode support.

Preliminary testing of the current-mode system was conducted to confirm neutron sensitivity, but more rigorous testing is planned in conjunction with calibration experiments in the coming months. Important concerns include the identification of a unity point where pulse-mode and current-mode operation can both be utilized, and determination of the gamma-ray sensitivity of current-mode. A unity point can be used to cross-calibrate the current-mode response rate with the count-rate from pulse-mode after calibration of the array in pulse-mode. Similar to other systems which operate in current-mode, the signal contribution from gamma rays is also of concern. Further analysis will need to be conducted to determine if a compensation chamber can be used to subtract the gamma-ray induced signal from the total signal.

6. Achievements and Future Outcomes

Much has been accomplished in the first year of instrumentation development for TREAT at Kansas State University. Although the present work focused on MPFDs, there is room for expansion to other instrumentation systems moving forward. We are closer now to the delivery of a tool for local, real-time measurement of neutron flux in TREAT. The results of survivability testing indicate the modifications to the MPFD sensor design are likely necessary to prevent sensor failure from fission-fragment heating. Additional experimental data from irradiation of highly enriched MPFD samples at the KSU TRIGA reactor and from natural uranium MPFD samples deployed at TREAT will help to confirm this conclusion. Furthermore, future efforts should include the investigation of different substrate and electrode materials which could help to mitigate the possibility for catastrophic failure of the sensor during a TREAT experiment. The calibration methods under development are illuminating some of the less-understood characteristics of MPFDs, and are aiding in the refinement of fabrication methods to improve consistency. Additionally, the successful calibration of MPFDs will be necessary to provide the most useful data possible. In the past, unreliable electronics greatly complicated testing of the prototypical sensors. The electronic support system for MPFD arrays up to 4 channels has provided a reliable test platform for characterization and testing.

7. Appendices

The following appendices summarize the present MPFD sensor design for TREAT, other relevant projects related to MPFD research, and the anticipated schedule for future MPFD demands at TREAT. These projects related to MPFD development and are aiding in the rapid innovation of these advanced sensors for in-core neutron flux measurements.

7.1 Appendix A – Current TREAT MPFD Design

The TREAT MPFD contains small ceramic components that form distinct chambers. Each chamber contains a neutron-reactive coating which detects signals arising from gas ionization in the chamber through fission product coulombic interactions. Thorium and natural uranium coatings are each used in two of the chambers to provide sensitivity to fast and thermal spectrum neutrons, respectively. Coating thickness is used to adjust instrument neutron detection efficiency. One each of the thorium and uranium chambers is coated to be low efficiency in order to correspond with the peak neutron flux during transient operations. Similarly, one each of the thorium and uranium chambers are coated to be high efficiency in order to correspond with lower-power steady state operations. Hence the MPFD gives fast and thermal neutron detection for a range of TREAT operating modes. All of the ceramic components are encapsulated in a small Inconel-625 tube with welded end caps. Eight lead wires emerge through a smaller diameter mineral-insulated extension cable. The initial use of the MPFD in TREAT experiments will be in the Multi-SERTTA vehicle in water at Pressurized Water Reactor (PWR) thermal conditions (280°C and 15.5 MPa). INL will provide current drawings and other operational parameters as needed to support development work.

7.2 Appendix B – Summary of Relevant MPFD Projects

Numerous projects are underway which will benefit from the results of the present work, and whose results can also be used to advance progress for TREAT MPFD development. Each project involves a different interest in MPFDs, from sensor-level investigation to deployment of large sensor arrays to measure reactor kinetics in real-time. Continued collaboration between the associated work groups will enhance the capabilities of MPFDs for use in TREAT for both physics testing and experiment monitoring in the future.

7.2.1 NEUP (NEET) Enhanced Micro-Pocket Fission Detector (MPFD) for High Temperature Reactors (INL, KSU, CEA)

The goal of this project is to develop and test high temperature (HT) MPFDs with the capability of measuring thermal neutron flux, fast neutron flux, and temperature within a single instrument package. The design packages the sensor into a mineral-insulated metal-sheathed cable. The robust design of the HT MPFD design has provided the foundation for deployment in multiple MTR experiments. Funding for this project will finish at the end of FY17. Currently, AGR-5/6/7 is planning to deploy an MPFD design consisting of a HT MPFD with a Type N thermocouple in an experiment at the Advanced Test Reactor (ATR). The Accident Tolerant Fuels (ATF) program is planning to deploy a HT MPFD in the ATF-2 Sensor Qualification test to be performed in ATR. The ATF-3 experiments are the first planned experiments to be performed in the restarted TREAT reactor. These test designs provided the impetus for MPFD deployment in TREAT experiments. The ATF-3 program provided requirements and calculations for high pressure usage of the MPFD that drove design selection for the sheath material thickness of the HT MPFD. Additionally, the ATF-3 design program funded significant modeling efforts to locate the MPFD in an optimal location in the test and to begin sensor level modeling of the sensor.

7.2.2 NEUP (NEAMS) A Transient Reactor Physics Experiment with High Fidelity 3-D Flux Measurements for Verification and Validation (KSU)

A suite of steady-state and transient experiments will be conducted at UWNR. The core will be instrumented with a set of detector arrays, each comprised of 4 micro-pocket fission detectors (MPFDs) designed to capture fluxes over a wide range of reactor powers. Detailed computational models are being developed to design the experiments and interpret the measured results. Ultimately, this data can be used to validate the advanced tools under developments for analysis of transient reactors like TREAT.

Currently, the project is planning to deploy a 7x4 array of MPFDs (7 wands of 4 nodes each). These wands will be inserted into individual channels within the University of Wisconsin (UW) Nuclear Reactor. The modular wand design is 6 feet long made of a 5/8 inch outer diameter tube. The wand will initially be tested at the KSU in fall 2017 with planned deployment at UW in winter 2017. The test hardware will be returned to KSU after the project is completed and may be of interest for deployments within the TREAT core. In addition, KSU sensor models developed as a result of this effort have provided strong evidence of the inability of current-mode operation to measure peak neutron flux in TREAT.

7.2.3 NEUP IRP Advanced Instrumentation for Transient Reactor Testing (UW, ISU, KSU, OSU, INL, CEA)

The project is developing specific innovative measurement diagnostics for real-time in-situ monitoring to support transient reactor testing in three key program elements: 1) Develop concepts that lead to next generation fuel motion monitoring system; i.e., advancements in spatial and temporal resolution for hodoscope imaging; 2) Develop instrumentation to support in-pile transient testing that includes temperature measurements, local fast and thermal neutron flux measurements; 3) Demonstrate these novel instrumentation measurement methods in a reactor environment using university TRIGA reactors.

In regards to MPFD-specific applications, little scope was initially dedicated to related topics. However, project evolution has progressed to include important supporting efforts. Idaho State University (ISU) is

now working on characterization of fissile deposits created by KSU with the goal of demonstrating the ability to measure absolute fission rates to <1% uncertainty. Also, recent developments at KSU have initiated experimental testing of the robustness of MPFD fissile deposits in response to TRIGA pulses at KSU.

7.2.4 NEUP IRP Computational & Experimental Benchmarking for Transient Fuel Testing (OSU, UMich, MIT, TerraPower, HTTP, ORNL, ANL, INL)

The project has the following overall goals: (Task 1) a comprehensive evaluation of existing TREAT Facility neutronics data according to established guidelines per the International Handbook of Evaluated Reactor Physics Benchmark Experiments (IRPhEP Handbook); (Task 2a) a complete characterization of existing sodium loop experimental data; (Task 2b) a compilation of relevant empirical data of a representative TREAT Facility flow loop; and (Task 3) an integrated instrumentation plan for the TREAT Facility.

For Task 3, the planned scope included selection and comparative testing of in-core instrumentation in the MITR, executed during the summer of 2017. Further testing is planned in either the Oregon State Reactor (OSTR) or in TREAT in FY18. Current instrumentation selections include dosimetry (wires/foils), a gamma sensor, and other possible local flux/fluence measurement sensors (fission chamber and/or SPND). The MPFD is a potential candidate for inclusion in the testing depending on availability of needed materials.

7.2.5 DOE NEET TREAT Baseline Instrumentation Development (INL)

The transient testing experiments program is actively pursuing the RD&D of several advanced instrument technologies to meet near-term experiment programmatic goals while establishing the base measurement capabilities (state-of-the-art) for next-generation experimentation. Varying levels of development and testing are required to achieve the characterization and qualification necessary for experiment objectives. Primary emphasis is on integration of known technologies, demonstration of interfaces, and instrument performance at test conditions. This program is expected to provide indefinite support for instrumentation to be deployed in TREAT experiments. The development efforts supporting TREAT MPFDs is the topic of this document.

7.2.6 US-ROK INERI Radiation Hardened Readout Circuit Design for High Temperature Micro-Pocket Fission Detectors Operating in Harsh Environments (INL, KAERI, KAIST, Sejong University)

This project is a collaboration of INL with the Korea Atomic Energy Research Institute (KAERI), Korea Advanced Institute of Science and Technology (KAIST) and Sejong University. The U.S. contribution to the project will be supported by the NEUP HT MPFD project for the first year. The remaining two years will be supported by the TREAT Experiments Instrumentation Development Program. As the project title suggests, the project will focus on the development of radiation hardened electronics in an optimized preamplifier design for the HT MPFD for operation in harsh environments. The circuit design has the potential to be directly integrated with the MPFD sensor.

7.2.7 SBIR Advanced Manufacturing of Micro-Pocket Fission Detector (MPFD)

The goal of this Small Business Innovative Research (SBIR) project will be to develop advanced manufacturing capability that will provide a unified MPFD design. The implementation of manufacturing techniques used in the semi-conductor industry may provide high throughput fabrication with very high reproducibility with tight tolerances. A commercial MPFD will be useful in the continued use of these sensors for extensive deployment with experiments at the TREAT facility.

7.3 Appendix C – Schedule of Important TREAT-MPFD Related Dates

The following schedule represents current planning and expected needs. For deployment in TREAT experiment assemblies, fabricated sensors are typically needed ≈ 3 months prior to the listed dates. Several other potential experiments are not listed in this schedule. The quantities indicate the present design plans. If limited sensor quantities are available in the given timeline, sensor placement will be negotiated.

| Date | Event | MPFDs | Results/Update |
|----------------|--|-------|--|
| 7/2017 | OSU IRP MITR Sensor Irradiation | 1 | Deployed sensor Observed neutron-induced pulses Noise problems |
| 8/2017 | Instrumentation testing at IGR in Kazakhstan | 4 | Estimated Date Samples Identified |
| 10/2017 | NEUP NEET HT-MPFD concludes | N/A | Project summary meeting at INL 8/22 |
| 10/2017 | TREAT Restart | N/A | N/A |
| 10/2017-3/2018 | TREAT Physics Testing begins | TBD | Working with SBIR |
| 10/2017-3/2018 | TREAT Experiment Qualification | 2 | N/A |
| 10/2017-3/2018 | OSU IRP TREAT Test | 2 | Collaborating with OSU IRP team |
| 4/2018-9/2018 | Calibration Testing | 8 | N/A |
| 10/2018 | First Experiment in TREAT | 4 per | N/A |

7.4 Appendix D – Schematics

The original MPFD disk and spacer design inherited several dimensions that were arbitrarily set during prior research efforts. Adjusting the dimensions of the MPFD disk and spacer can enhance the fabrication employable fabrication methods and device functionality. Decreasing the chamber thickness improves the uniformity of fission-fragment ionization. Similarly, reducing the diameter of the electrodeposition electrode improves the uniformity of fission-fragment ionization. A smaller electrodeposition electrode also reduces the maximum fissile mass which can be deposited. Increasing the distance between the anode and cathode wires reduces the likelihood that a short will occur across the electrodeposition electrode, but also increases the applied bias necessary to reach saturation velocity of charge carriers in the ionization gas. Eliminating the collar in the spacer enhances the ability of charge carriers to be swept from the chamber and increases pulse amplitudes.

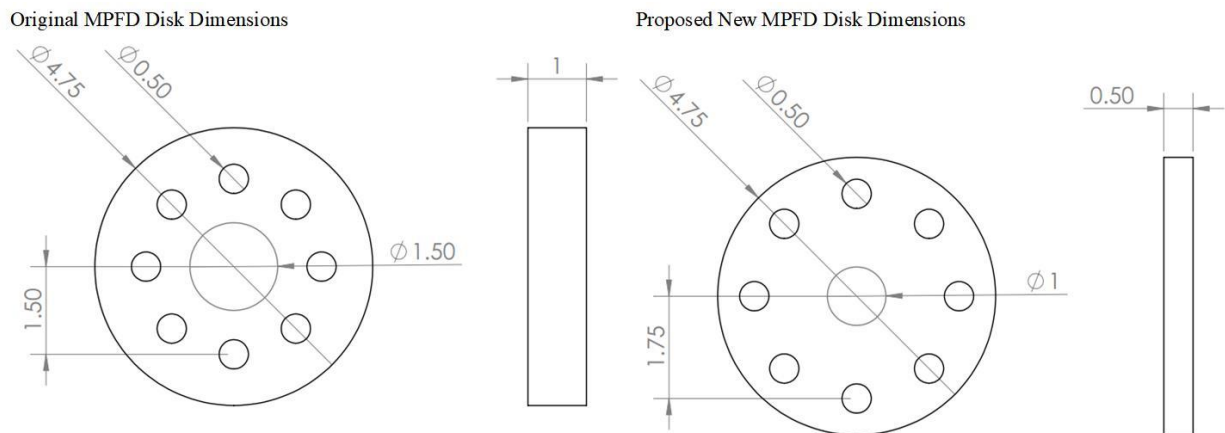


Fig. 7.1. Small modifications to the MPFD disk geometry can improve functionality and manufacturability (units in mm).

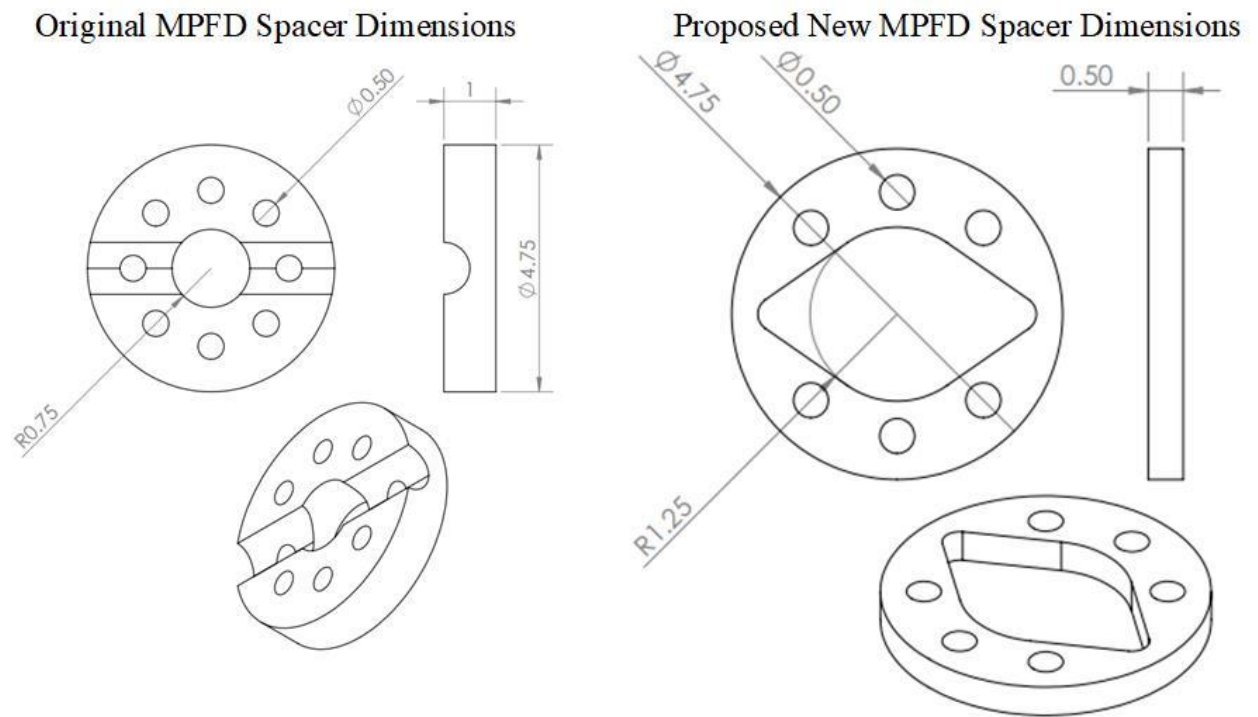


Fig. 7.2. An improved spacer design allows for better charge carrier transport in the ionization chamber (units in mm).

8. References

- [1] M.A. Reichenberger, T. Ito, P. B. Ugorowski, B. W. Montag, S. R. Stevenson, D. M. Nichols, D. S. McGregor, "Electrodeposition of Uranium and Thorium onto Small Platinum Electrodes," *Nucl. Inst. and Meth. Res. A*, no. 812, pp. 12-16, 2016.
- [2] Nuclear Regulatory Commission, "49CFR173.434," [Online]. Available: <https://www.gpo.gov/fdsys/pkg/CFR-2010-title49-vol2/pdf/CFR-2010-title49-vol2-sec173-434.pdf>. [Accessed 14 8 2017].
- [3] V. K. Patel, M. A. Reichenberger, J. A. Roberts, T. C. Unruh and D. S. McGregor, "Simulated Performance of Micro-Pocket Fission Detectors (MPFDs) in the Transient REAactor Test (TREAT) Facility using MCNP6," *Annals of Nuclear Energy*, submitted.
- [4] J. C. Boyington, R. L. Reed, R. Ullrich and J. A. Roberts, "Gamma-Ray and Thermal-Neutron Filter Design for a TRIGA Penetrating Beam Port," in *ANS Winter Conference*, 2017.
- [5] Synova, "Laser MicroJet," Synova, 2017. [Online]. Available: <https://www.synova.ch/technology/laser-microjet.html>. [Accessed 14 8 2017].
- [6] M. Reichenberger, T. George, R. Fronk, P. Ugorowski, J. Geuther, J. Roberts, T. Ito, H. Vo-Le, S. Stevenson, D. Nichols and D. McGregor, "Advances in the Development and Testing of Micro-Pocket Fission Detectors (MPFDs)," in *IAEA International Conference on Research Reactors: Safe Management and Effective utilization*, Vienna, Austria, 2015.
- [7] M. A. Reichenberger, T. C. Unruh, P. B. Ugorowski, T. Ito, J. A. Roberts, S. R. Stevenson, D. M. Nichols, D. S. McGregor, "Micro-Pocket Fission Detectors (MPFDs) for in-core neutron detection," *Annals of Nuclear Energy*, no. 87, pp. 318-323, 2016.
- [8] M. A. Reichenberger, D. M. Nichols, S. R. Stevenson, T. M. Swope, C. W. Hilger, J. A. Roberts, T. C. Unruh and D. S. McGregor, "Fabrication and Testing of a 4-Node Micro-Pocket Fission Detector Array for the Kansas State University TRIGA Mk. II Research Nuclear Reactor," *Nucl. Inst. and Meth. Res. A*, p. Submitted, 2017.
- [9] NucFil, LLC dba NFT, "NFT," NucFil, LLC, 2017. [Online]. Available: <http://www.nftinc.com/>. [Accessed 19 1 2017].
- [10] M. A. Reichenberger, T. C. Unruh, J. A. Geuther, D. M. Nichols, T. J. Sobering, J. A. Roberts, P. B. Ugorowski and D. S. McGregor, "Electronic Support System

Enhancements for Micro-Pocket Fission Detectors (MPFDs)," in *Conf. Proc. IEEE Nucl. Sci. Symp.*, Strassbourg, FR, 2016.

Appendix B

Infrared Pyrometry Development for TREAT Experiments

2017 Annual Report

A. Fleming, C. Jensen, K. Condie

Idaho National Laboratory

Table of Contents

| | | |
|-----|---|----|
| 1. | Introduction | 1 |
| 2. | Background..... | 1 |
| 3. | Approach | 3 |
| 4. | Manufacturing Custom High Transmission Optical Connections..... | 4 |
| 5. | Fiber Survivability Study | 4 |
| 6. | Sheathed Sapphire Rods | 6 |
| 7. | Pyrometer Calibration | 9 |
| 8. | Oxidation Test | 9 |
| 9. | Design of Experiments | 10 |
| 10. | Temperature Measurement | 15 |
| 11. | Summary and Conclusions | 17 |
| 12. | Future Work..... | 17 |
| 13. | References | 18 |

1. Introduction

The development of non-contact, high-speed temperature measurements using infrared (IR) pyrometry has been the focus of significant development and evaluation. A high-speed pyrometer system is a high priority for deployment in TREAT with capability to measure cladding surface temperature with millisecond time resolution. An optical fiber line is required to collect the IR emission from the target and transport it several meters to the detector. The collection optics must be able to withstand the harsh PWR conditions of a test vehicle and allow for hermetic feedthroughs at high temperature across a high pressure boundary. The pyrometer has potential to provide unprecedented data on the temperature evolution of fuel cladding during a transient test. This temperature evolution combined with other high-speed instrumentation, such as the boiling detector, will provide important data on the sequence of thermal/thermal-hydraulic events leading up to fuel failure. In-pile IR temperature measurements present a unique set of challenges for instrument and mechanical design, data interpretation, and the pyrometry method of choice. In order to achieve the goal of near-term in-pile deployment of IR pyrometry, a multi-pronged approach has been undertaken to rapidly gain capability and expertise. Two distinct commercial pyrometer systems are undergoing testing, each based on different principles of operation, one active and one passive, and each having potential strengths and weaknesses. In addition, a university partnership has been established with the University of Pittsburgh to design, build, and test a custom IR pyrometer system that will allow for flexible adaptation of the system for specific test objectives and/or requirements and will target a time resolution of < 1 ms.

The active pyrometer system was procured first and has been undergoing evaluation in the High Temperature Test Laboratory (HTTL) at Idaho National Laboratory (INL). To date, it has been undergone significant assessment of its operation, capabilities, and limitations. This process has been streamlined through the use of design of experiments factorial analysis and additive manufacturing to rapidly build new experimental fixtures. The calibration procedure has been learned and employed to understand potential deployment requirements. Significant component-level testing has been conducted to determine feasibility of the optical-line design for deployment in TREAT. This report begins with an overview of pyrometry to provide a technical foundation to understand the developmental needs and progress. This introductory section is followed by a discussion about the approach taken in the development and evaluation, and finally the results and conclusions from testing will be provided.

2. Background

Pyrometry is the process of determining the temperature of an object from the natural emitted thermal radiation governed by Planck's Law. An ideal emitter is termed a "blackbody" and its thermal emission is described precisely by Planck's Law. Non-blackbody materials emit a fraction of this thermal radiation. This fraction of emission is determined by a material property called emissivity. Knowing or measuring material emissivity is key to performing accurate temperature measurements. Different methods of pyrometry are largely distinguished by the method used to determine material emissivity.

Planck's Law describes the emission of radiation in a given direction, per solid angle, per unit surface area normal to that given direction. All pyrometers measure the thermal radiation emission and relate the measured signal back to some form of Planck's Law. Pyrometers can largely be classified by a few categories including passive or active and single, dual, or several wavelength. Passive pyrometers operate by only collecting thermal radiation and do not incorporate the use of lasers or any other external light source. Active pyrometers typically incorporate a pulsed laser that is aligned such that it reflects off the target surface. The power of the reflected light can be measured and related to the emissivity of the target material.

Many pyrometers measure the thermal radiation at one wavelength. The signal received from these types of pyrometers is directly proportional to Planck's Law at that wavelength. The proportionality is determined by the sample emissivity. The dominant uncertainty with pyrometers generally stems from the determination of the target emissivity. For single wavelength pyrometers the emissivity is either measured or assumed to be known from literature data or some other source.

Dual wavelength pyrometers perform thermal radiation measurements at two different wavelengths. The determination of temperature from these two measurements only requires the ratio of the emissivity at the two wavelengths, rather than the actual value of emissivity at the two wavelengths. Often in dual wavelength measurement the wavelengths are chosen such that the values of emissivity are similar, therefore their ratio is close to unity.

The final classification of pyrometers are known as multi-band or spectral pyrometers. The operation of these pyrometers perform measurements at several wavelengths, and essentially fit the spectral dependence of Planck's Law to measurements. These pyrometers perform N spectral measurements, and use a model to describe emissivity with $N-1$ fit parameters. This $N-1$ parameters along with the unknown temperature allows for each parameter and temperature to be determined uniquely. A commercial system based on a variation of this technique has been purchased to provide detailed performance comparison with the active pyrometer, which is currently undergoing evaluation.

The active pyrometer under development and evaluation at HTTL is a high speed commercial pyrometer with custom modifications made by both the manufacturer and INL personnel. The custom modifications are all related to the complications induced by performing in-pile measurements. A diagram showing the operation of the system is shown in Figure 1. The system utilizes two optical lines, the first supplies laser light to the surface of the target (pump line), and the second collects the reflected laser light and the emitted thermal radiation (probe line). From these measurements, target emissivity and temperature may be calculated when properly calibrated. The optical line is composed of silica optical fibers and sapphire rods. The silica fibers transmit the light between the pyrometer and just outside of the pressure vessel inside of the experiment vehicle in treat. Before entering the pressure vessel the light is transferred to the sapphire rods and then ultimately the fuel cladding. There are many engineering challenges associated with developing this optical line that have practical consequences in the performance of the pyrometer. The active pyrometer has theoretical challenges associated with it due to the method of pyrometry it utilizes. Both the engineering and theoretical challenges associated with this active pyrometer system are addressed in the work presented here.

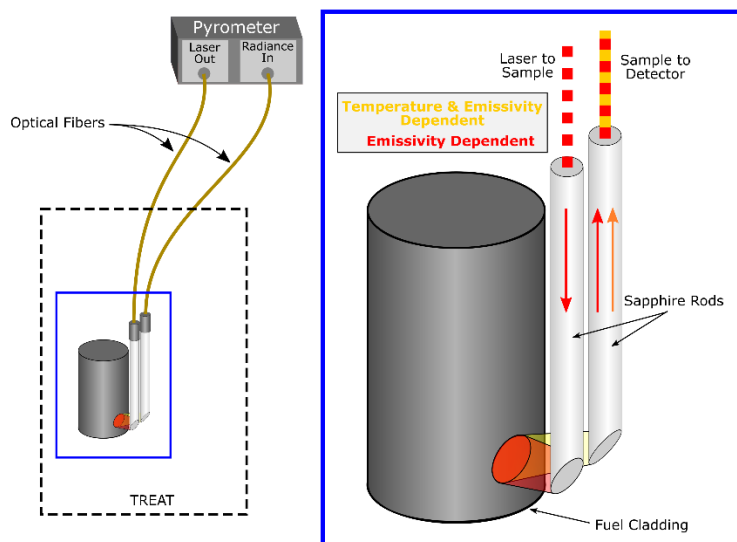


Figure 1. Diagram showing the operation of the active pyrometer under development and evaluation in the HTTL. The dashed black box represent the TREAT reactor showing which components are inside and outside of the reactor.

3. Approach

Deploying instruments in an in-pile environment is generally a great technical and engineering challenge. Detailed understanding of the instrument science is critical to achieving success as well as addressing what on the surface seem like simple engineering problems in terms of the required interfaces and assembly logistics associated with in-pile fuels testing.

The engineering challenges associated with the pyrometer mainly deal with the design of the optical paths for the pyrometer. The high speed pyrometer will be deployed for temperature measurements inside an experiment vehicle in the TREAT reactor. The pyrometer is currently being developed for a deployment in an experiment vehicle which provides Pressurized Water Reactor (PWR) conditions (300° C, 15.5 MPa) for fresh fuel test specimens. The optical line penetrating the capsule pressure boundary must be capable of withstanding (at a minimum) PWR conditions. Optical feedthroughs must be developed that are capable of transmitting the light out of the pressure vessel without damaging the optics.

Some of the defining challenges facing a pyrometer deployment in TREAT are:

- Uncertainties introduced from alignment and positioning error of the sapphire rods or fuel pin;
- Related to the previous, system calibration will be sensitive to exact positioning so that the logistics of eventual test assembly need to account for this;
- Incorrect emissivity determination related surface radiation properties and geometry: diffuse/specular reflection properties of target, varying target emissivity (material oxidizing during experiment), cylindrical cladding target surface;
- Error introduced from background radiation from surrounding environment reflecting off target surface;
- Influence of water/steam by absorption, refraction, or scattering the light.

While these challenges are not unique to the nuclear materials testing applications, the harsh environment, limited access to the target, and overall material limitations make them much more challenging to overcome than conventional pyrometer applications.

These challenges have been the focus of this work. Results are presented in the following sections. The first half of this report is dedicated to addressing the engineering challenges because they represent the first critical roadblock to potential deployment of a pyrometer. The second half discusses the initial exploration conducted that addresses some of the measurement science challenges.

4. Manufacturing Custom High Transmission Optical Connections

Pyrometers need to collect the emitted thermal radiation and focus it onto a photodetector. The magnitude of this signal is used to determine the targets temperature. Therefore, signal losses in the optical path can greatly influence the temperature measurement. The calibration process is critical to accurate pyrometer measurement as its purpose is to eliminate any potential bias caused by these losses. Therefore, assuming signals levels are high enough to be measured, these losses do not affect the accuracy of the pyrometer unless they change after the calibration. Fiber-to-fiber connections are often used in fiber-based optical systems to facilitate overall system assembly and to connect differing optical components together. The transmission through these connections is largely dependent on the quality of the connection, determined by the alignment of the optically transmitting cross sections (fiber cores), perpendicularity of the polished surfaces, the quality of the polished interfacing ends, and the overall degree of surface to surface contact. For ideal good performance and reproducible response in these connections, all three of these parameters should be controlled precisely. Thus, quality fiber optic connections is critical for the performance of an optical pyrometer and requires in-house fabrication and characterization capabilities, expertise, and experienced personnel. Figure 2a shows the end of a fiber for a critical optical connection in the active pyrometer system obtained from the commercial vendor of the system. Figure 2b displays a representative example of a fiber end that was manufactured in the HTTL laboratory at INL. The images clearly show the fiber end produced at INL will perform much better with lower loss and more reproducible transmission. The contrast in the quality of the connectors highlights the critical need to do have these capabilities in HTTL.

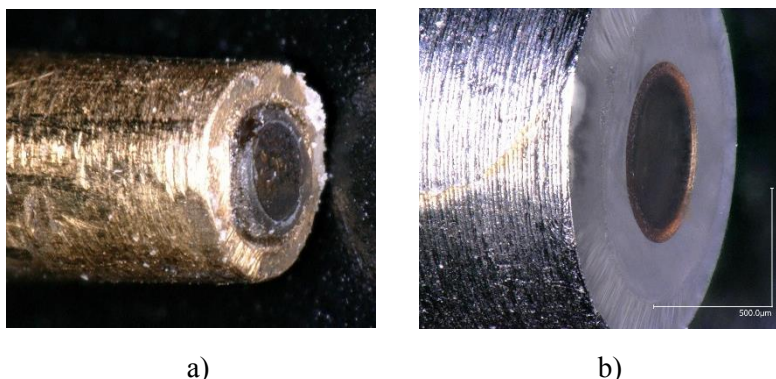


Figure 2. Micrographs of the ends of optical fibers. Flat and well-polished end are required for good physical contact and low loss optical connection a) The optical fiber provided with the commercial pyrometer system. b) Custom optical fiber end made at HTTL

5. Fiber Survivability Study

Experiment conditions require that the optical fibers must be capable of surviving the extreme conditions of PWR temperature and pressure. To obtain measurement of cladding surface temperature, part of the optical line would have to be located in the coolant and therefore survive and perform well in PWR conditions. To investigate fiber material behavior in this condition, five fiber samples were placed in the autoclave at PWR conditions (300° C and 15.5 MPa) for 24 hours. Micrographs of the fibers taken after the test can be seen in Figure 3. All of the silica fibers tested showed significant degradation of the fiber. The aluminum and polyimide coatings were damaged sufficiently that they no longer protected the fiber. The

copper coating survived the environment, but the silica was eroded at the exposed end of the fiber. Though detailed research into the water chemistry and interactions with specific different silica fiber compositions could help, the results show exposed silica fiber is not a good option for PWR conditions. The sapphire fiber had no visible damage from the exposure as seen in Figure 3e. Therefore, sapphire is recommended to be used for applications involving PWR water environments.

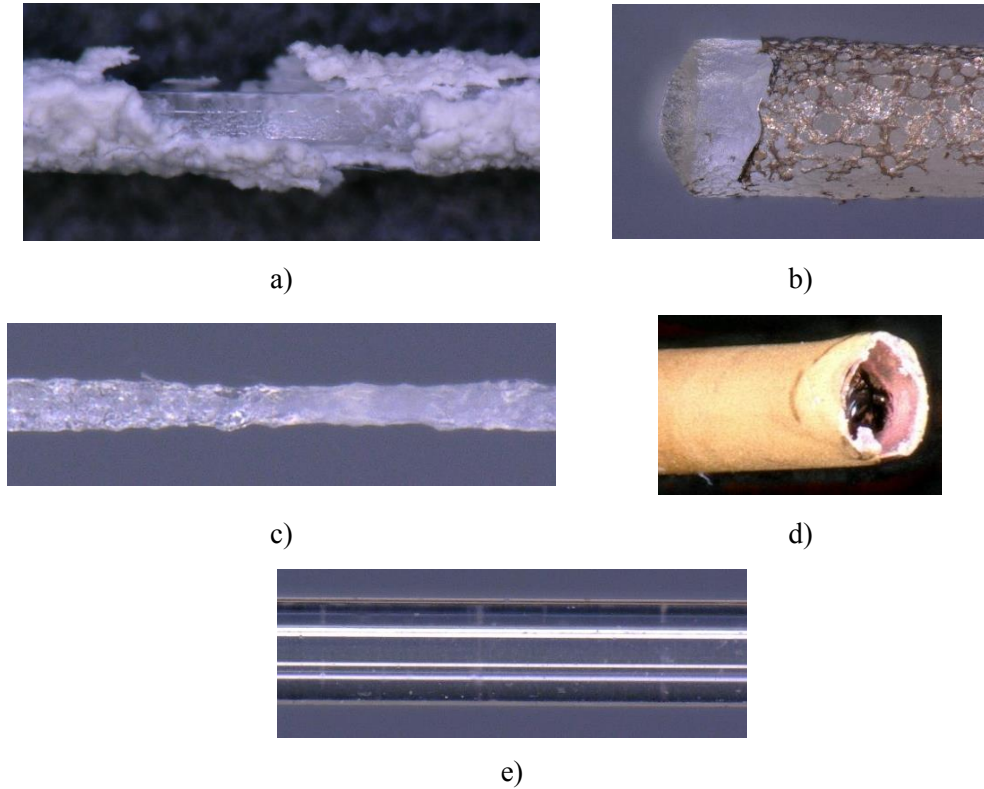


Figure 3. Micrographs of optical fibers after 24 hours in the autoclave at 300° C and 2250 psi a) Aluminum coated silica fiber b) polyimide coated silica fiber c) bare silica fiber d) copper coated silica fiber e) sapphire fiber

6. Sheathed Sapphire Rods

The requirements for a feedthrough in initial water based testing are to make a hermetic pressure seal up to the design pressure of the experiment vessel of 7500 psi. The feedthrough location must also allow for temperatures up to approximately 350°C. In addition, there is limited footprint available on the feedthrough flange and limited head room above and below it as well. Commercial feedthrough products are available that are rated to very high pressures (much higher than needed). However, most available products are limited to about 200°C and frequently are too large in some dimension to fit within spatial constraints.

A novel design for a feedthrough into high pressure water environment requiring high temperature compatibility uses a Conax fitting to allow penetration of metal-sheathed sapphire rods into the pressure vessel. This fitting has a pliable sealant that tightens around the sapphire rods as it is compressed by a tightening nut to provide a seal for the pressure boundary. The compression from this fitting can potentially damage the sapphire rods. Preliminary tests showed the sapphire rods fractured under the compressive stresses from the Conax fitting. After the preliminary test, custom metal-sheathed sapphire rods were purchased from a vendor to provide protection from the compressive forces encountered in the feedthrough. The bottom part of the sheathed sapphire can be seen in Figure 4.

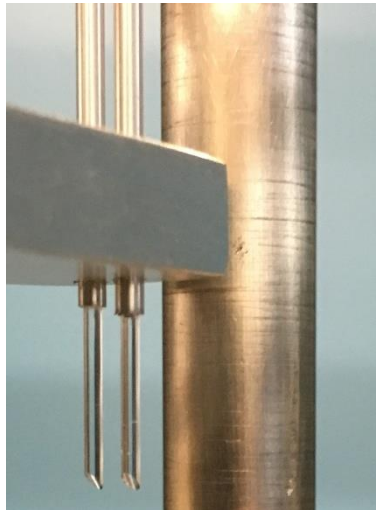


Figure 4. The two sheathed sapphire rods on the left side of the image pointing towards the electrically heated cylinder. The sheathing ends about 1 cm, just after passing through the holder for alignment.

The metal sheath is attached by epoxy to the sapphire rods at the top of the rod. CT scans were taken to observe the bond between the sapphire and metal sheathing. A good bond at the top of the sheathed sapphire can be seen in the CT scan shown in Figure 5a. The section of the fiber rod shown in the CT scan in Figure 5b is the bottom section of the sheathing which can also be seen in the photograph in Figure 4. This CT scan allows for an inspection of the bonding and as-manufactured state of the sheath and sapphire.

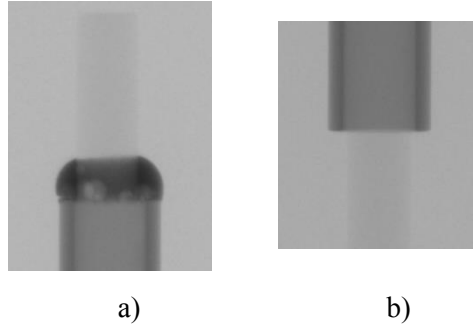


Figure 5. CT Scan of metal sheathed sapphire rods. a) Top of the sapphire rod. The rounded dark area is the epoxy used for sealing the sheath to the rod. b) Bottom of the sheathing

An optical experiment was configured in which the transmission through the rods were monitored with photodetectors while the feedthrough was torqued to its specification. The experimental configuration with the light source, feedthrough, sapphire rods, and photodetectors can be seen in Figure 6.

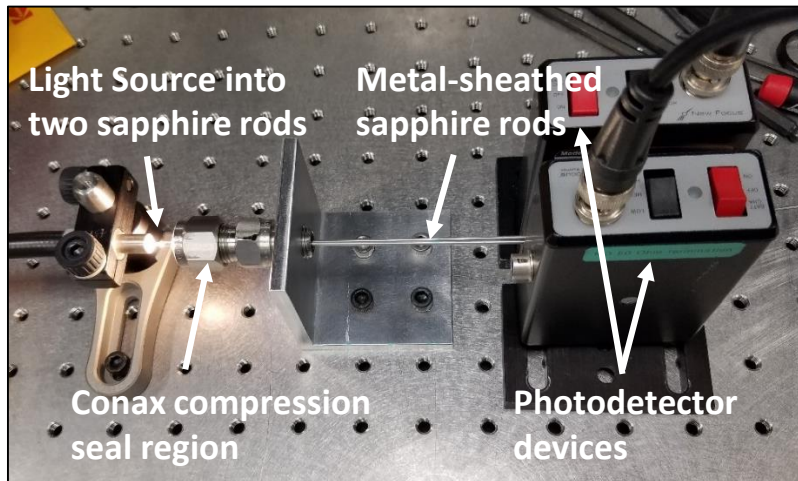


Figure 6. Photograph of the sapphire rod pressure feed-through test. The transmission through the sapphire rods were measured while the fitting was tightened.

As shown in Figure 7, the results from the Conax feedthrough test show good transmission through the sapphire throughout the torquing processes. The alignment of the sapphire rod to the photodetectors changes at the initial stages of tightening when the seal and rods still have some play. This leads to an initial decrease in the measured voltage, but it levels off quickly after the sapphire rods reach a fixed position. If one of the sapphire rods had fractured during the torquing process, a sharp decrease would likely have been observed. These test results confirm that this feedthrough design is a viable solution for the high pressure, high temperature feedthrough for the sapphire rods. The optical path should remain intact in the seal to transmit infrared radiation out of the capsule to the pyrometer for measurement. In conjunction with the autoclave testing, this compression seal-sapphire compatibility experiment confirms at the component that metal-sheathed sapphire in a Conax seal will provide the required performance for PWR capsule-based testing. Future work will include a small task to perform a more integral test in the PWR autoclaves at HTTL.

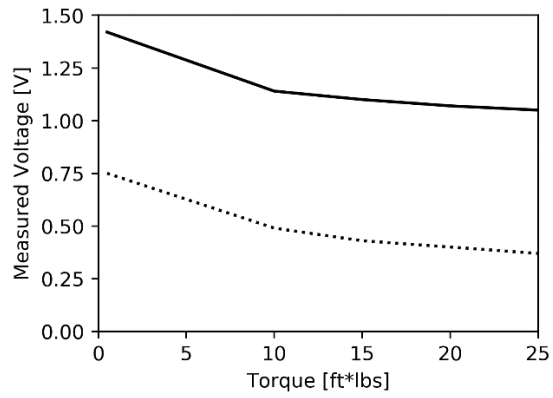


Figure 7. Measured voltage from photodetectors in the Conax feedthrough transmission test. The alignment of sapphire rods changes slight at the ignition stages as the fitting begins to tighten, but quickly levels starts to level off up to the torque specification of the Conax seal of 25 ft·lbs.

7. Pyrometer Calibration

As discussed described in a previous section, pyrometers determine target temperature by quantitatively measuring the radiance collected by and transmitted through the optical path. The transmission has been improved through the new optical connections that were shown in Figure 2b. The increased transmission requires a recalibration of both the reflection and radiance measurements performed by the pyrometer.

A blackbody radiation reference source was acquired to accomplish the radiance measurement calibration. The blackbody source consists of an isothermal cavity which emits thermal radiation near that of an ideal blackbody emitter. In this calibration procedure, the sapphire rod is pointed into the cavity of the blackbody source in which the temperature is known. The pyrometer takes a measurement of radiance at this known value and uses it for the calibration.

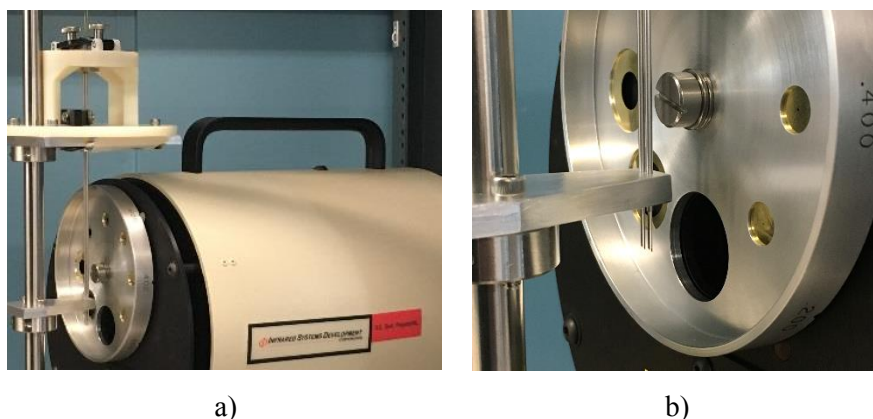
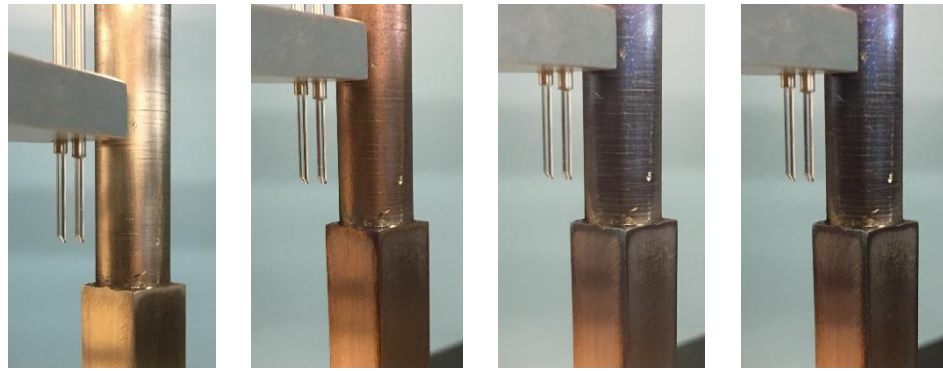


Figure 8. Calibration of pyrometer using blackbody radiation source. a) The experimental setup showing rod alignment and manipulation in the upper left with blackbody source in the lower right b) close-up image of the blackbody aperture and sapphire rods aimed at the cavity.

The reflectance measurement is calibrated through the use of a reflectance standard. The reflectance standard was positioned at the design working distance of the pyrometer. The sapphire rods are then backlit to illuminate the area from which they collect emitted light. In this manner, the rods are then aligned so the illuminated areas overlap each other. With proper alignment, the pyrometer emits laser light from one of the sapphire rods, and collects the reflected light with the other sapphire rod. This measurement can be used for calibration since the reflectivity of the target is a known standard.

8. Oxidation Test

Active pyrometers measure reflected laser light to determine the emissivity of a sample requiring an additional active light source. The real-time emissivity measurement is the main advantage over passive pyrometer systems. An experiment was constructed to test the capability of the commercial active-mode system to measure changes in emissivity via the reflected signal. This test used the pyrometer to measure target temperature and emissivity at various oxidation levels. For each of these measurements the rod was heated to 250° C. After a measurement was taken, the rod surface was oxidized by raising and holding the temperature at 600° C until a visible change in the surface was noticeable. The rods temperature was then decreased to 250° C where the next measurement was taken. The results from these tests can be seen in Figure 9 along with images of the measured rod surface, which indicates the evolution of oxidation at each measurement. The results show some capability of the system to measure the target temperature while the surface sample surface emissivity is changing. This test was done prior to the recalibration of the system which accounts for some of the discrepancy between the measured temperature and the actual emissivity/temperature.



$\epsilon=28.1$, $T=266^\circ\text{C}$ $\epsilon=44.6$, $T=256^\circ\text{C}$ $\epsilon=48.2$, $T=256^\circ\text{C}$ $\epsilon=81.2$, $T=240^\circ\text{C}$

Figure 9. Photographs of the target after different levels of oxidations. All temperature and emissivity measurements were made at 250°C . Note: these tests were performed prior to the enablement of calibration, which likely accounts for the reported temperature variations.

9. Design of Experiments

Many factors influence the temperature measurements from a pyrometer, including but not limited to: alignment, target surface properties, and anything that influences transmission through the optical path. Many factors are also interrelated and will have significant interaction effects that can be different from their respective separate effect. A design of experiments factorial analysis is well-suited to evaluating the main and interaction effects of these factors.

The commercial active pyrometer was evaluated using a 2^5 factorial using 3 replications under each condition. The factors and their conditions used in this factorial can be seen in **Error! Reference source not found.** In general, the low values of the factors are considered an “as-designed” condition and the high values are an “off-design” condition. Theta 1 and theta 2 refer to the aiming direction of sapphire rod number 1 and 2, respectively. The well-aligned conditions of each rod is considered to have an angle of 0° . The rod position was manipulated by a mechanical stage in two directions, X and Y. The X direction was defined as the lateral movement, and the Y direction was defined as longitudinal movement (moving away from sapphire rods). The combinations of factor conditions in each experimental case is shown in Table 2. The measured outputs from the design of experiments are the pyrometer measured emissivity, un-corrected temperature, and corrected temperature. The order of experiments was randomized to reduce the influence of underlying uncontrolled factors on the results. The design of experiments was conducted according to the guidelines provided by Montgomery [1].

Table 1. The factors and levels used in the design of experiments factorial analysis.

| <i>Factor</i> | <i>Low (-)</i> | <i>High (+)</i> |
|---------------------------|----------------|---------------------|
| <i>(A) Theta 1</i> | 0° | 15° |
| <i>(B) Theta 2</i> | 0° | 15° |
| <i>(C) Rod X Position</i> | 0 | 0.5 mm |
| <i>(D) Rod Y Position</i> | 0 | 0.5 mm |
| <i>(E) Shape</i> | Flat Surface | Cylindrical Surface |

Table 2. Descriptions of the state of all the parameters under each experimental condition evaluated. The (-1) and (1) refer to the high and low states described in **Error! Reference source not found.**

| Case | Theta 1 | Theta2 | X | Y | Shape |
|------|---------|--------|----|----|-------|
| 1 | -1 | -1 | -1 | -1 | -1 |
| 2 | 1 | -1 | -1 | -1 | -1 |
| 3 | -1 | 1 | -1 | -1 | -1 |
| 4 | 1 | 1 | -1 | -1 | -1 |
| 5 | -1 | -1 | 1 | -1 | -1 |
| 6 | 1 | -1 | 1 | -1 | -1 |
| 7 | -1 | 1 | 1 | -1 | -1 |
| 8 | 1 | 1 | 1 | -1 | -1 |
| 9 | -1 | -1 | -1 | 1 | -1 |
| 10 | 1 | -1 | -1 | 1 | -1 |
| 11 | -1 | 1 | -1 | 1 | -1 |
| 12 | 1 | 1 | -1 | 1 | -1 |
| 13 | -1 | -1 | 1 | 1 | -1 |
| 14 | 1 | -1 | 1 | 1 | -1 |
| 15 | -1 | 1 | 1 | 1 | -1 |
| 16 | 1 | 1 | 1 | 1 | -1 |
| 17 | -1 | -1 | -1 | -1 | 1 |
| 18 | 1 | -1 | -1 | -1 | 1 |
| 19 | -1 | 1 | -1 | -1 | 1 |
| 20 | 1 | 1 | -1 | -1 | 1 |
| 21 | -1 | -1 | 1 | -1 | 1 |
| 22 | 1 | -1 | 1 | -1 | 1 |
| 23 | -1 | 1 | 1 | -1 | 1 |
| 24 | 1 | 1 | 1 | -1 | 1 |
| 25 | -1 | -1 | -1 | 1 | 1 |
| 26 | 1 | -1 | -1 | 1 | 1 |
| 27 | -1 | 1 | -1 | 1 | 1 |
| 28 | 1 | 1 | -1 | 1 | 1 |
| 29 | -1 | -1 | 1 | 1 | 1 |
| 30 | 1 | -1 | 1 | 1 | 1 |
| 31 | -1 | 1 | 1 | 1 | 1 |
| 32 | 1 | 1 | 1 | 1 | 1 |

Figure 10a shows the custom experimental setup used to perform the alignment experiments with an electrically heat rod for a target. The plastic device shown in Figure 10b was additively manufactured to provide a quick turnaround in the development of the experimental setup. Its primary purpose is to provide a custom connection between the optical fibers and the sapphire rods and to allow for the alignment of the sapphire rods to be manipulated. The pyrometer target can be seen in Figure 10c with the flat and cylindrical section clearly visible. A thermocouple is welded onto the back side of the target (not visible) which is

used as a feedback to a temperature controller driving a cartridge heater inside of the rod. This accurately controls the temperature of the target surface.

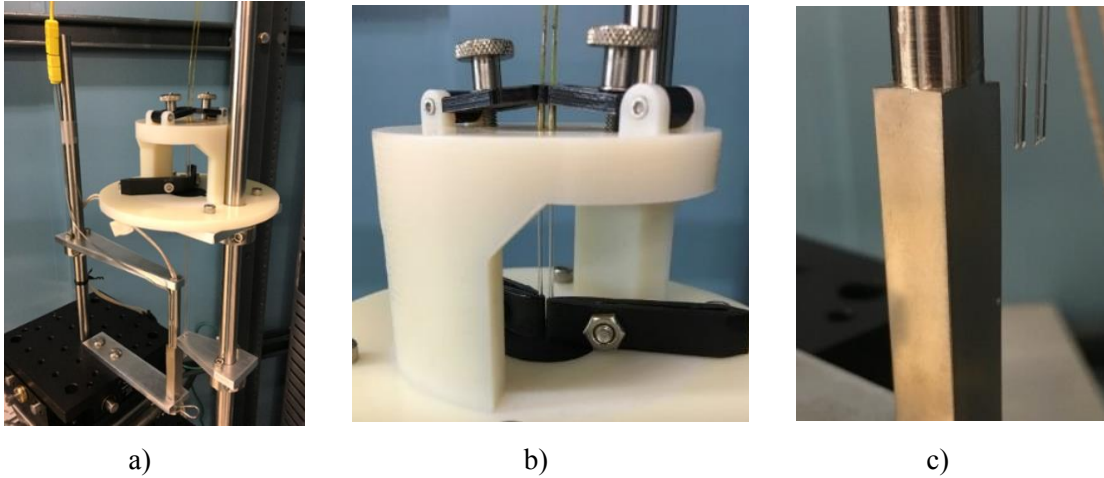


Figure 10. Photographs of experimental setup used in the design of experiments. a) shows the whole test setup b) shows the fixture used for manipulating the sapphire alignment and the sapphire to silica fiber coupling c) close-up image of the electrically heated rod and sapphire rods.

Several valuable results were obtained from the design of experiments. The main and interaction effects for each factor can be seen in Table 3. The complex nature of the pyrometer operation and interaction effects can make the interpretation of the results complicated. With this in mind, there are some clear observations that can be made. Factor A (θ_1) is the control of the aiming of the sapphire rod collecting the radiance from the target. All of the un-corrected temperature information is obtained through this rod alone. This fact is manifested in a strong dependence of θ_1 and target shape on the un-corrected temperature. These results are expected. The consistency provides confidence that the experimental apparatus and experiments were well controlled, and good results were obtained.

The interpretation of emissivity measurements is much more complicated. There are many interaction effects that can influence the measurement of the reflected light. There are many off-design conditions which could lead to a greatly reduced or increased reflection, mainly due to the interaction effects of the parameters. For example, if a flat target was moved closer to the sapphire rods and the angle of the two rods was adjusted such that the reflected light was directed into the collection rod, a significantly higher reflection would be measured. This condition represents an off design condition corresponding to the factor ABD. It is easy to understand how this effect would not be the same if the surface is curved such as ABDE. This specific example can be seen in the results where ABD leads to a significantly decreased emissivity (high measured reflectivity), but ABDE leads to an increased emissivity (lower measured reflectivity). There are too many similar off-design conditions that can lead to significantly different measurements of emissivity to discuss, but a quick glance at Table 3 provides an idea of how complicated these interaction effects are. Another important observation on the emissivity measurements relates to the magnitude of the main effects compared to the interactions. The largest effects (both positive and negative) are the interaction effects between factors rather than the main effects. Similar to the example given earlier, this finding can be explained by considering off-design conditions where two or more off-design conditions lead to a much increased or decreased reflection as compared to only one factor in the off-design condition.

Table 3. Tabulated data of the main and interaction effects for factors in the design of experiments. The cells are high-lighted corresponding to the cells so the large effects are easily identified.

| | Emissivity | Un-corrected Temperature | Corrected Temperature |
|-------|------------|--------------------------|-----------------------|
| A | 9.29 | -5.38 | -3.65 |
| B | -10.95 | -0.23 | 14.14 |
| AB | 31.08 | -0.68 | -0.63 |
| C | 32.47 | 1.03 | 8.33 |
| AC | 2.28 | -0.14 | -7.64 |
| BC | -17.91 | -0.28 | 11.28 |
| ABC | 40.65 | 0.12 | -0.94 |
| D | -28.26 | -0.92 | -8.06 |
| AD | -8.74 | -0.35 | 1.72 |
| BD | -7.42 | -0.99 | -3.65 |
| ABD | -32.58 | -1.33 | -5.29 |
| CD | -44.19 | 0.51 | 3.59 |
| ACD | 8.74 | -0.58 | -1.63 |
| BCD | 9.99 | 0.57 | -4.32 |
| ABCD | -32.32 | 1.09 | -6.21 |
| E | -8.55 | 8.08 | 23.1 |
| AE | -64.72 | -3.82 | 21.19 |
| BE | -56.5 | 0.28 | 19.03 |
| ABE | -5.44 | 0.12 | 0.63 |
| CE | -6.81 | 0.35 | 10.1 |
| ACE | -33.53 | 0.09 | -7.92 |
| BCE | -55.67 | -0.68 | 13 |
| ABCE | 12.19 | -0.44 | -6.71 |
| DE | -10.39 | -0.71 | 5.32 |
| ADE | 33.9 | -0.67 | -6.09 |
| BDE | 34.25 | 0.42 | -4.68 |
| ABDE | 6.56 | -0.3 | -6.33 |
| CDE | -1.94 | -0.42 | -1.49 |
| ACDE | 42.27 | 0.02 | 0.85 |
| BCDE | 43.56 | 0.09 | -4.37 |
| ABCDE | -0.33 | 0.59 | -3.69 |

In addition to the main and interaction effects, an analysis of variance ANOVA table was calculated for each of the output parameters in the design of experiments. The ANOVA tables provide a statistical test to determine if the means of several treatment conditions are equal. These results should be interpreted in conjunction with the main and interaction effects. If the ANOVA table shows the mean of a group is not statistically different then the effect of the factor(s) for the group under consideration is probably not very useful. However, if the mean is shown to be statistically different then it provides confidence in the effect for the factor(s) is important. The ANOVA tests for the three output parameters can be seen in Table 4 through Table 6. The variability in the experimental results causes only a small portion of the treatment conditions to be statistically significant. A range of p-values are shown in each ANOVA table. Many of the factors that had strong effects from the design of experiments also show up as statistically significant.

Table 4. ANOVA table from the design of experiments results for emissivity. P values < 0.1 are highlighted in green

| Factor | Sum of Squares | DoF | Mean Square | F0 | p value |
|--------|----------------|-----|-------------|------|---------|
| A | 2072.6 | 1 | 2072.6 | 0.12 | 0.7305 |
| B | 2877.88 | 1 | 2877.88 | 0.17 | 0.68488 |
| AB | 23185.68 | 1 | 23185.68 | 1.34 | 0.25152 |
| C | 25309.07 | 1 | 25309.07 | 1.46 | 0.23113 |
| AC | 125.13 | 1 | 125.13 | 0.01 | 0.93252 |
| BC | 7695.57 | 1 | 7695.57 | 0.44 | 0.5074 |
| ABC | 39665.46 | 1 | 39665.46 | 2.29 | 0.13508 |
| D | 19170.45 | 1 | 19170.45 | 1.11 | 0.29667 |
| AD | 1835.23 | 1 | 1835.23 | 0.11 | 0.74583 |
| BD | 1320.02 | 1 | 1320.02 | 0.08 | 0.78336 |
| ABD | 25476.26 | 1 | 25476.26 | 1.47 | 0.22961 |
| CD | 46856.43 | 1 | 46856.43 | 2.71 | 0.10488 |
| ACD | 1832.25 | 1 | 1832.25 | 0.11 | 0.74603 |
| BCD | 2396.4 | 1 | 2396.4 | 0.14 | 0.71112 |
| ABCD | 25065.45 | 1 | 25065.45 | 1.45 | 0.23336 |
| E | 1754.8 | 1 | 1754.8 | 0.1 | 0.75127 |
| AE | 100539.93 | 1 | 100539.93 | 5.81 | 0.01886 |
| BE | 76612.87 | 1 | 76612.87 | 4.42 | 0.03937 |
| ABE | 710.25 | 1 | 710.25 | 0.04 | 0.84015 |
| CE | 1114.53 | 1 | 1114.53 | 0.06 | 0.80054 |
| ACE | 26986.29 | 1 | 26986.29 | 1.56 | 0.21644 |
| BCE | 74388.48 | 1 | 74388.48 | 4.3 | 0.04224 |
| ABCE | 3567.04 | 1 | 3567.04 | 0.21 | 0.65146 |
| DE | 2590.02 | 1 | 2590.02 | 0.15 | 0.70023 |
| ADE | 27584.43 | 1 | 27584.43 | 1.59 | 0.21148 |
| BDE | 28161.04 | 1 | 28161.04 | 1.63 | 0.20683 |
| ABDE | 1033.07 | 1 | 1033.07 | 0.06 | 0.80782 |
| CDE | 90.68 | 1 | 90.68 | 0.01 | 0.94254 |
| ACDE | 42892.21 | 1 | 42892.21 | 2.48 | 0.12045 |
| BCDE | 45530.65 | 1 | 45530.65 | 2.63 | 0.10982 |
| ABCDE | 2.55 | 1 | 2.55 | 0 | 0.99035 |
| Error | 1108238.23 | 64 | 17316.22 | 0 | |
| Total | 1766680.92 | 95 | | | |

Table 5. ANOVA table from the design of experiments results for uncorrected temperature. P values < 0.1 are highlighted in green

| Factor | Sum of Squares | DoF | Mean Square | F0 | p value |
|--------|----------------|-----|-------------|--------|---------|
| A | 695.53 | 1 | 695.53 | 106.47 | <0.001 |
| B | 1.31 | 1 | 1.31 | 0.2 | 0.65622 |
| AB | 11.21 | 1 | 11.21 | 1.72 | 0.19496 |
| C | 25.22 | 1 | 25.22 | 3.86 | 0.0538 |
| AC | 0.48 | 1 | 0.48 | 0.07 | 0.78685 |
| BC | 1.93 | 1 | 1.93 | 0.29 | 0.58897 |
| ABC | 0.33 | 1 | 0.33 | 0.05 | 0.82377 |
| D | 20.53 | 1 | 20.53 | 3.14 | 0.08099 |
| AD | 2.94 | 1 | 2.94 | 0.45 | 0.50473 |
| BD | 23.6 | 1 | 23.6 | 3.61 | 0.06184 |
| ABD | 42.67 | 1 | 42.67 | 6.53 | 0.01299 |
| CD | 6.2 | 1 | 6.2 | 0.95 | 0.33356 |
| ACD | 8.17 | 1 | 8.17 | 1.25 | 0.26771 |
| BCD | 7.71 | 1 | 7.71 | 1.18 | 0.28149 |
| ABCD | 28.6 | 1 | 28.6 | 4.38 | 0.04037 |
| E | 1564.94 | 1 | 1564.94 | 239.55 | <0.001 |
| AE | 349.61 | 1 | 349.61 | 53.52 | <0.001 |
| BE | 1.93 | 1 | 1.93 | 0.29 | 0.58897 |
| ABE | 0.37 | 1 | 0.37 | 0.06 | 0.81141 |
| CE | 2.94 | 1 | 2.94 | 0.45 | 0.50473 |
| ACE | 0.2 | 1 | 0.2 | 0.03 | 0.86108 |
| BCE | 11.21 | 1 | 11.21 | 1.72 | 0.19496 |
| ABCE | 4.68 | 1 | 4.68 | 0.72 | 0.4004 |
| DE | 12.04 | 1 | 12.04 | 1.84 | 0.17933 |
| ADE | 10.93 | 1 | 10.93 | 1.67 | 0.20039 |
| BDE | 4.17 | 1 | 4.17 | 0.64 | 0.42746 |
| ABDE | 2.16 | 1 | 2.16 | 0.33 | 0.5673 |
| CDE | 4.33 | 1 | 4.33 | 0.66 | 0.41832 |
| ACDE | 0.01 | 1 | 0.01 | 0 | 0.96193 |
| BCDE | 0.2 | 1 | 0.2 | 0.03 | 0.86108 |
| ABCDE | 8.4 | 1 | 8.4 | 1.29 | 0.261 |
| Error | 418.09 | 64 | 6.53 | 1.29 | |
| Total | 3272.63 | 95 | | | |

Table 6. ANOVA table from the design of experiments results for corrected temperature. P values < 0.1 are highlighted in green

| Factor | Sum of Squares | DoF | Mean Square | F0 | p value |
|--------|----------------|-----|-------------|-------|---------|
| A | 319.01 | 1 | 319.01 | 0.37 | 0.54458 |
| B | 4799.68 | 1 | 4799.68 | 5.58 | 0.02119 |
| AB | 9.5 | 1 | 9.5 | 0.01 | 0.91661 |
| C | 1666.67 | 1 | 1666.67 | 1.94 | 0.16864 |
| AC | 1399.95 | 1 | 1399.95 | 1.63 | 0.20654 |
| BC | 3055.53 | 1 | 3055.53 | 3.55 | 0.06394 |
| ABC | 21.09 | 1 | 21.09 | 0.02 | 0.87602 |
| D | 1560.09 | 1 | 1560.09 | 1.81 | 0.1827 |
| AD | 70.73 | 1 | 70.73 | 0.08 | 0.77518 |
| BD | 320.47 | 1 | 320.47 | 0.37 | 0.54367 |
| ABD | 672.04 | 1 | 672.04 | 0.78 | 0.37993 |
| CD | 308.88 | 1 | 308.88 | 0.36 | 0.55102 |
| ACD | 64.03 | 1 | 64.03 | 0.07 | 0.78581 |
| BCD | 448.07 | 1 | 448.07 | 0.52 | 0.47297 |
| ABCD | 925.04 | 1 | 925.04 | 1.08 | 0.3035 |
| E | 12802.02 | 1 | 12802.02 | 14.89 | 0.00027 |
| AE | 10778.08 | 1 | 10778.08 | 12.54 | 0.00075 |
| BE | 8690.62 | 1 | 8690.62 | 10.11 | 0.00227 |
| ABE | 9.38 | 1 | 9.38 | 0.01 | 0.91716 |
| CE | 2446.22 | 1 | 2446.22 | 2.85 | 0.09651 |
| ACE | 1507.33 | 1 | 1507.33 | 1.75 | 0.19018 |
| BCE | 4053.4 | 1 | 4053.4 | 4.71 | 0.03362 |
| ABCE | 1080.04 | 1 | 1080.04 | 1.26 | 0.26655 |
| DE | 678.41 | 1 | 678.41 | 0.79 | 0.3777 |
| ADE | 889.38 | 1 | 889.38 | 1.03 | 0.31293 |
| BDE | 524.54 | 1 | 524.54 | 0.61 | 0.43762 |
| ABDE | 961.4 | 1 | 961.4 | 1.12 | 0.29427 |
| CDE | 53.4 | 1 | 53.4 | 0.06 | 0.80398 |
| ACDE | 17.51 | 1 | 17.51 | 0.02 | 0.88696 |
| BCDE | 457.63 | 1 | 457.63 | 0.53 | 0.46831 |
| ABCDE | 326.34 | 1 | 326.34 | 0.38 | 0.54001 |
| Error | 55022.53 | 64 | 859.73 | 0.38 | |
| Total | 115939 | 95 | | | |

10. Temperature Measurement

The design of experiments presented provides detailed information about the sensitivity of the measurement to different factors, and thus, a deeper understanding of the limitations of the system. It does not provide a good understanding of the actual temperature measurement capabilities. A simple test was configured using the design of experiments configuration in which the system was well aligned and calibrated. For the experiment, temperature and emissivity measurements were conducted over a range of temperatures.

The pyrometer-measured temperature was plotted against the temperature read by the thermocouple on the surface of the rod. This plot of the temperature measurements is shown in Figure 11. Both the emissivity-corrected and uncorrected temperatures are plotted. Good agreement is shown between the emissivity-corrected and the thermocouple measurements, which shows the advantage of the active pyrometer system. The measured emissivity for these measurements is shown in Figure 12. The large shift in emissivity measurement at approximately 725° C corresponds to the change in operating wavelength the pyrometer is using. For the low temperature range it uses a 1550 nm wavelength and switches to a 905 nm for the high temperature range. Even with this large change in emissivity the pyrometer is capable of accurately measuring the correct temperature.

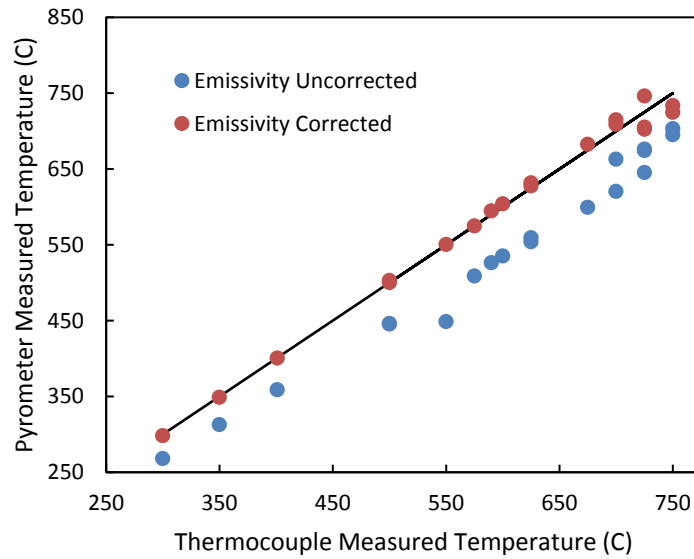


Figure 11. Plot of pyrometer measured temperature vs temperature measured by thermocouple welded on the surface of the rod. The blue dots are the measured temperature not accounting for the measured emissivity. The orange dots are the measured temperature after correcting for the measured emissivity. The black line represents a line where the pyrometer and thermocouple would be in perfect agreement.

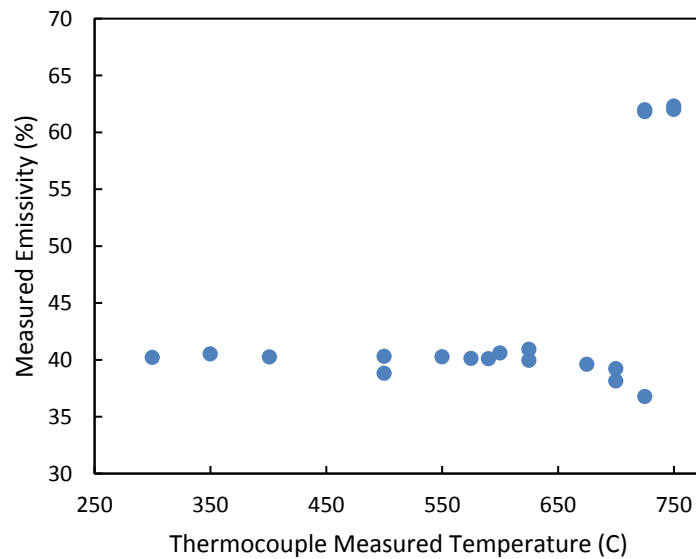


Figure 12. Plot of the measured emissivity corresponding to the measured temperatures in Figure 11.

11. Summary and Conclusions

The goal of deploying IR pyrometer technology in in-pile experiments carries with it significant challenges that may be divided into two categories: engineering challenges and measurement science challenges. Several engineering challenges have been overcome during this phase of work. A fiber-based optical line has been developed that is capable of transmitting the infrared radiation out of the experiment vehicle and reactor to the pyrometer. The optical line includes a novel optical feedthrough design that has been demonstrated to perform adequately and components that are able to withstand the PWR water conditions. This design may also be leveraged for future development of optical-based in-pile measurements.

Important measurement science challenges associated with measuring cladding surface temperature have been explored through a design of experiments analysis. The factors explored in the design of experiments include: aiming direction (angle) of each sapphire rod, the X and Y position of the surrogate fuel pin, and the surface shape (flat or cylindrical). The results show strong interaction effects between parameters in the off design conditions. The results indicate that significant error may result when two or more parameters are in an off-design condition. This error can cause an over- or underestimation of the true value, depending on the conditions. This highlights a weakness of the active systems sensitivity to alignment errors, and drives the requirement for well-controlled and precise alignment procedures.

Other supporting accomplishments are crucial to enabling proper development and meaningful in-pile deployment of pyrometer systems. These include: the establishment of in-house capabilities to manufacture low-loss, highly-repeatable optical connections and the ability to calibrate radiance and reflection measurements through the use of a newly acquired blackbody furnace and reflectance standard, respectively.

Additional experimental results have shown the capability of the active pyrometer system to measure changes in target emissivity due to surface oxidation. This feature is a key advantage of active pyrometer systems compared to passive pyrometers. Generally, several experimental tests have shown the pyrometer to function well for on-design conditions. The measurements show good agreement, over a large temperature range, between the pyrometer measured temperature and the temperature measured by a thermocouple welded to the target surface.

12. Future Work

Much work has been conducted on addressing the engineering and science challenges of deploying the active commercial pyrometer for in-pile temperature measurements in TREAT. The primary challenges that remain to be addressed are viewing under water, steam, and water phase change conditions, understanding the effects and limitations caused by the background radiation in a hot environment, and in-pile performance of optical fibers during TREAT transient irradiations.

Additionally, an alternate commercial spectral pyrometer (multi-wavelength passive pyrometer) was recently acquired that will be evaluated for in-pile temperature measurements to compare performance with the active system. The system can be seen in **Error! Reference source not found.** The advantages of a spectral pyrometer include:

- One optical line simplifying feedthroughs and the engineering design;
- Not sensitive to changes in specular/diffuse reflection properties of the material surface;
- Less sensitive to attenuation along the optical path;
- Alignment is slightly simplified because reflected light does not need to be collected.



Figure 13. Photograph of a recently acquired spectral pyrometer

With spectral pyrometers, concerns exist about the spectral influence of the water/steam environment among other emissivity determination challenges. Exploration of both systems in the experimental stations at HTTL will provide valuable comparisons of performance, especially in regards to in-pile deployment challenges, to maximize the potential of in-pile pyrometer implementation at TREAT.

13. References

- [1] Montgomery, D.C., *Design and Analysis of Experiments* John Wiley & Sons (1996)

Appendix C

Development of a Custom Infrared Pyrometer System for TREAT Experiments

2017 Annual Report

Zilong Hua, Austin Fleming, Heng Ban
University of Pittsburgh

Colby Jensen
Idaho National Laboratory

Table of Contents

| | |
|---|----|
| Abstract | 1 |
| 1. Introduction | 1 |
| 1.1 Objective | 1 |
| 1.2 Infrared Measurements | 1 |
| 2. Measurement Mechanism | 2 |
| 3. System Design | 3 |
| 3.1 System Design and Analytical Performance Model | 4 |
| 3.2 Proof-of-Concept Measurement System Design | 8 |
| 4. Experimental Testing | 8 |
| 4.1 Radiance Measurement Calibration & Testing | 8 |
| 4.2 Active Emissivity Measurement Calibration & Testing | 11 |
| 4.3 Combined Emissivity and Temperature Measurement Calibration & Testing | 13 |
| 5. Conclusion | 17 |
| 6. References | 17 |

Abstract

A high-speed infrared (IR) thermometer system (pyrometer) has been designed for in-pile measurement of cladding surface temperature in transient irradiation experiments. A theoretical model has been developed to estimate system performance, aid system component selection, and define expected uncertainties over the targeted temperature range. The primary principle of operation has been studied experimentally to demonstrate proof-of-concept in addition to initial component-level testing. This measurement technology leverages advantages of existing active mode pyrometer technology with modifications to optimize performance for in-pile applications. The spectral emissivity is measured through the use of a modulated infrared laser. Simultaneously, emitted thermal radiation heat flux is measured and used to calculate the targets surface temperature based on Planck's Law. The final objective of the project is to build a local non-contact temperature measurement system for in-pile applications, capable of temperature measurements in the range of 300°C – 1600°C with < 1 ms temporal resolution.

1. Introduction

The development of a custom approach to perform temperature measurements is a key component of the strategy to enable non-contact temperature measurements for nuclear fuel experiments. This work is being carried out in parallel to the experiment qualification efforts being performed at INL to support deployment of commercial systems that have been adapted in an attempt to meet the needs of the transient testing program. Due to the varied and unique requirements of in-pile experiments, the custom system will provide a flexible and expandable platform that may be adapted to specific experiment needs such as varied temperature ranges, optical line requirements, calibrations needs, environmental considerations such as under water/steam viewing and irradiation effects, etc. In particular, development emphasis is placed meeting the time response requirements of transient experiments as no other commercial technology can currently fully address.

1.1 Objective

The objective of this project is to develop, build, calibrate, test and optimize a non-contact, high speed, optical fiber based radiometry temperature measurement system that can be used in a test capsule or water loop for transient reactor testing (TREAT) facility. The application can be measuring cladding outer surface temperature in air or water without the need to attach the sensor to cladding, or selected locations inside fuel pellet with sub-microsecond resolution.

The scope of work is to design, build, and test/calibrate a custom pyrometer system. The target performance specifications for the system are:

- Spatial resolution: 200 micron to millimeters,
- Temporal resolution: < 1 millisecond resolution,
- Measurement temperature range: 300°C-1600°C (2000°C desired),
- Compatibility with optical fiber lines, feedthroughs for use in a water environment with temperatures of up to 350°C and pressures from atmospheric to 15.5 MPa.

1.2 Infrared Measurements

Thermal radiation is emitted from all objects with the temperature above absolute zero. Based on Planck's Law, the radiation heat flux of an object at a particular wavelength or wavelength band is a function of temperature and thus can be used to determine the temperature of the target object. There are two general types of pyrometers, active and passive. Passive pyrometers operate without the use of any external radiation sources. Active pyrometers typically use a laser reflected off the sample surface to aid in

the determination of emission properties. The thermal radiation from an ideal emitter, often called a blackbody, follows Planck's Law identically. For non-blackbody objects, the emitted thermal radiation is related to Planck's Law by the materials emissivity. To determine temperature using pyrometry, the sample's emissivity needs to be known, measured, or assumed. Emissivity is a function of the wavelength, temperature, and direction. On most commercial passive pyrometers, the emissivity of the sample is either assumed known at the given wavelength (single-band passive pyrometer), or assumed identical at two wavelengths (dual-band passive pyrometer). Accurate temperature results cannot be obtained if the emissivity cannot be determined. Another design of a passive pyrometer measures radiation heat flux at hundreds of wavelength bands and uses a multi parameter fit to determine emissivity.

An active pyrometer is an excellent candidate to provide accurate temperature measurement capability for in-pile applications. Compared to passive pyrometers, active pyrometers use a light source (e.g., laser) to perform a real-time emissivity measurement. The detailed measurement mechanism will be described in the following sections. One unique advantage of this custom designed pyrometer system is that the emissivity measurement accuracy is improved through the use of a lock-in amplifier. The lock-in amplifier has an extremely narrow frequency bandwidth to significantly increase (order of magnitude) the signal-to-noise ratio of the periodic signal measurement. This advantage is expected to be critical to deal with samples with a moderate-to-high emissivity at high temperatures.

2. Measurement Mechanism

The spectral radiance of a body, or the radiant heat flux of different wavelengths, can be calculated from Planck's Law as follows:

$$B_{\lambda}(\lambda, T) = \varepsilon_{\lambda} \frac{2hc^2}{\lambda^5} \frac{1}{e^{\frac{hc}{\lambda k_B T}} - 1} \quad (1)$$

In Eq. (1), λ is the wavelength, T is the body temperature, and ε_{λ} is the spectral emissivity in wavelength; h is the Planck constant, c is the speed of light in the medium, and k_B is the Boltzmann constant. As h , c , and k_B are all known constants, and λ is adjustable and can be considered as a known parameter, T can be obtained by measuring B_{λ} and ε_{λ} . A complete measurement will theoretically need to collect all radiation heat from the sample by using a sphere or hemisphere receiver. In the actual radiometry system, only a small portion of the radiation heat flux reaches the detector sensor. Therefore, the heat flux onto a given area and solid angle, and the spectral directional emissivity ($\varepsilon_{\lambda, \theta}$), are used instead of the total radiance and (total) spectral emissivity in the design and calculation.

One method to obtain $\varepsilon_{\lambda, \theta}$ is to calculate it from the spectral directional reflectivity ($\rho_{\lambda, \theta}$) measurement. In such a measurement, the light from an external source (i.e., laser with the same wavelength of the measured heat flux) reflected off the object surface is monitored to calculate $\varepsilon_{\lambda, \theta}$ as follows:

$$\varepsilon_{\lambda, \theta} = \alpha_{\lambda, \theta} = 1 - \rho_{\lambda, \theta} - \tau_{\lambda, \theta} = 1 - \rho_{\lambda, \theta} = 1 - k \times \rho_{\lambda, \theta}' \quad (2)$$

In Eq. (2), $\alpha_{\lambda, \theta}$, and $\tau_{\lambda, \theta}$ are spectral directional absorptivity and transmissivity, respectively. As any radiation can only transmit through, be absorbed or reflected by an encountered object. The summation of absorptivity, reflectivity and transmissivity is always 1, as shown in Figure 1. As the tested sample is assumed opaque, $\tau_{\lambda, \theta}$ will be 0, and $\varepsilon_{\lambda, \theta}$ is always equal to $\alpha_{\lambda, \theta}$. In the last part of the equation, $\rho_{\lambda, \theta}'$ is the relative spectral directional reflectivity, which will be transiently measured in the active pyrometer system, and k is a parameter related predominately to the surface roughness influencing the degree to which the reflected light is scattered. If the sample surface specularly reflects light, then the parameter k would have a value of 1. If the sample reflects perfectly diffuse, then this parameter is dependent primarily on the detection surface area and distance from the sample. However, in reality most samples do not have perfectly

specular or diffuse reflections, and are actually a combination of the two. This should be taken into account in the calibration process. A calibration sample with similar surface qualities is needed to calibrate this parameter.

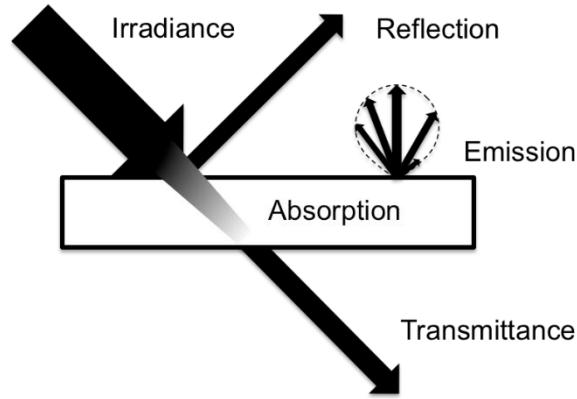


Figure 1. When radiation encounters a solid medium, it will transmit through, be reflected, or be absorbed. Thus, $\tau + \rho + \alpha = 1$; emissivity is always equal to absorptivity for given wavelength and direction. Emission is direction-dependent.

In the measurement, the output power of the external emitter will be modulated by an optical chopper to produce a periodic square-wave before reflecting off the sample surface. Three signals will be measured in order to determine the sample temperature: S_0 – the radiation emitted by the laser, S_ρ – the radiation from the laser reflected by the sample, and $S_e + S_\rho$ – the summation of the emitted radiation from the sample and the reflected laser light. In post-processing data, S_0 and S_ρ will be used to calculate $\rho_{\lambda, \theta}$ and thus $\varepsilon_{\lambda, \theta}$ from Eq. (2). Using the measured emissivity, the temperature, T , can be calculated from S_e as

$$T(\lambda) = \frac{\frac{C_2}{\lambda}}{\ln \left(\frac{f' \times \frac{C_1}{\lambda^5} \left(1 - k \times \frac{S_\rho}{S_0} \right)}{S_e} + 1 \right)}. \quad (3)$$

where f' is a systematic parameter obtained from calibration, which accounts for the measurement wavelength bandwidth, effective detection area and solid angle of the receiver, and transmission losses; k is a geometric parameter that can be obtained from calibration; and

$$C_1 = 2hc^2$$

$$C_2 = \frac{hc}{k_B}$$

3. System Design

An active pyrometer system has been designed based on the measurement theory discussed in the previous section. Analytical models have been used to predict system capabilities and limitations based on vendor-supplied component specifications. This section discusses the detailed calculations performed to account for transmission losses through the optical path and the performance of electronic components. The selected parts and specification for the final design are provided with performance predictions. Finally a proof-of-concept system is design is provided with some modifications from the final design in order to quickly and economically test the operating principle and system.

3.1 System Design and Analytical Performance Model

The radiation heat flux intensity from the target is considered to be the most critical design parameter. Theoretically, both heat flux intensities of S_e and S_p need to be considered to provide an adequate signal to noise ratio in the design procedure. Though, laser power may be adjusted to suit specific configuration requirements, and the use of a lock-in amplifier will significantly increase the ability to detect small signals from the modulated laser. Therefore, the detection of the emitted thermal radiation will be the theoretical limiting parameter for the operation of the pyrometer. Because of this requirement, the measurement wavelength is a primary design parameter, by which the system design selections will be based. It will be shown in the following section that the measurement sensitivity and accuracy strongly depend on the measurement wavelength.

Figure 2 presents an overview of the current design for the high-speed lock-in IR pyrometer. Based on the design, all system components selected are listed in Table 1. A single fiber design is preferred to facilitate experiment integration. However a two-fiber design may be used if internal reflections in a single fiber become a problem, one fiber to deliver the laser to the sample and the other one to receive reflected laser light and sample emission. The temperature range is based on the fuel cladding temperatures in the reactor, which is 300°C – 1600°C during the reaction and up to 2000°C and beyond in extreme cases. From Wein's displacement law, the corresponding wavelength region that covers the peak of the spectral radiance in this temperature range is 1 – 5 μm . A low NEP (Noise-Equivalent-Power), Thorlabs' thermoelectrically cooled low-noise InGaAs photodiode detector (model PDA10DT) was selected with a measurement wavelength range of 0.9 – 2.57 μm . Its internal integrated amplifier can amplify the signal with a gain up to 4.75×10^6 V/A.

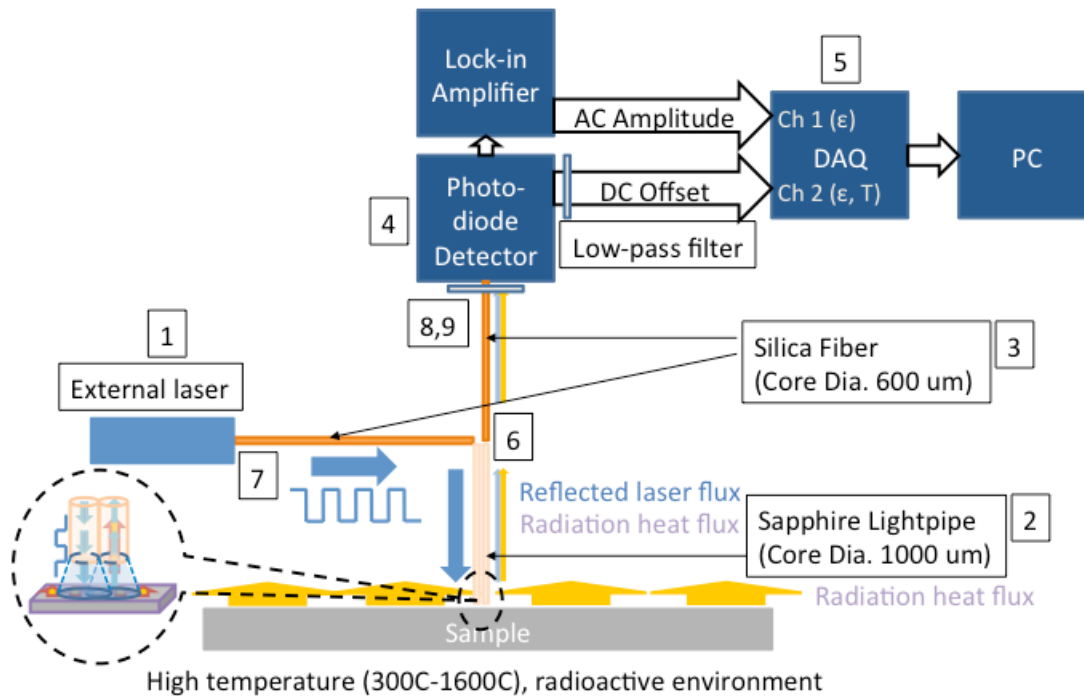


Figure 2. Schematic overview of fast response lock-in IR pyrometer. The numbered components correspond to values given in Table 1.

Table 1. List of system components for active pyrometer system

| Components | Vendor/Model | Price | Note |
|------------------------|--|-----------------|---|
| 1 – IR laser @ 2450 nm | SensAline (10mW, 5% power stability, free space) | \$5,500+\$2,700 | |
| 2 – Sapphire fiber | PhotransD | \$600/m×2 | Good performance in water/steam |
| 3 – Silica fiber | | \$20/m×5 | Good transmission loss at 1-3µm |
| 4 – Detector | Thorlabs PDA10DT | \$1,960 | Peak at 2.2 µm, up to 2.6 µm, responsivity = ~1.2 A/W, with amplifier (1.51 kV/A) |
| 5 – DAQ | NI PCI-4474 | \$3,200 | 24-bit, 102 kS/s, 1.2 µV sensitivity, 4 channels, simultaneous sampling |
| 6 – SMA/SMA connector | Thorlabs ADASMA | \$15.6×2 | 1.5 dB loss (30%) |
| 7 – Fiber coupler | Thorlabs PAF-SMA-11-D/E | \$394/741(×2) | 0.5 dB loss (11%) |
| 8 – Fiber adaptor | S120-SMA | \$38 | |
| 9 – Optical BP filter | Spectrogon | \$300 | 2300±50 nm, 85% |

The radiance increases monotonically with temperature, with the maximum design radiance being reached at 1600°C. The radiance at 1600°C can be more than six orders of magnitude higher than at the lower bound of 300° C, depending on the wavelength. Based on Planck’s Law, the ratio of the maximum to the minimum spectral radiance in this wavelength range decreases monotonically with the wavelength, from $\sim 1.36 \times 10^7$ at 1 µm to $\sim 7.5 \times 10^2$ at 2.5 µm. Considering that signal levels will be small at the lowest temperatures and with large signal variation over the entire temperature range, both detector and DAQ needs to be sensitive over a large dynamic range. Commercial components meeting these requirements are not readily available. Because of this large dynamic range, a longer measurement wavelength is preferred in this design.

Cladding temperature measurements are desired in both dry and wet experiment vehicles in TREAT. Careful selection of wavelength is necessary to minimize the influence of steam absorption on the temperature measurement. In Figure 3 the transmission through steam is shown over a range of wavelengths. The wavelength band around 2.3 µm would be ideal for the measurement for its longer wavelength. The band near 1.6 µm is also feasible but would require a larger dynamic range for the electronics to span the entire targeted temperature range. Radiation effects are not expected to be of major concern in TREAT, however, with broader long-term implementation in mind, they may also play a role in wavelength selections for the final design. This consideration would tend to push wavelength selection towards 1.5 µm assuming silica-based fibers.

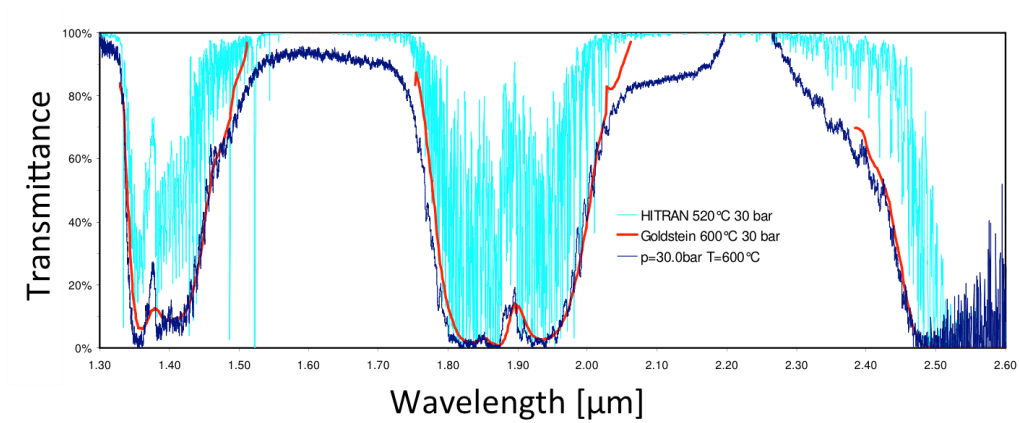


Figure 3. Simulated and experimental data of transmission spectrum of steam. High transmission regions around 1.6 μm and 2.3 μm are ideal for pyrometer measurement in a steam environment. Plot taken from [1].

To estimate system performance, the radiation heat flux (input) is calculated from the radiance (based on Planck's Law), solid angle and effective area of the detection, and sample emissivity. At 2.3 μm , the expected signal level is 1.62×10^{-7} W at 300°C, and 2.13×10^{-4} W at 1600°C at the fiber head with the following assumptions:

- 1) the optical fiber has a diameter of 1000 μm and NA of 0.12;
- 2) the working distance between the fiber head and the tested object surface is 5 mm;
- 3) the emissivity of the tested object surface is ~ 0.5 , and the measurement wavelength bandwidth is 50 nm (2300 ± 25 nm).

Transmission losses at 2300 nm for various fiber types are: 5.5% per meter for the fluoride fiber, $\sim 10\%$ for the silica fiber, and 20% per meter for the sapphire fiber. Based on design input from Idaho National Laboratory (INL), sapphire and silica fiber are assumed to make up the optical line. Assuming that the total lengths of the sapphire fiber and silica fiber are 0.5 m and 6 m, respectively, and the losses at the fiber connection and at the bandpass filter are 30% and 25%, respectively, the radiation heat flux signal at the detector input can be calculated as approximately 3.78×10^{-8} W at 300°C and 4.96×10^{-5} W at 1600°C. These calculations are summarized in Figure 4. With a low-pass filter embedded in the detector, equivalent noise level of the detector in our design is calculated to be 1.8×10^{-10} W, and thus the minimum signal-to-noise ratio of the measurement is approximately 210.

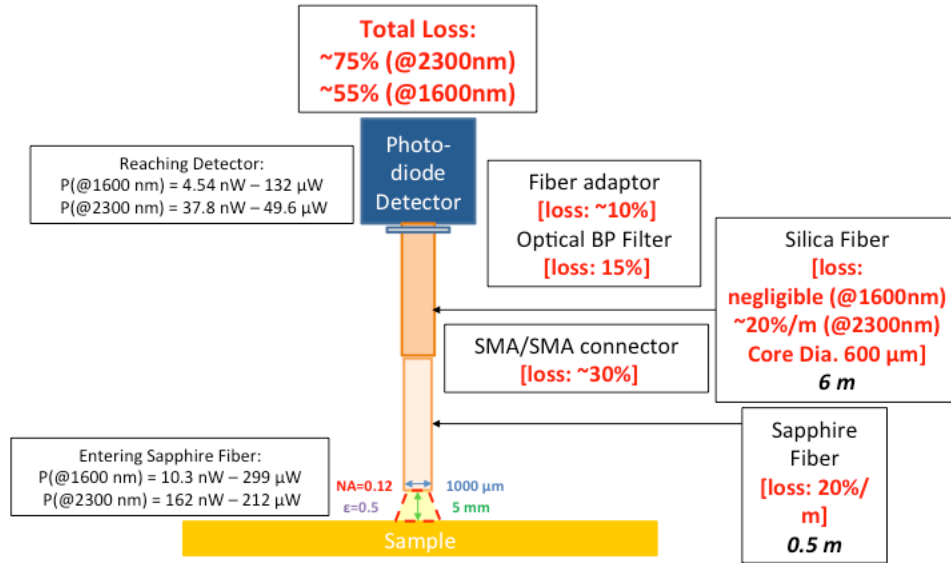


Figure 4. Graphical description of model used to predict detector signal.

After the signal is converted and amplified by the detector (with the gain of 151 kV/A, and responsivity of 1.25 A/W), it will be split into two parts to measure the emission heat flux and emissivity (reflectivity) respectively. One part is measured by the DAQ directly which is estimated to be ~7.13 mV at 300°C, and ~9.36 V at 1600°C. The DAQ selected for the current design, National Instruments PCI-4474, has a range of 10 V and sensitivity of 1.2 μV. The other part is measured by the lock-in amplifier to extract the real-time emissivity. The lock-in amplifier acts as an extremely narrow bandpass filter at the modulation frequency. This filters all other frequencies in the electrical signal and significantly improves the signal-to-noise ratio. The actual signal amplitude will depend on the final experimental setup layout. The output from the lock-in amplifier is measured by the DAQ on a second channel so all data acquisition will be performed through the one unit for ease of synchronization. This analysis is summarized in .

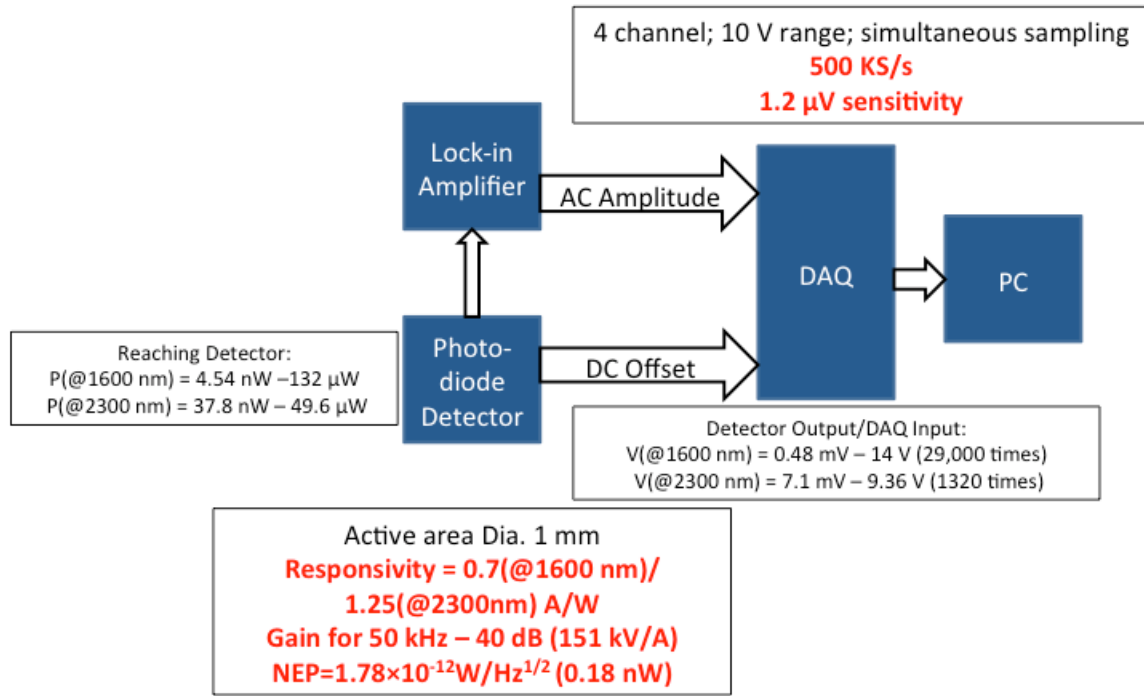


Figure 5. Graphical description of model used to predict data acquisition requirements based on the detected signals calculated in Figure 4.

3.2 Proof-of-Concept Measurement System Design

To minimize the risk in the development process, a proof-of-concept design is developed based on the final design. The primary motivation for this design is to reduce cost and lead time of some of the components, while still evaluating key features of the design. The major modifications in the proof-of-concept design are the working wavelength and removal of the sapphire fiber. A wavelength of 1550 nm is selected because lasers are readily available (short lead time) and inexpensive as compared to 2300 nm. Sapphire fiber is not necessary in the absence of the PWR conditions experienced in the TREAT experiment vehicle. An optical chopper is used for the laser modulation in the proof-of-concept testing, because they are inexpensive and easily accessible. This limits the modulation frequency, but the lock-in detection measurement can be conducted in the same manner regardless of the frequency.

4. Experimental Testing

For proof-of-concept, the radiance and emissivity measurement capability must be demonstrated. In the following subsections the radiance calibration and measurement procedures will be discussed, followed by a detailed discussion of the emissivity determination and calibration procedure.

4.1 Radiance Measurement Calibration & Testing

Two calibration parameters are required to perform a radiance measurement using a photodetector. An additive parameter is necessary to shift the measurement reference level. This parameter is required because the DC voltage offset of the photodetector is arbitrary and does not correspond to a zero radiance condition. The second parameter is a scaling parameter (related to f' in Eq. (3)) which accounts for view factors, detector sensitivity, amplifier gain, detection area, and optical transmission. These two parameters are determined by fitting the theoretical model to the experimental data taken over a range of temperatures.

A blackbody furnace will be used for radiance calibration of the final pyrometer system, but for the proof-of-concept testing a temperature controlled stage (Linkam Scientific, model FTIR 600) is used. The temperatures used for calibration ranged from 200° C to 500° C with a resolution of 25° C. The radiation heat flux signals were recorded every 25°C after the steady state is reached. The radiation heat flux was measured at two bandwidths, 1550±40 nm and 2370±35 nm, through the use of optical bandpass filters. This procedure was conducted with a silver and a glassy carbon target.

Figure 6 shows a photograph of the setup used for this testing. The fiber head is located normal to the heating stage separated by a couple of mm. The light collected by the optical fiber is transmitted to the amplified photodetector, and the result is recorded by the DAQ. The gain of the detector amplifier was set to 70dB (4.75×10^6 V/A), and the frequency bandwidth setting was 500 Hz (narrowest to minimize noise).

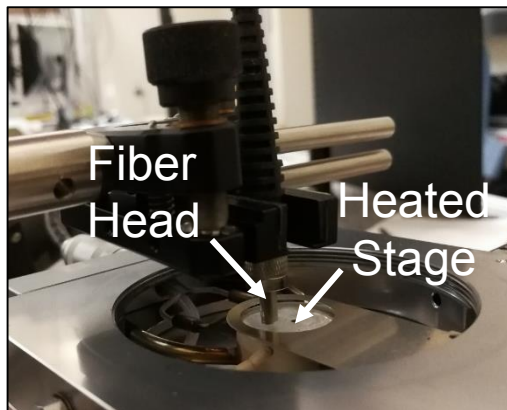


Figure 6. Photograph of the experimental setup for doing radiance measurements showing the relative positions of the fiber head and the heated stage surface.

One set of processed data obtained at 1550 nm is shown in Figure 7, with the calculated signal level for comparison. Each spot on the experimental data curve is averaged for 10 seconds after steady-state is reached. The post-processed experimental data is below noise levels zero at temperatures < 350°C. This is due to a limitation in photodetectors relating to their dark current. This low temperature error is a limitation of the 1550 nm operating wavelength. High measurement temperatures are required for further exploration at this wavelength.

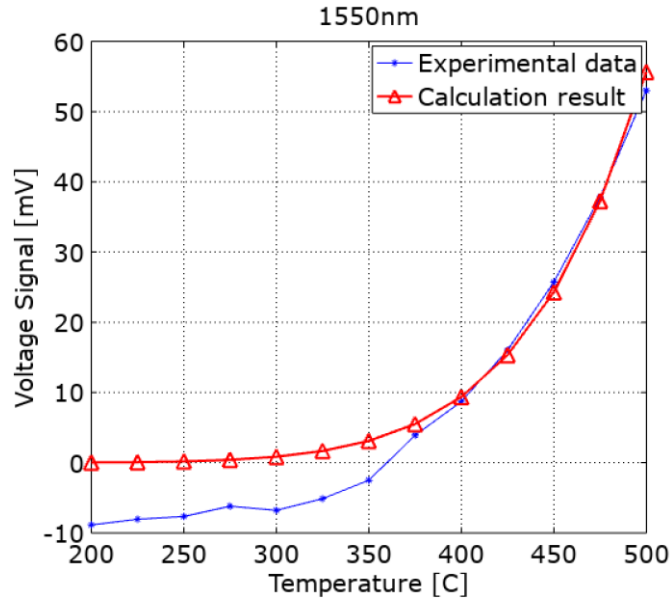


Figure 7. Comparison of the experimental and calculated results at the wavelength band of 1550 nm. The data are collected with an increment of 25°C.

The data obtained at around 2370 nm shows a smaller overall deviation from the calculation (as shown in Figure 8) comparing with at around 1550 nm, thanks to the higher signal level due to the longer operating wavelength. Therefore, the lower end of the measureable temperature range is extended to ~200°C. It displays the importance of using a longer operating wavelength for accurate temperature measurements at low temperatures. The scaling calibration parameter for the 2370-nm measurements is found to be ~150% larger than the one of the 1550-nm measurement. It is the combined effect of the transmission loss, bandpass filter transmission, detector responsivity, and emissivity differences at two wavelengths.

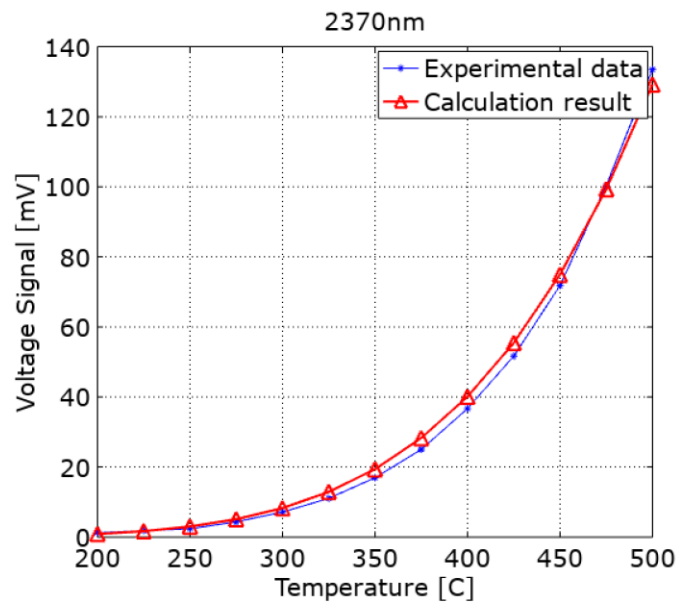


Figure 8. Calibration obtained for the 2370 nm operating wavelength

The high uncertainty level in the measurement at the shorter wavelength and lower temperature is a shortcoming found in the radiance measurements. For instance, the measured signal of experimental data at 350°C with the wavelength around 1550 nm has an average level of ~25.4 mV, while the offset factor is ~20 mV, which leaves the actual signal level to be ~5.4 mV. The uncertainty from the same measurement is approximately 2.5 mV, close to 50% of the actual signal level. This uncertainty on voltage propagates to a temperature uncertainty of ~ -50°C or +25°C under those specific conditions. This problem can be solved or generally reduced by increasing the experimental signal-to-noise ratio, such as using a longer wavelength or capturing more radiation heat flux (e.g., using the fiber with larger diameter and higher NA, etc.).

4.2 Active Emissivity Measurement Calibration & Testing

The active emissivity measurement used in this design is conducted by measuring a modulated laser reflection off the target surface. A novel approach using lock-in measurement technique is used to measure the reflected signal with high sensitivity. The measurement of this reflection is dependent on the sample reflectivity and surface roughness properties. The simplest case results when the target specularly reflects the laser light with little scattering. In this case the reflectivity is easily measured because most of the reflected light can be more easily captured by a photodiode. This measurement is then compared to a measurement of the laser beam prior to the reflection. The ratio of these measurements provides the targets directional reflectivity and therefore emissivity. An alternative case exists when the target reflects the light diffusely. If the magnitude of reflection is independent of direction (random) then a photodiode measurement, from any angle, can estimate the reflectivity of the sample. For diffuse reflection calibration a sample of known reflectivity is needed for a proper calibration. In practice real targets are neither perfectly specular nor diffuse. The best way to calibrate the active measurement for the real measurement scenario is to use a calibration sample, with known reflectivity, with similar surface roughness. Therefore, the specular/diffuse directional reflection will be similar to the conditions experienced in the actual measurement environment.

An experimental setup was built on an optical table to test the concept of active emissivity measurement based on lock-in detection. This setup used a free space 1550 nm laser and an optical fiber coupled to a photodiode for detection. The laser was periodically modulated by an optical chopper, and the output from the photodiode detector was measured by a lock-in amplifier.

A photograph of the experimental setup can be seen in Figure 9. Reflectivity measurements were performed on several materials exhibiting a range of values for reflection. The materials measured include Ag, Cu, Al, Ni, glassy carbon, and aerosol deposited graphite. In addition to the range of reflectivity values, these samples also contained various specular/diffuse reflection properties. An example of the signal recorded by the DAQ and lock-in amplifier can be seen in Figure 10. The magnitude of the modulation is easily extracted by the lock-in amplifier with very little noise.

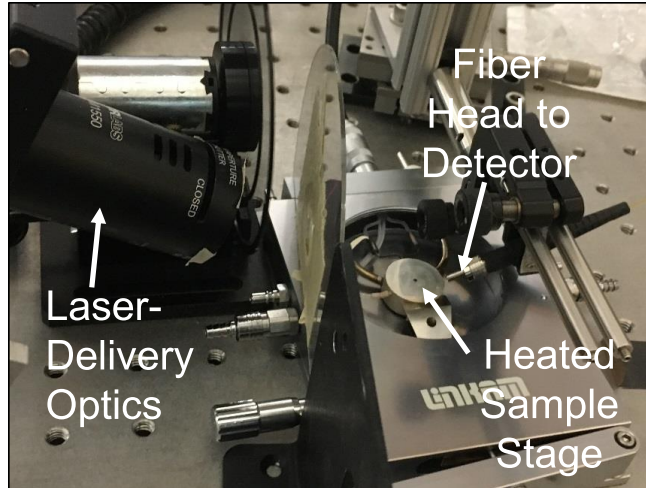


Figure 9. Photograph of the active pyrometer setup used to test concept of lock-in detection.

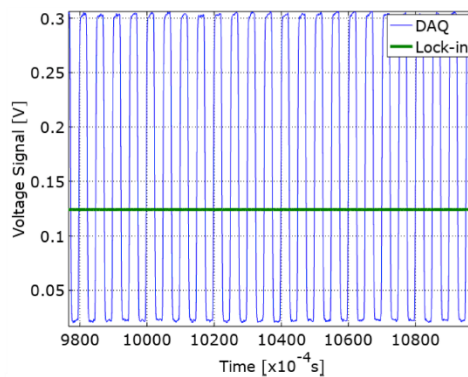


Figure 10. Segment of the experimental data obtained from DAQ and lock-in amplifier illustrating clean signal detection with little noise.

The results from the active emissivity/reflectivity measurements are summarized in Table 3. The lock-in amplifier measured square-wave amplitude is less than 2% from the amplitude extracted from the DAQ measurements. The primary advantage of the lock-in amplifier, the significantly higher signal-to-noise ratio. This benefit is clearly visible through the measurement standard deviation seen in the table. The measurements conducted on Ag show a signal to noise ratio approximately 20 times larger when measured with the lock-in amplifier compared to the measurement by the DAQ. The reflection signal level on samples with low reflectivity is too low to extract amplitudes from the DAQ data, but the lock-in amplifier was still able to extract reasonable results. As a conclusion, the lock-in amplifier greatly improves the emissivity measurement accuracy, and it is particularly necessary for measurements on samples with poor reflection (high emissivity). This is even more advantageous at high temperatures where the emitted radiation may be much higher than the reflected radiation. In these scenarios the measured signal may be over an order of magnitude larger than the modulated reflected signal.

Table 2. Comparison of the amplitude measurement results by using the DAQ and the lock-in amplifier. The lock-in amplifier exhibits a much lower standard deviation resulting in a higher signal to noise ratio. The small amplitude of reflection on the graphite and carbon samples made extracting the amplitude from the DAQ measurements impossible, however, the lock-in amplifier was able to still measure the value accurately.

| Material | Average Amplitude lock-in [mV] | Average Amplitude DAQ [mV] | Difference | Standard Deviation lock-in | Standard Deviation DAQ | Standard Deviation Ratio |
|----------|--------------------------------|----------------------------|------------|----------------------------|------------------------|--------------------------|
| Ag | 124.15 | 126.45 | 1.85% | 4.34e-5 | .74e-4 | 20.15 |
| Cu | 74.887 | 76.05 | 1.55% | 2.38e-4 | .13e-3 | 4.75 |
| Al | 60.924 | 61.2 | 0.45% | 2.12e-4 | .67e-4 | 3.14 |
| Ni | 102.56 | 104.4 | 1.79% | 7.29e-5 | .64e-4 | 11.85 |
| Graphite | 1.4326 | N/A | N/A | 2.e-5 | N/A | N/A |
| C Spray | 0.4079 | N/A | N/A | 4.1e-5 | N/A | N/A |

The measured amplitudes are compared to the materials reflectivity found in literature in Table 4. If all of the samples were well-aligned and the reflection was perfectly specular, then all of the measured amplitudes would correspond directly to their reflectivity. Two measurements were performed on each sample (except graphite). The differences between measurements are primarily due to variations in surface orientation. The targets tested have varying surface properties relating to their specular/diffusion reflection property. This variability highlights the need to have a good calibration based on the surface conditions experience in the measurement. The level of control needed to appropriately configure and calibrate pyrometer systems for the wide-ranging needs of irradiation testing is a strong motivation for the development of custom systems, as commercial system offer limited flexibility.

Table 3. Reflectivity measurement results summary for various materials compared to their reflectivity values from literature.

| Materials | Lock-in signal magnitude for two measurements [mV] | Reflectivity from literature (@ 1550nm) |
|------------|--|---|
| Ag (stage) | 124.15/107.20 | 0.95-0.99 |
| Cu | 74.887/143.7 | 0.85-0.93 |
| Al | 60.924/89.054 | 0.9-0.96 |
| Ni | 102.56/81.12 | 0.75-0.85 |
| Graphite | 1.4326 | 0.3-0.7 |

4.3 Combined Emissivity and Temperature Measurement Calibration & Testing

Two samples were selected for the combined emissivity and temperature measurement testing, Ag (heating stage) and glassy carbon, due to their well-defined surface condition. They also represent materials with high and low reflectivity, respectively. The measurements presented in this section are to display the ability of the active pyrometry system to extract both emissivity and temperature simultaneously. For these experiments the temperature controlled stage begins at 200° C and is heated at a rate of 50° C/min until reaching 500° C. During this time, both the measurements described in section 4.1 and 4.2 are conducted simultaneous.

The detector signal is composed of the radiance emitted from the sample and the reflected laser denoted as $S_e + S_p$ (when the laser is on). The lock-in amplifier extracts the amplitude of the modulating component

of the signal which is attributed solely to the reflected light (magnitude of $S_p/2$). The post processed data from the DAQ measures the time averaged signal from the photodetector which is expressed as $S_e + S_p/2$. The radiance is obtained by subtracting the value measured by the lock-in from the post-processed time-averaged data from the DAQ. The emissivity data is obtained directly from the voltage measured by the lock-in amplifier by the same process described in section 4.2.

For the measurements conducted in this section, the laser beam intensity is modulated by the mechanical chopper at 200 Hz. As the time constant of the lock-in amplifier needs to be 5-8 times longer than the period of the modulation frequency, the actual measurement time resolution is ~ 30 ms for measurements provided. This time resolution is more than adequate to resolve the temperature ramping rate (50°C/min) of the temperature controlled stage.

The raw data recorded by the DAQ and lock-in amplifier for the Ag target are plotted in Figure 11, and the time averaged data are plotted in Figure 12. Even from the raw data the temperature evolution through time is clearly visible. For the last 25 second of the measurement, the temperature controlled stage was held at 500°C ; this plateau is clearly visible in the data. From the lock-in amplifier data shown in Figure 12, a increase in emissivity with temperature is clearly visible.

The processed curves representing the heat flux from the experiment and calculation are compared and plotted in Figure 13. The deviation at the lower temperature end is caused by the temperature limitations imposed by the 1550 nm wavelength, similar to the radiance results shown in section 4.1.

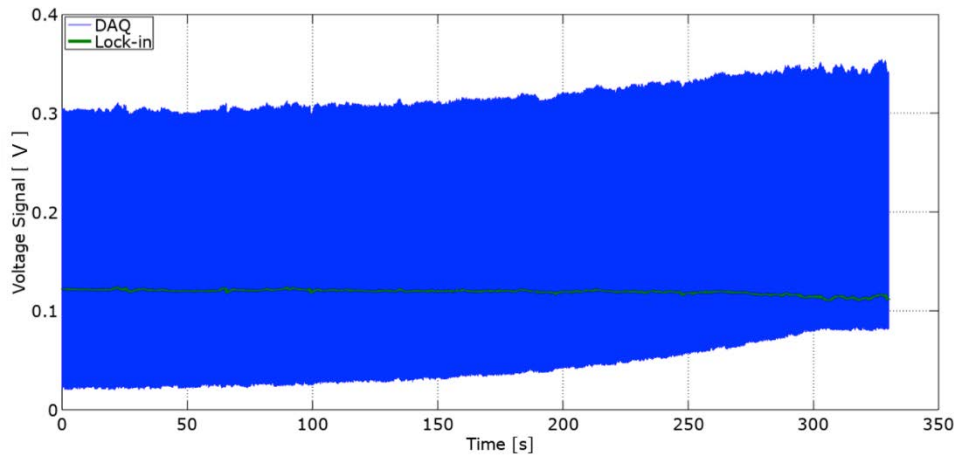


Figure 11. Unprocessed experimental data of transient temperature measurement. The measurement was performed on the calibration sample of Ag.

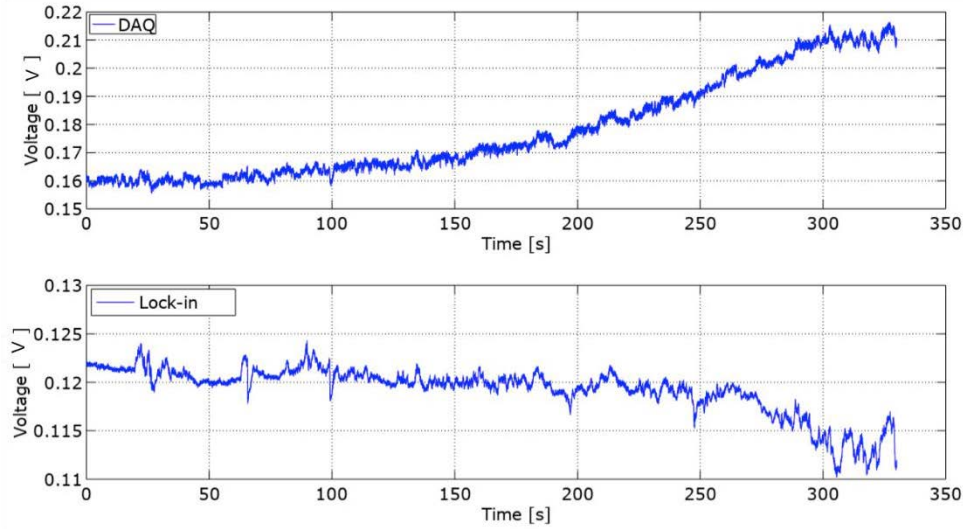


Figure 12. Processed experimental data of transient temperature measurement from DAQ and lock-in amplifier, corresponding to the offset and amplitude of the square-wave signal, respectively.

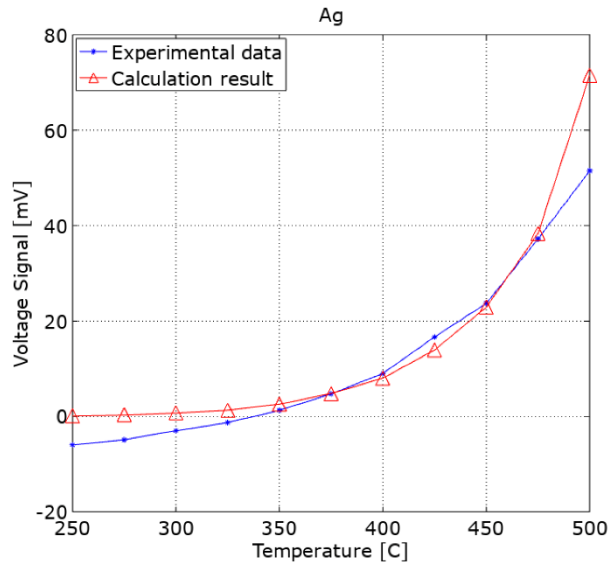


Figure 13. Comparison of calculated and measured signal levels on Ag for a range of temperatures showing improved performance away from the lower temperatures.

The same measurement procedure was conducted with a graphite sample. The measured heat flux and calculated results have a better match on the graphite sample than the results shown for Ag, as shown in Figure 14. This better result is because of a significantly higher signal level compared to that of the Ag sample, which overcomes the photodetector dark current limitations. As the graphite sample has different surface conditions, the reflection calibration coefficient, k , of graphite is found very different from Ag. The measured emissivity of graphite falls in the range of 0.283 ~ 0.4, which is lower than most literature values. This result is validated from a reference measurement by using a commercial pyrometer (~0.40 at 400°C). The low emissivity is believed to be caused by a polish treatment from the vendor. The emissivity measurement results of Ag and graphite are plotted in Figure 15.

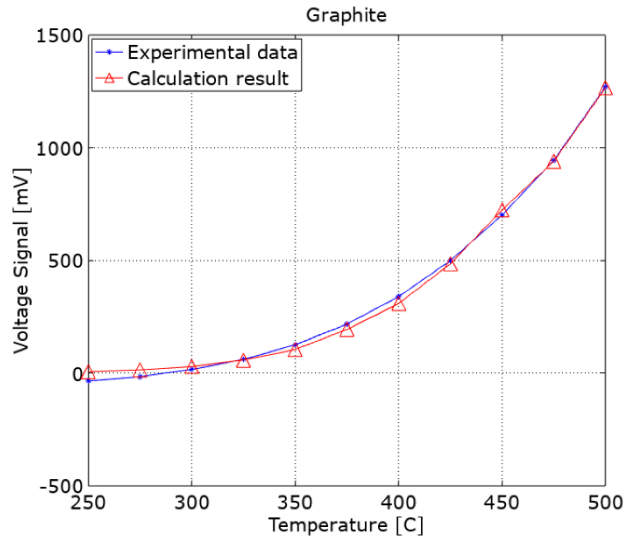


Figure 14. Comparison of calculated and measured signal levels on graphite showing very good agreement over a wide range of temperatures.

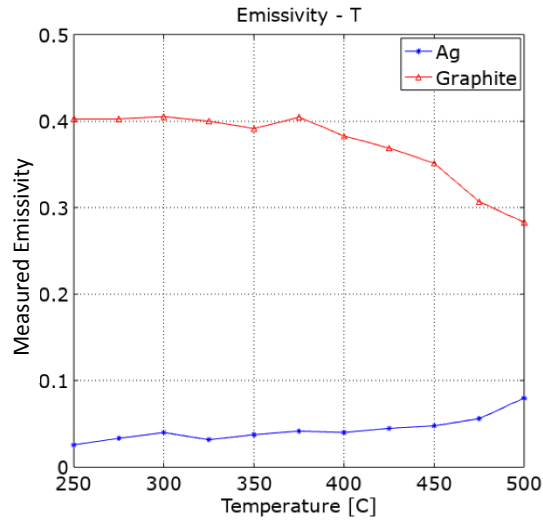


Figure 15. Emissivity measurement results with respect to temperature. The emissivity of Ag increases with temperature, from ~ 0.0256 to 0.08 , and the emissivity of graphite decreases with temperature, from ~ 0.403 to ~ 0.283 .

The results provide proof-of-concept for a lock-in based approach to active thermography and illustrate its advantage over a non-lock-in approach. However, there are some aspects that are different between the proof-of-concept testing and the final design that will influence the performance. Based on calculations, in order to accomplish the 0.1-ms time resolution, the detector gain needs to be used at the 40dB setting to obtain a sufficiently fast response time. This will reduce the amplification by a factor of ~ 31 , compared with the current 70dB gain (4.75×10^6 V/A vs 1.51×10^5 V/A). By switching the measurement wavelength back to 2300 nm in the final design, calculations show the signal level will increase by a factor of ~ 35 (8.25×10^7 Wsr $^{-1}$ m $^{-3}$ vs 2.38×10^6 Wsr $^{-1}$ m $^{-3}$). This will compensate for the reduction associated with the gain setting with the amplifier, but will provide little enhancement over the current performance. Therefore, it

is expected to have a low signal-to-noise ratio in the low temperature range (300~350°C) in the final design configuration, based on these preliminary results.

5. Conclusion

A high-speed active pyrometer system has been designed to be capable of temperature measurements from 300°C-1600°C and response time <1 millisecond. The design is based on a novel approach to active pyrometry using lock-in detection. A proof-of-concept system was built to test the measurement principle and key features of the design. The testing results from this system show good results for both active emissivity and radiance measurements. The results underlined the value of using the lock-in amplifier in the transient emissivity measurement. In some cases, the signal-to-noise ratio from the lock-in amplifier was 20 times larger than that measured by the DAQ, and in others it was able to extract the modulating signal when the DAQ could not. The results from the active emissivity measurement were able to successfully measure the temperature dependent emissivity during the experiment and results were found to be in good agreement with unrelated measurements.

Detailed calibration procedures were developed to calibrate for surface roughness, emissivity, and transmission of the optical path. Complete flexibility and control of the calibration process is not possible in commercial systems and can significantly hamper applications. The custom system allows for the measurement wavelength and other design features to be easily interchanged based on the specific needs of a given application.

In FY18, the team plans to optimize and finalize the system design and complete performance characterization studies of the final design. Specifically, the objectives are to:

- 1) Complete the final measurement system design, build, calibrate and test;
- 2) Test the final system design at the INL High Temperature Test Laboratory (HTTL) to compare performance with commercial systems.

6. References

- [1] W.F. Mohr and P. Ruffino, "Experimental Investigation into Thermal Behaviour of Steam Turbine Components, Part 1 – Temperature Measurements with Optical Probes," Proceedings of ASME Turbo Expo 2012, Copenhagen, Denmark, June 11-15, 2012.

Appendix D

Cladding Thermocouples for Transient Irradiation Experiments

2017 Annual Report

Richard Skifton, Colby Jensen

Idaho National Laboratory

Table of Contents

| | |
|---|---|
| Abstract | 1 |
| 1. Introduction | 1 |
| 2. Preliminary Work | 2 |
| 2.1 Thermocouple Type | 2 |
| 2.2 Mechanical Properties of Thermocouple Attachment..... | 2 |
| 3. Heat Transfer Considerations | 5 |
| 4. Conclusions and Path Forward | 7 |
| 5. References | 8 |

Abstract

A preliminary study of thermocouples attached to the fuel cladding during in-pile Reactivity Initiated Accident (RIA) fuel tests is presented. The thermocouples require fast response times while maintaining junction-cladding integrity during the harsh conditions of the testing environment. The recommended thermocouple configuration is bare-wire thermocouples, welded to form an integral junction with the cladding material. Thermocouple wire size is recommended as 0.005 inch, while thermocouple type is still under consideration. The type N thermocouple shows the most promise, but testing of this thermocouple and others will bring more certainty.

1. Introduction

The input provided herein is to facilitate directive in the selection of thermocouples for transient irradiation experiments in stagnant water environments (i.e. without forced convection). These experiments are to be performed in the Transient Reactor Test (TREAT) facility at Idaho National Laboratory (INL). The desired test conditions will include liquid water with initial conditions ranging from atmospheric to Pressurized Water Reactor (PWR) conditions (300°C, 15.5 MPa) with cladding surface temperatures reaching from 1000°C-1500°C depending on test-specific objectives. Cladding materials may be varied in ultimate test deployments, however, the baseline material to consider for an engineering solution is Zirconium-based alloys.

In RIA experiments, measurement of fuel/rodlet cladding temperature is critical to understanding the fuel behavior during a transient power event, as it can provide information on (but not limited to): 1) nucleate and/or film boiling, 2) maximum cladding temperature, and 3) estimated fuel maximum or centerline temperatures. Unfortunately, due to the very nature of the temperature ranges trying to be measured, drastic temporal and spatial gradients in temperature at the surface of the fuel produce large uncertainties. When purposed for cladding surface temperature, the thermocouple measurement is severely complicated by size, geometry, material interactions, chemical reactions, irradiation effects, heat loss finning effects [1], electrical interference, surrounding coolant phase change effects. An entire in-pile test series (twelve tests) was carried out at the Power Burst Facility (PBF) to study these complications and derive optimized solutions [2]. These uncertainties from both temporal and spatial sources can be minimized by adopting thermocouple configurations with cladding-intrinsic junctions, in which thermocouple wires are attached directly to the cladding such that the cladding completes the circuit.

Several in-pile transient irradiation experiments have used thermocouples for cladding surface measurements. Figure 1 shows images illustrating techniques that have been used at various transient reactors. Historical experiments at the Special Power Excursion Reactor Test Capsule Driver Core (SPERT CDC) reactor used bare-wire, integral-cladding junction, Type D thermocouples (W-3%Re/W-25%Re) in a configuration similar to what has been adopted by the National Safety Research Reactor (NSRR) with the exception of the use of Type R (Pt vs Pt-13%Rh) thermocouples. NSRR still uses this design. At PBF and Loss of Fluid Test (LOFT) facility, extensive thermocouple development including significant in-pile testing was performed for many geometrical and material design variations. At the CABRI reactor in France, experiments are performed in flowing water and thermocouple design incorporates a specially designed clip, which holds the test rod concentric in the flow tube, but also maintains pressure on the tip of a sheathed thermocouple to press it against the rod.

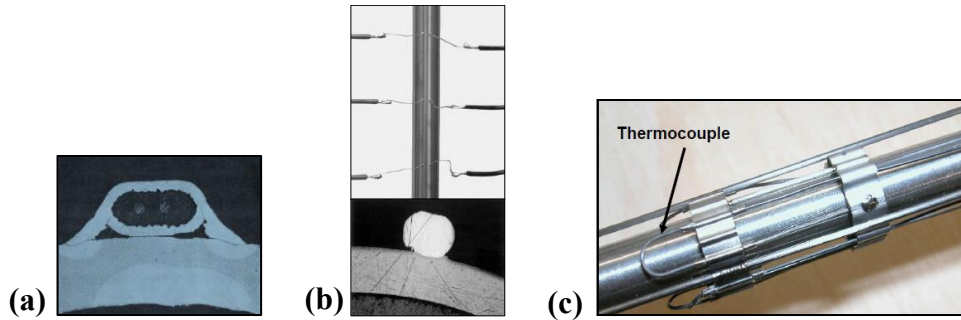


Figure 1. Examples of thermocouple-cladding attachment for various in-pile transient testing facilities. (a) Zr-sheathed, custom thermocouple laser welded to Zry cladding developed as part of the PBF/LOFT programs used in flowing water environments; (b) Thermocouples spot welded to cladding at the NSRR facility, similar design as the SPERT CDC program; (c) thermocouple clip design used in the CABRI RIA experiments, the bands press the tip of the sheathed thermocouples to the cladding surface using a ZrO₂ insulator between the clip and the thermocouple.

2. Preliminary Work

Selection of thermocouple types and mechanical connections of thermocouple-to-surface have been reviewed and partly tested. Further work in these two areas will be performed in FY18.

2.1 Thermocouple Type

The selection of a thermocouple type for testing in TREAT will depend on the expected temperature range and material compatibility with test cladding material. Literature indicates problematic adhesion for many types of thermocouples on zirconium alloys. The historical SPERT program utilized Type D (W-3%Re/W-25%Re) on Zircaloy cladding. Different types of thermocouples were tried initially, but were found to be unreliable during transient irradiation tests. These types include Chromel/Alumel, Ir/Ir-60%Rh, Pt/Pt-87%Rh. They reported difficulties creating a satisfactory bond between the thermocouples and Zircaloy cladding, causing early junction failures. The tested thermocouple materials form a low-melt eutectic with Zircaloy [3]. The initial conditions of those tests were 20°C where future TREAT tests are targeting 300°C. For more than four decades, the transient testing program in Japan at NSRR has used Type-R (Pt vs Pt-13%Rh) thermocouples welded to the cladding, forming intrinsic junctions with the surface [4]. Interestingly, platinum-zirconium has eutectic temperature of approximately 1180°C.

Ongoing studies will investigate material performance in the PWR prototypic autoclaves (i.e. temperature and pressure matching of PWRs). Also, testing will focus on attachment to Zircaloy cladding including potential impacts on surface oxidation or other coating materials. Final selection of thermocouple type for TREAT experiments will require input from the materials compatibility and weld process testing, heat transfer analysis, and approval from the fuels testing program.

2.2 Mechanical Properties of Thermocouple Attachment

The primary concerns with thermocouple attachment is mechanical stability of the thermocouple and attachment (addressed above, i.e. material compatibility with fuel cladding), time response of the measurement, heat shunting effects through the attached material, and ground loops formed through ungrounded junction attachment to conductive cladding. An additional design consideration is allowing for exposed wires to pass into the pressure vessel via Mineral-Insulated, Metal-Sheathed (MIMS) cable, such that the measurement is not affected by water ingress into cable insulation.

Alternative options considered include: 1) larger/smaller wire - tradeoff between practical implementation and mechanical stability and heat shunting effects; 2) junction-welded thermocouples with the junction welded to the cladding; 3) small, standard grounded or ungrounded sheathed thermocouples; 4) small, ungrounded, fast response MIMS thermocouple (diamond packed internal junction for fast response with approximately 0.5 mm diameter). Figure 2 provides an illustration of these different types of thermocouple junction options.

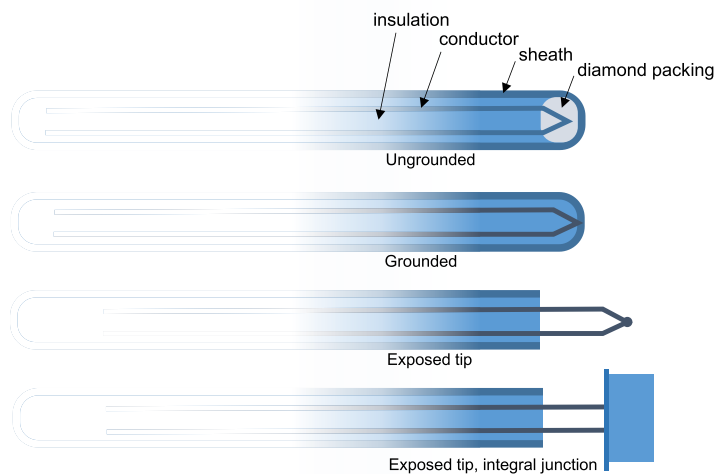


Figure 2. Illustration of options for thermocouple junction configurations

To support this selection process, testing was performed in the High Temperature Test Laboratory (HTTL) at INL. MIMS cabling with open-ends, exposing the bare wire from the thermocouples was procured from two vendors and have been tested in feedthroughs in water autoclaves at PWR conditions. A few of the desired outcomes of these tests were to ensure helium leak rates of $< 6 \cdot 10^{-6}$ atm-cc/sec, and ensure performance of the cables when exposed to high temperature and high pressure water. The setup, parameters, and results from these tests can be seen in Figure 3.

Figure 3a shows the pre-autoclave configurations of two Type K thermocouples. An unsheathed Type K thermocouple that has been laser welded together to form an exposed junction is in the top center of the picture. The thermocouple wires each have a 0.005" diameter. Just below and center to the image, an ungrounded MIMS (0.5 mm), diamond-packed thermocouple is placed with a Zirc-2 substrate attached to the very tip. The Zircaloy-2 was attached using the HTTL's laser welder and nickel filler for the bond.

Figure 3b shows the autoclave configuration and test parameters. The autoclave vessel is in the far right of the image behind the Plexiglas. The two aforementioned thermocouples can be seen standing erect above the autoclave with their connections/lead wires going to a hand held reader. At the time the picture was taken, the autoclave was slightly above PWR prototypic conditions at 2200 psig and 345°C. The duration of this test was about two hours. Figure 3c shows measured temperature from the two thermocouples, both showing good agreement with the reference thermocouple in the autoclave thermowell indicating no degraded performance from the bare wire thermocouple.

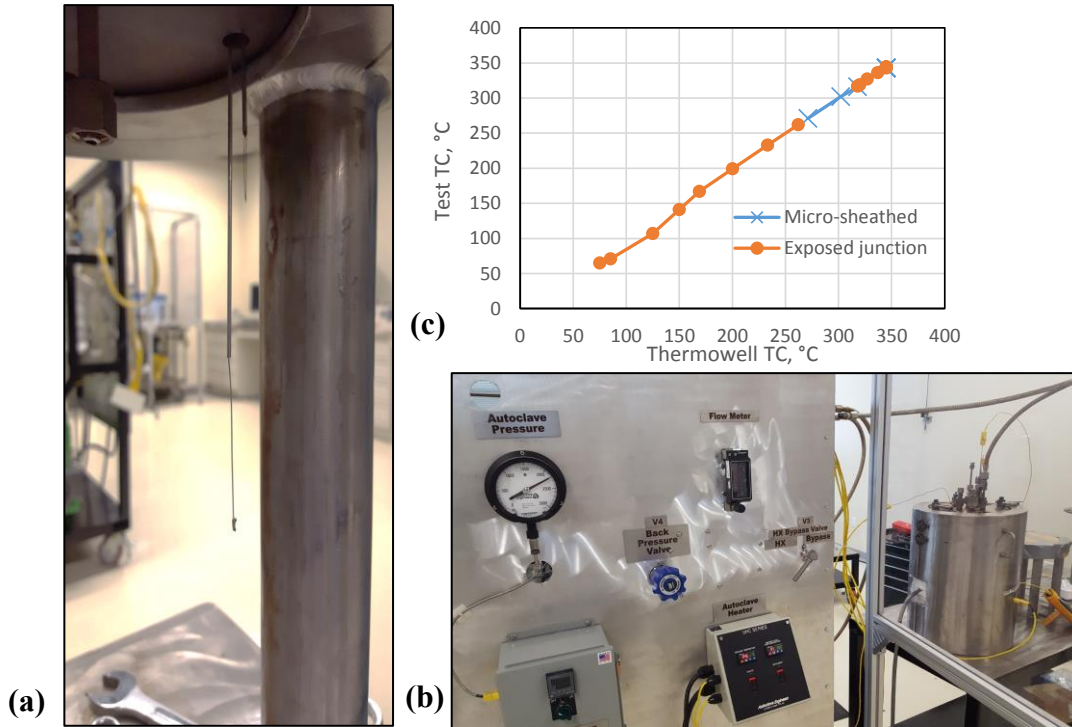


Figure 3. Autoclave testing of thermocouple junctions and exposed wire lead wire. (a) Autoclave configuration of MIMS cable and thermocouple junctions prior to PWR prototypic tests. Exposed junction type K thermocouple (upper center), and small MIMS-type (0.5 mm), diamond packed thermocouple welded to a small piece of Zry-2 (center). (b) Autoclave #2 at the HTTL during thermocouple testing at PWR prototypic conditions. Test parameters displayed shown at 2200 psig and 345°C. (c) Measured temperature comparison of small MIMS-type and exposed junction thermocouples with thermocouple output from autoclave thermowell.

Figure 4a shows the He leak rate check configuration performed after the autoclave test was completed. The exposed junction Type K thermocouple was utilized in this test in order to focus directly on the MIMS cabling, as the insulation was exposed where the bare wires protruded. The electronic quick connect was removed and one end of the cable was inserted into the bombing chamber (i.e. upper pipe) which was then put under 1,000 psig of pure He. The cabling was then bent around and inserted into the lower pipe which was under vacuum and plumbed directly into the He leak rate checker. The cabling was approximately 12" long. This configuration then stood for approximately 1 hour with the He continually trying to push through the MIMS cabling. Figure 4b shows the results of this test. The He leak rate slowly increased over the first 30 min of the hour long test, then remained fairly constant at a value well below the unacceptable value of $< 6 \cdot 10^{-6}$ atm-cc/sec.

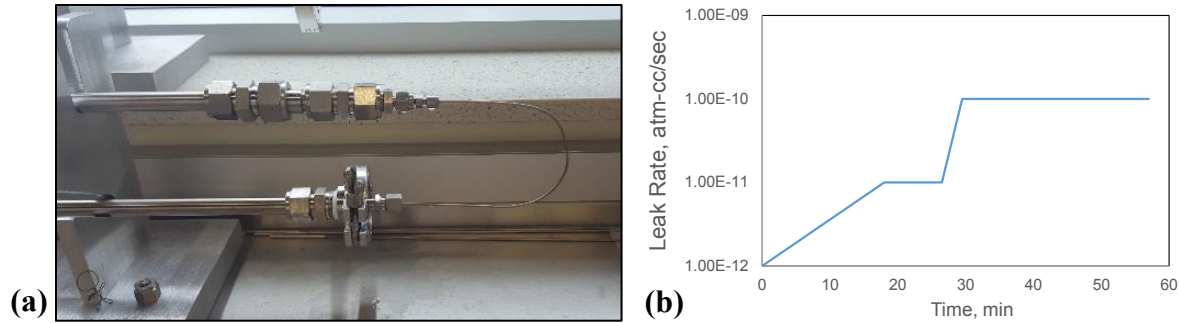


Figure 4. The testing of He passing through MIMS cabling after exposure to PWR prototypic conditions for 2 hours. (a) The bombing chamber (upper pipe) is at 1,000 psig of pure He, while the lower pipe is under vacuum – plumbed to a He Leak Detector; (b) measured leak rates far from unacceptable limits.

The integrity bond between the Inconel sheathing of the thermocouple and the Zry substrate with nickel filler remained intact after the autoclave testing. These results provide a promising first step to achieving desired thermocouple adherence and has performed well under pretest conditions of planned experiments. The precision provided by the laser welding process for the mode of attachment is viewed as a distinct advantage as compared to typical arc- or spot-welding. However, due to a lack of equipment at HTTL for spot-welding very small thermocouples, arc- and spot-welding approaches have not been properly characterized and compared in terms of form and reproducibility of the final product and potential cladding effects from weld-affected zones. Arc and spot-welding approaches will both need further exploration for final selection of the mode of attachment.

As for locating the exposed end of the sheathed portion of the thermocouples (i.e. where the exposed conductors protrude), some vessels may require extension of the MIMS cable into the liquid water region of the capsule next to the attachment location. Water ingress into the cable is a concern for creating false junctions within the thermocouple. Therefore, it is generally preferable to maintain the exposed end of the MIMS cable in the steam and/or gas regions of experiment devices. For the former, 0.010" extension wire can be placed in alumina or mullite ceramic tubing for protection and to maintain wire isolation, extending near to the attachment location where the smaller wire is welded to the cladding.

A critical consideration in the selection process will be the availability of facilities in locations where thermocouples may be attached to cladding. Assembly of fresh fuel rodlets for experiments will likely take place in a glove box. Depending on overall assembly logistics, thermocouple wires may be able to be attached to cladding prior to assembly. However, a more probable and versatile scenario is attachment of wires within the glove box. The Test Train Assembly Facility (TTAF) at the Advanced Test Reactor (ATR) complex has recently installed a laser welding facility in a glove box to enable fresh fuel rodlet fabrication. It may offer the needed capability to perform required functions for experiment assembly for TREAT tests, though some questions remain as to the welder's particular specifications for feasibility of welding fine wires. With much of the experiment assembly process occurring at the Materials and Fuels Complex (MFC), a functional micro-welding installation at a glove box facility at MFC is the preferred approach and should be considered as part of critical infrastructure needs to support TREAT experiments. Future testing of pre-irradiated rods may require capability to perform such assembly processes in a hot cell.

3. Heat Transfer Considerations

The thermocouple configuration shown in Figure 5 shows a modeled representation of an intrinsic junction which uses the substrate itself to complete the thermoelectric junction. This design allows for rapid time response and more accurate temperature readings of the targeted cladding material [5]. The wire spacing at the connection should be between 1-2 wire diameters to ensure wire separation with minimal temperature difference between the interfaces of the two leads with the cladding. The electromotive force

(EMF) generated with the introduction of an additional material in the thermocouple circuit will cancel out its effect if both ends are at the same temperature. From a thermal standpoint, the diameter of the thermocouple wires should be as small as practically feasible to minimize fin effects through the thermocouple wire. The ends of the thermocouples wires should be welded perpendicular to the surface of the prototype surrogate rod (and later on actual fuel) with minimal mass added at the weld. Each lead should be routed away from the rod to be welded to the matched, exposed leads from the epoxy-sealed MIMS cable penetrating through the vessel head.



Figure 5. A representation of an intrinsic thermocouple junction attached to a representative substrate. The targeted wire spacing is between 1-2 wire diameters.

In Henning and Parker [5], an analytical solution is presented for response of an intrinsic thermocouple junction described above. A critical thermal parameter related to time response is given in the form of

$$a = \frac{1}{1 + \frac{1}{2} \sqrt{\frac{k_T \rho_T c_T}{k \rho c}}} \quad (1)$$

where k is thermal conductivity, ρ is density, c is specific heat capacity, and subscript T is the wire properties of the thermocouple. Naturally, parameters without subscript T are properties of the substrate. The results of Equation 1 are presented in Table 1 for a variety of different thermocouples welded to Zry as the substrate. A measure of how quickly the thermocouple reached thermal equilibrium with the substrate temperature is seen in column 4 of Table 1 where

$$t_{|95\%} = \frac{25}{\pi} \frac{D^2}{\alpha} \left(\frac{k_T}{k} \right) \quad (2)$$

Here $t_{|95\%}$ is an acceptable limit for the time it takes for the thermocouple to reach 95% of the substrate temperature. Further, α is the thermal diffusivity of the substrate, and D is the diameter of the wire. For the sake of the calculated results in Table 1, the diameter of the wire is assumed to be 0.005”.

Table 1. The calculated results of Eqs. 1 and 2 utilizing room temperature properties of various thermocouples to Zirc-2 cladding.

| TC Type | Wire Mat'l | a^* | $t _{95\%} (s)^\dagger$ |
|---------|------------|--------|-------------------------|
| K | Alumel | 0.754 | 0.003 |
| K | Chromel | 0.872 | 0.002 |
| R | Platinum | 0.412 | 0.008 |
| R | Pt - 13%Rh | 0.566* | 0.005 |
| N | Nicrosil | 0.949 | 0.001 |
| N | Nisil | 0.880 | 0.002 |
| B | Pt - 6%Rh | — | 0.007* |
| B | Pt - 30%Rh | — | 0.006* |
| HTIR | Molybdenum | 0.175 | 0.017 |
| HTIR | Niobium | 0.494 | 0.006 |

*Material properties were estimated from known values in [6][7].

[†]Material properties of Zry-2 from [8]

The results of Equations 1 and 2 in Table 1 show that Type N and Type K thermocouples have the fastest response time from a pure thermal standpoint, where a closest to unity is desired. Later Gat *et al.* made further improvements to Equation 1 by applying a time marching approach to temperature dependent properties of materials while heating is applied [9] and may hold value for further investigation. Lastly, for Type B thermocouples, the thermal properties of the two platinum alloys were not found in literature. Therefore, the time response of those wires were estimated using data from [6].

Continued work should focus on a combination of experimental and analytical studies to support estimation of measurement uncertainties from implemented thermocouple configurations. Along with the theoretical studies described previously, detailed finite element analysis (FEA) of the thermocouple attachment including conduction, convection, and radiation effects can provide further insight into geometry and material effects on measurement accuracy and may also lead to correction factors for measured temperature values.

4. Conclusions and Path Forward

The development of techniques for implementation of thermocouples on fuel cladding will focus heavily on attachment to cladding materials. A range of cladding materials (prioritized as Zirconium-based alloys, stainless steels, martensitic steel (HT-9), FeCrAl, and SiC) and variations of cladding surface characteristics (coated, pre-irradiated, oxidized) should be considered. Iron-based claddings are not expected to pose much difficulty in cladding attachment in regards to high temperature failures. SiC will

require unique attachment or forced contact design. Attachment of thermocouples to claddings with unique surface characteristics will require special attention. Testing performed at the NSRR relies on a hot-cell based system to remove oxidation locally at the attachment point where the thermocouples are then spot welded to the cladding. They have reported no issues with artificially induced failures due to their procedure. Experimental studies will require evaluation of the weld affected zone of attachment using metallography, scanning electron microscopy, and other characterization techniques to define the ideal process and ensure reliable and reproducible results.

The focus of this document has been primarily for testing in high temperature, stagnant water conditions. In this case the optimal configuration has been discussed in this report, with thin bare thermocouple wires welded to form an integral junction with the cladding. This approach was used at the SPERT CDC facility and is still used at NSRR after more than five decades of testing. In the case of dry or liquid metal testing, heat transfer impacts are not expected to be as severe in terms of measurement biases and uncertainties. In these cases, miniature MIMS, ungrounded thermocouples with diamond packing at the tip may be most advantageous. However, cladding-thermocouple material (thermoelements or sheathing material) bonds will still be a concern that requires exploration. For flowing water conditions expected in the medium-term, the problem is much more complex and will require unique approaches.

Type K or N thermocouples will likely be the best option for test objectives below peak temperatures of 1372 °C, the recommended upper limit. Platinum based thermocouples (Type S, R, B) are best suited for higher temperatures up to 1768°C. With Pt-based thermocouples, the design of extension wire attachment and materials is an additional concern that must be addressed by the experiment design. Compatible extension wires of different composition (copper based) are available but have recommended working temperature ranges much closer to ambient. Test designs used at NSRR with Type R thermocouples utilize an attachment point integrated into the frame supporting the fuel, which is immersed in the liquid water within the test section of the experiment device. At this attachment point, the extension wire is attached based on the assumption of isothermal conditions at the points of attachment of each thermocouple lead wire, a reasonable assumption in stagnant liquid water with closely spaced contacts.

Ultimately, modeling and simulation will provide key estimations of biases induced by the particular thermocouple configuration and test environment and conditions. Preliminary studies can provide guidance to initial design selections and estimates of measurement uncertainties.

5. References

- [1] Tszeng, T.C., Saraf, V. *A study of fin effects in the measurement of temperature using surface mounted thermocouples*, Journal of Heat Transfer, **125**, 5, pgs. 926–935, 2003.
- [2] Garner, R. W., and MacDonald, P. E., Report NUREG/CR-2665, EGG-2190 1982.
- [3] Taxelius, T.G., “Annual Report SPERT Project October 1968-September 1969,” IN-1370, June 1970.
- [4] Tsuruta, T., Fujishiro, T., *Evaluation of Thermocouple Fin Effect in Cladding Surface Temperature Measurement during Film Boiling*, Journal of Nuclear Science and Technology, **21**, 7, pgs. 515–527, 1984.
- [5] Henning, C. D., Parker, R., *Transient Response of an Intrinsic Thermocouple*, Journal of Heat Transfer, **89**, 2, pgs. 146–152, 1967.
- [6] Laubitz, M. J., van der Meer, M. P., *High Temperature Transport Properties of Some Platinel Alloys*, Thermal Conductivity: Proceedings of the Seventh Conference Held at the National Bureau of Standards, **302**, pgs. 325–330, 1968.
- [7] Mølgaard, J., Smeltzer, W. W., *The thermal conductivity of 87% platinum-13% rhodium alloy*, Journal of the Less Common Metals, **16**, 3, pgs. 275–278, 1968.
- [8] Murabayashi, M., Tanaka, S., Takahashi, Y., *Thermal Conductivity and Heat Capacity of Zircaloy-2, -4 and Unalloyed Zirconium* Journal of Nuclear Science and Technology, **12**, 10, pgs. 661–662, 1975.

- [9] Gat, U., Kammer, D. S., Hahn, O. J., *The Effect of Temperature Dependent Properties on Transients Measurement with Intrinsic Thermocouple*, International Journal of Heat and Mass Transfer, **18** 12 pgs. 1337–1342, 1975.

Appendix E

Development of an In-Pile Boiling Detector System Based on Measurement of Electrical Impedance

2017 Annual Report

A. Fleming, K. Condie, Colby Jensen, J. Svoboda, E. Larsen, P. Calderoni

Idaho National Laboratory

Table of Contents

| | |
|--|----|
| Abstract | 1 |
| 1. Introduction | 1 |
| 2. Theory & Methodology | 2 |
| 3. Detector System Design | 3 |
| 3.1 Sensor electrodes..... | 3 |
| 3.2 Electrically insulating electrodes | 3 |
| 3.3 Measurement circuit design | 4 |
| 4. Experimental Setup | 7 |
| 5. Experimental Results..... | 9 |
| 5.1 Design of experiments | 9 |
| 5.2 Position sensitivity | 15 |
| 5.3 Transient Experiments | 16 |
| 6. Summary & Conclusions..... | 18 |
| 7. References | 18 |

Abstract

A complete boiling detector measurement system has been designed and built including sensor, electrical circuit design and setup, and data acquisition and processing software that will interface with the TREAT experiment DAS. The development and qualification of the boiling detector has progressed to an advanced stage of testing to characterize its performance using a unique, high-speed video boiling setup. An electrically insulating coating has been established through performance evaluation for use at PWR water conditions of a capsule-based experiment. This coating provides a significant enhancement of the sensor design by increasing the sensitivity of the detector to changes in the effective dielectric by reducing the sensitivity to water conductivity. A complete, packaged in-pile impedance measurement system has been designed, tested, and is now available for supporting TREAT experiments. This system is uniquely designed for in-pile use. Detailed performance characterization studies have been performed based on a design of experiments. Results quantitatively show the sensor is influenced most by the presence of a void and has significant sensitivity to the temperature of the water. Using a Teflon sleeve as a void film surrogate, good sensitivity was found when the film is located anywhere between the electrodes on the pin, with marginal sensitivity above and below the electrodes. Finally the transient response of the sensor was experimentally explored using the high speed video and quick removal of a Teflon sleeve. Though the results were not entirely conclusive, based on some assumptions, the results from this test indicate response time < 1 ms.

1. Introduction

For Reactivity Initiated Accident (RIA) events, the thermal hydraulic conditions experienced by fuel undergo a rapid transition from forced convection cooling to critical heat flux conditions. This rapid rise in heat flux in the fuel ultimately leads to film boiling conditions at the surface of the fuel clad resulting with high cladding temperatures and eventually the collapse of the surrounding vapor blanket. Though several experimental programs have been performed to measure fuel performance phenomena under RIA conditions, the time-dependent thermal hydraulic conditions at the fuel clad surface remain an area of high uncertainty [1] and thus a primary target for data collection intended for fuel performance model validation.

Performing accurate void fraction measurements in two-phase flow mixtures has long been a challenge in the thermal-hydraulic community. A number of different techniques have been developed including the wire mesh method [2], X-ray scanning method [3][4], Ultra-fast X-ray CT scanner, Gamma-ray attenuation method, Neutron radiography [5], Nuclear Magnetic Resonance (NRM) imaging [6], Bi-optical probe [7], Needle contact probes [8], Photography method, Conductance-type void fraction meter [9], Capacitance-type void fraction sensor, and ultrasonic method [2]. An exhaustive review of current void fraction measurement techniques can be found in Reference [10]. However, these methods are either invasive (i.e. disturb the flow field) or are too complex or expensive for engineering applications. Moreover, not all of these techniques are capable of real-time measurement under high-pressure and high-temperature conditions. An impedance-based sensor is an attractive solution due to the fact that it is a non-invasive measurement and can possibly meet the non-trivial functional I&C requirements imposed by RIA testing.

Impedance-based sensor (also referred to as capacitive-based sensor or boiling detector in this document) technologies are well-established for measuring void in fluid and generally used to measure phase concentrations for materials having different permittivities [11]. Cimorelli and Evangelisti (1967) [12] developed a capacitance sensor to study bulk boiling at atmospheric pressure. Thereafter, various types of capacitance sensor were developed to measure flow regime, velocity vector flow fields [13] and void fraction, including flat-plate, concave, helical and multiple helical type. Abouelwafa and Kendall (1980) [14] designed six electrode sensors to measure water-oil/water-air/oil-air two-phase flow void fraction. Shu et al. (1982) [15] performed static and dynamic calibration of their concave-type sensor for both stratified flow and vertical flow. For vertical flow, the sensor was first calibrated in a static test by inserting glass tubes into the center of the sensor and comparing with dynamic calibration tests using a quick-closing valve

technique. Because the dielectric constant of glass is slightly larger than that of air, a correction factor was proposed to account for the difference between glass and air for static calibration tests [15]. In order to improve the stability and sensitivity, Huang, S. (1986) [16] designed a guard layer on the capacitance sensor to minimize the parasitic capacitance between the sensor and the environment. One reported disadvantage of capacitance sensors is the non-uniformity of the distribution of sensitivity over pipe cross-section and therefore differing responses to different flow regimes [11][17]. As indicated by Strizzolo, C. N. and J. Converti (1993) [18] and Ceccio, S. and D. George (1996) [17], the response of concave-type sensors and ring-type sensors are strongly related to flow regime. For these sensors, the output capacitance is not proportional to the void fraction but also depends on the flow regime.

Application of a capacitive sensor for remote, *in-pile* measurement in *Pressurized Water Reactor* (PWR) conditions (15.5 MPa and 280°C) with fast response time (< 1 ms) requires significant adaptation to address environment and facility constraints. To achieve this goal, a complete in-pile boiling detector system has been designed and developed including sensor, measurement circuitry, and data processing, which can be directly interfaced to the TREAT data acquisition system. Following initial development efforts in the last fiscal year including feasibility experiments performed at PWR conditions, the continued sensor development and qualification effort has been focused on: documenting a description of complete system design, establishing a viable electrical insulating coating to use on the measurement electrodes, characterizing detector sensitivities to various environment factors including the presence of a vapor film layer on a test fuel rod, and quantifying sensor response time. This document provides a technical summary of those efforts.

2. Theory & Methodology

Impedance based measurements rely on a principle of supplying a voltage across an electrical element and measuring the current flowing across that same element. Impedance is then calculated from the ratio of voltage and current. Among many applications, measurements of impedance are made to determine the electrical properties of a component, from which, in some cases the measured electrical properties are used to determine other information about the component. For the purposes of this work, the impedance measurement is used to gain information about the gas void between the two electrodes.

The capacitance between two conductors depends primarily on the dielectric of the material between them, the distance between them, and their surface area. Equation (1) illustrates this relationship through the idealized, theoretical relationship for capacitance between two parallel plates of the same surface area

$$C = \frac{\epsilon \cdot A}{d}, \quad (1)$$

where ϵ is the permittivity of the material between the plates, A is the area of each plate, and d is the separation distance between parallel plates. The dielectric constant of liquid and vapor water are significantly different. Therefore, the amount, location and shape of voids between electrodes significantly impact the capacitive coupling. This is the technical basis for using an impedance measurement to detect vapor voids between electrodes.

For impedance measurements, LCR (inductance, capacitance, resistance) meters are often used to measure electrical components at specific frequencies. This standard equipment is similar to other impedance measurements where a voltage is supplied and a current is measured. They typically use a fixture with a four wire configuration where two of the wires supply the current and the other two measure the voltage. While an LCR meter is standard equipment and are designed to perform accurate impedance measurements, their application to in-pile measurements is limited. The impedance measurement system developed in this work is similar in operation to an LCR meter, but has some critical features that enable it to perform in-pile impedance measurements.

3. Detector System Design

Measurement of electrical impedance is a common practice with many technologies available as mentioned previously. In addition, commercial technology is available to measure voids in thermal-hydraulic systems. The design of an in-pile impedance sensor to operate at PWR conditions requires significant adaptations to withstand the environment and test overall performance at condition. It also necessitates careful design of the electrical circuitry and data acquisition to enable measurement with long lead wires inside a complex experiment device surrounded by other instruments, power cables, conductive water, and other hardware. This section details the detector design and associated requirements of the sensor.

3.1 Sensor electrodes

For an ideal sensor design, the water volume of interest would be located directly between the electrodes. With voids formed on the surface of the test fuel cladding, the ideal configuration for this measurement would be to allow electrically conductive cladding to act as an electrode and use an outer concentric tube electrode around the cladding. This configuration is not feasible due to the challenges in the in-pile experiment design to electrically isolate the cladding from the test capsule and supporting hardware. This limitation results in the requirement of using two electrodes exterior to the fuel rodlet. The current design of the boiling detector electrodes are thin, slightly curved plates located around the rodlet. For simplicity in setup and testing, the geometry for the electrodes used in the laboratory studies are located concentrically to the inner cladding surrogate rod as shown in Figure 1.

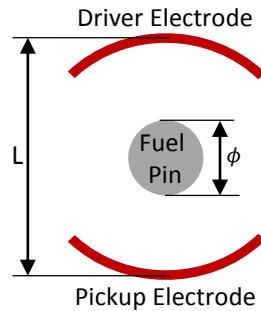


Figure 1. Diagram of the electrode geometry used in the boiling detector for laboratory studies. The fuel pin diameter, $\phi=3/8''$ and the electrode separation, $L=0.9''$

3.2 Electrically insulating electrodes

The boiling detector measurement is based on the change in the dielectric properties of the water between two plate-like electrodes when it changes phase from a liquid to a gas. This change in the dielectric results in a change in the electrical impedance between the electrodes. If the electrodes are directly exposed to the water, current will pass directly through the water dependent on its electrical conductivity, which is highly dependent on any potential impurities and thermodynamic state of the water. This effect makes establishing a baseline measurement level very difficult as it is constantly changing. Therefore, a well-designed boiling detector should be predominately sensitive to changes in the dielectric due to the presence of vapor voids. To achieve this goal, the electrodes need to be electrically insulated from the water. Few electrically insulating materials are available that will maintain adherence to the surface of an electrode and are capable of withstanding PWR conditions. Continuing from testing from the previous year, many insulating coatings have been tested under PWR conditions to find a material that will satisfy the design requirement. Results from some of this testing can be seen in Figure 2

The plasma-sprayed ZrO₂ was found to maintain excellent adherence at the end of FY16, however, early in FY17 it was found that it likely retains some porosity which allows water to contact the electrode. Therefore, some attempts were made to improve the coating by adding more layers and looking at additional high temperature materials. These attempts never achieved the desired goal. After testing many potential coatings at PWR conditions for several hours, the Teflon® Ruby Red coating performed well in autoclave testing as shown in the post-test photograph in Figure 2. The coating also maintains excellent electrical isolation of the underlying plate electrodes. The Ruby Red coated plate shown in Figure 2 is built to the dimension that was designed for TREAT deployment.



Figure 2. Post-test photographs of various insulating coatings tested in PWR conditions in an autoclave to determine survivability. From left to right: (1) plasma sprayed ZrO₂ coating (white) with additional impervious layer (gray), (2) Teflon® Ruby Red coating.

3.3 Measurement circuit design

The custom electronic design of the measurement system contains the most unique and critical aspects of the in-pile boiling detector system. Specifically, a unique challenge for in-pile instrumentation is reliably extracting an electric signal through long leads introducing large parasitic capacitance. Overcoming this challenge is especially difficult when small currents and voltages are of interest, as is the case with the impedance measurement in the boiling detector. This subsection discusses some of the key features of the electrical design which enable the ability to perform these in-pile measurements.

Using AC measurement techniques, the choice of excitation frequency is extremely important because it significantly impacts the sensitivity and response time. It also has practical ramifications for the design of system components. For this design, a frequency of 100 kHz was chosen as a tradeoff between providing improved sensitivity to permittivity and finer temporal resolution vs avoiding power transmission frequency regime at higher frequencies.

As discussed earlier, impedance measurements are generally conducted by applying a voltage or current across an electric component and measuring the resulting current or voltage, respectively. Oftentimes, a four-wire configuration (Kelvin sensing) is used where the current loop is composed of two of the wires, and the voltage is measured with the other two. This configuration is often used in LCR meters because it minimizes the effect of the resistance in the measurement leads and contact resistance because (nearly) no current flows into the voltage measurement leads. However, this technique is not well suited for the design

requirements of a remote, in-pile design because of the high capacitance between lead lines. This capacitance acts as an electrical short to a ground providing an alternate path for the current to flow.. In fact, this capacitance would be larger than the capacitance between the measurement electrodes and thus dwarf the sensitivity to the true measurement target of void formation.

To overcome this challenge, custom electronics were developed that minimize the effects of lead capacitance on the measurement. Specifically, the circuit is designed to excite the driver electrode with voltage and measure the current from the pickup electrode. This allows for current to flow from the driver electrode to other ground locations (parasitic capacitance) without effecting the measurement, since only the current flowing through the pickup electrode is measured. With this configuration, the pickup electrode is held at a ground potential along with all other surrounding hardware and components. However, the circuit is isolated from the surrounding hardware through the use of a current-to-voltage amplifier to act as a buffer circuit. This design effectively removes the effect of the capacitance of the pickup lead and the ground shield because they are held at the same potential. The measurement of current on the pickup electrode is a key enabling feature of the system because it removes the influence of the large capacitance of the pickup lead. The complete measurement system diagram can be seen in Figure 3.

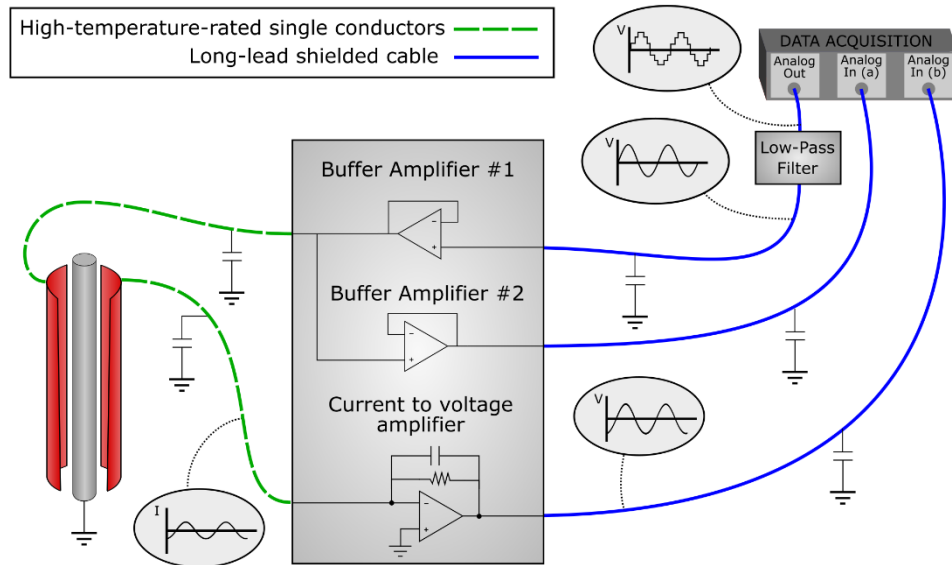


Figure 3 System schematic of electrical circuit design for the in-pile boiling detector system

The measurement system begins with the sinusoidal voltage output at 100 kHz from the data acquisition unit. The sine voltage is composed of discrete levels due to the digital nature of the DAQ. This signal is then processed through a low-pass filter leaving only the lowest 100 kHz frequency. It is then passed to the input of a buffer amplifier. This amplifier is necessary because the data acquisition cannot output enough current to drive the parasitic capacitance of the leads (high-temperature-rated single conductor leads). A second buffer amplifier provides the current to send a reference signal back to the data acquisition. At the sensor location, the current that is induced into the pickup electrode runs into a current-to-voltage amplifier, which sends voltage on to the data acquisition. The amplitude and phase of the pickup voltage compared to the reference (driver voltage) is measured to determine the impedance between the driver and pickup electrodes. After design and testing of the circuit, the custom circuit was fabricated into a circuit board and packaged into complete system allowing for a robust system allowing for simple connection of cables. A photograph of the custom circuit board used in the system can be seen in Figure 4.

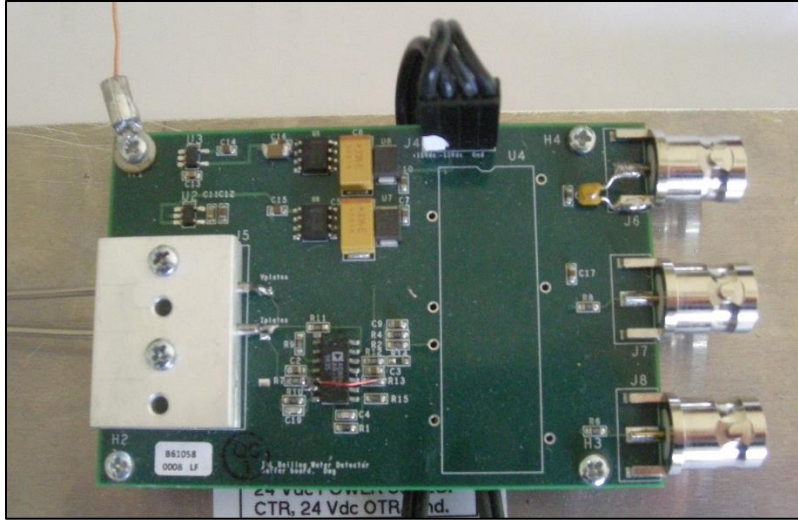


Figure 4 Picture of custom electronics designed for use in the boiling detector measurement system. This electronic box is represented by the large gray box in the center of Figure 3. The three BNC connectors on the right are the connections to the DAQ. The two wires on the left are MgO cables that connect to the driver and pickup electrodes.

An equivalent circuit for the boiling detector can be seen in Figure 5. This diagram illustrates how the measurement system is only sensitive to the current flowing from the driver electrode to the pickup electrode. A key feature of this design deals with the current-to-voltage conversion on the pickup electrode. Since one of the inputs to the amplifier is tied to ground, the other input (connected to the pickup electrode) is also at the ground potential. This results in no voltage potential across Z_3 and Z_4 . Therefore, any current flowing from the driver electrode to the pickup electrode (through Z_5) must then flow through Z_G around the amplifier. The current flowing through the parallel paths of impedances Z_1 and Z_2 do not impact the current flowing through Z_5 . It is important to note that only the current flowing between the two electrodes is measured, and not the total current flowing through the driver electrode (which would be the cases if a Kelvin probe/4 wire approach were used).

The design of this electrical circuit is optimized for performing impedance measurements in a test reactor. Specifically, this design is part of the system for use in PWR RIA experiments in TREAT. However, the design can potentially be directly used or adapted for other applications (e.g. deformation sensors) based on measurement of impedance.

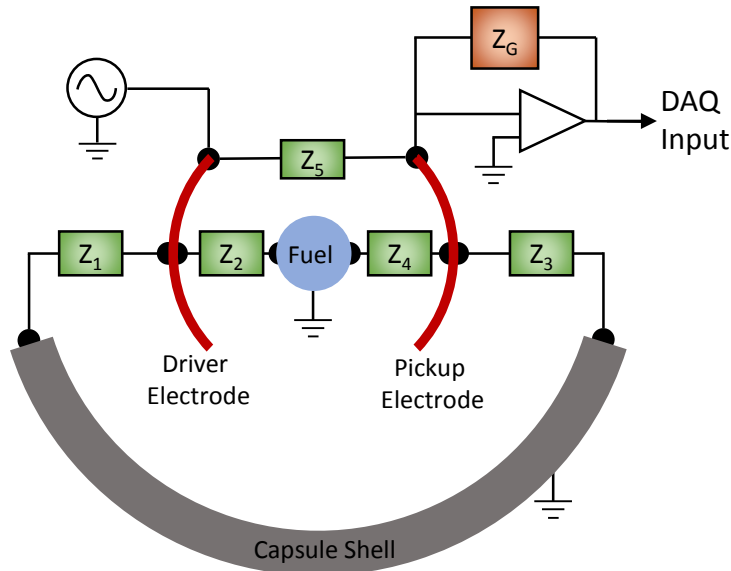


Figure 5 Diagram of equivalent electrical circuit surrounding electrodes.

4. Experimental Setup

Several experimental facilities have been used to study the behavior of the boiling detector. These include simple benchtop studies using beakers to experimental tests in the PWR water autoclaves. To perform detailed characterization of the performance of the boiling detector, a visual boiling station was designed and built in the High Temperature Test Laboratory (HTTL). Figure 6 shows a schematic and photograph of this setup in HTTL. This experimental setup was built using a large custom-built glass cylinder filled with water. An inner glass tube is installed that holds a metallic tube representing the central test fuel rod. A cartridge heater is installed in the inner tube to allow for boiling within the setup. A tube was also installed to allow insertion of measured volumes of air below the sensor region. Additionally, void surrogates using Teflon were used to represent the presence of void in the system. The Teflon was machined to thin tubes to fit on the central rod to study sensitivity to the presence of void film on the central rod. The sensor electrodes may be connected directly to an LCR meter or to the custom measurement electronics and DAS to perform measurements.

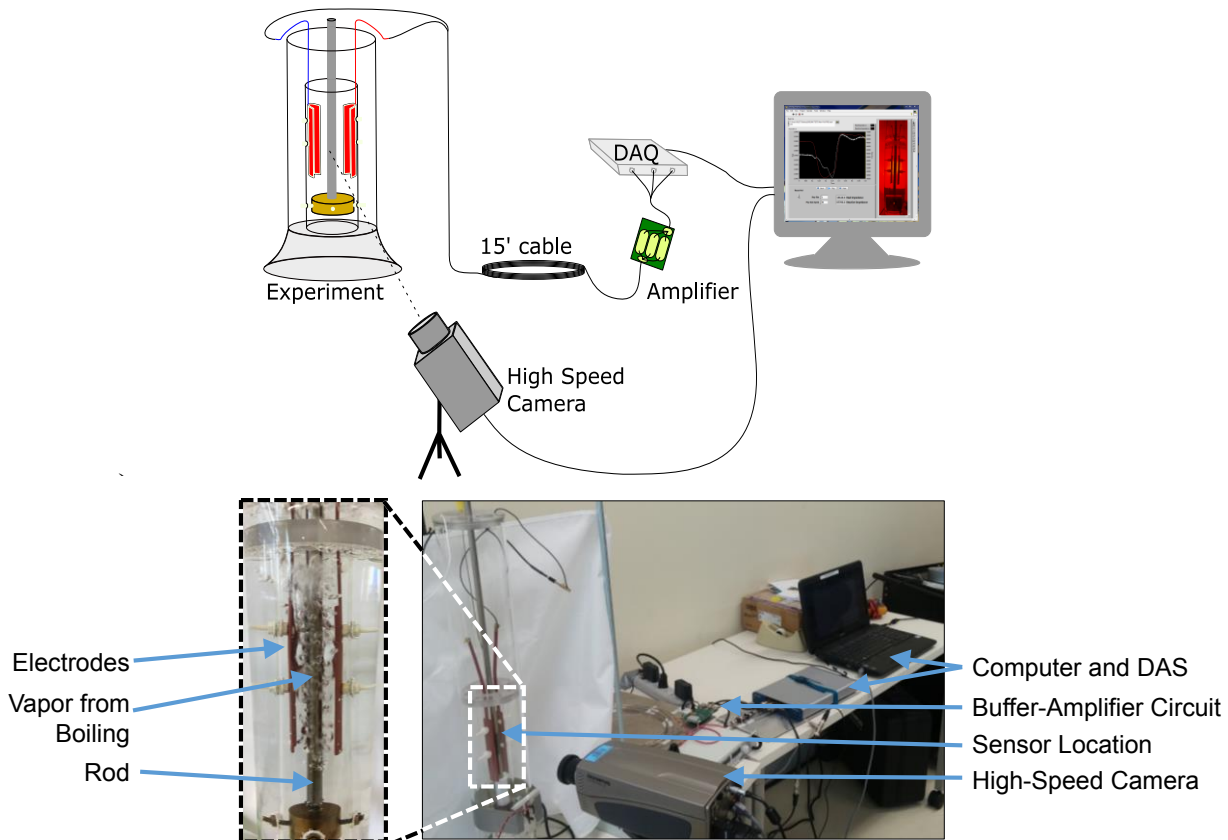


Figure 6. High speed visual boiling setup in HTTL. (a) schematic overview; (b) photograph

Additionally a high speed camera was also installed with backlighting to enable optical visualization at a frame rate of 1000 Hz. The camera was then synced to the impedance measurement through the DAS system to provide images directly correlated measured impedance. This unique system was primarily used to obtain the results in the following section. An example of output from the DAS graphical user interface (GUI) is shown in Figure 7. The marker in the plot of impedance vs time represents the point in time corresponding to the image.

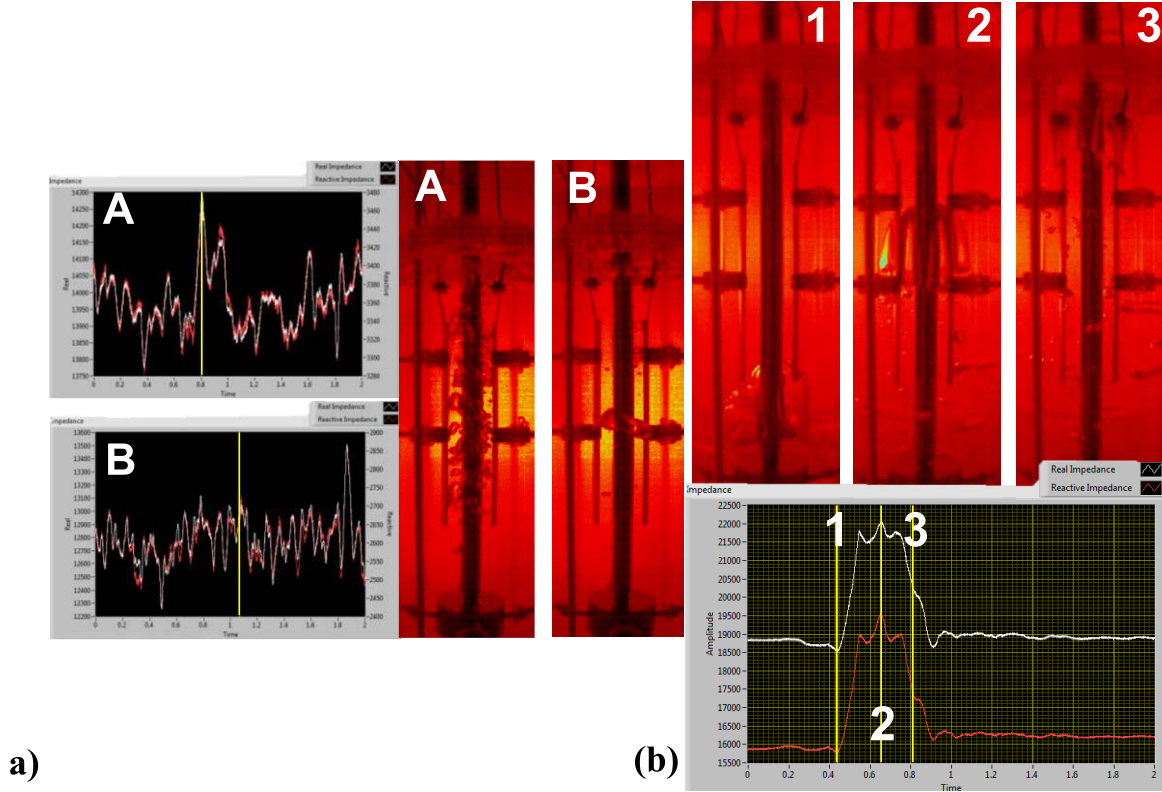


Figure 7. Examples of data taken with high speed visual boiling setup. (a) Boiling; (b) Propagation of an air bubble through sensor region

5. Experimental Results

Many experiments have been conducted to evaluate and characterize the performance of the void sensor. These experiments include a design of experiments factorial, a void-position sensitivity experimental set, and transient tests to investigate system response. The DoX's factorial was chosen in order to efficiently and systematically evaluate the influence of certain parameters on the experimental result and to evaluate the efficacy of the sensor. The position sensitivity experiment set was aimed at determining spatial effects of void sensitivity for the boiling detector, with particular interest in the presence of void film layers on the surface of a fuel rod. The transient experiments were conducted to evaluate the time response of the detector. These experimental sets were chosen because the results are important for the qualification of the instrument to be used for in-pile testing. This section presents and discusses the results from these three sets of experiments.

5.1 Design of experiments

As described in previous sections, an insulative coating was used to reduce the electrical conduction between the sensor electrodes. Even with this feature, there are still many factors that influence the electrical impedance between the electrodes. These factors include geometry and electrical properties of the dielectric media between the electrodes. The geometry of the electrodes and fuel pin were held in fixed positions (as well as experimentally possible) during these tests. These experiments focused on manipulating the electrical properties of the water and other media separating the two electrodes. The operating principle of the boiling detector is based on water vapor having a largely different dielectric constant than liquid water. When a vapor forms, the electric field and thus the electrical coupling between the electrodes is impacted. This design of experiments study was oriented with the goal of determining void detection capability

depending on its size and position and surrounding water temperature. The temperature of the water is a critical consideration because of the strong temperature dependency of the dielectric constant of water. As water subcooling is reduced, its dielectric constant becomes closer to that of vapor, thus reducing sensitivity of the impedance measurement to void formation in the water.

A design of experiments factorial is ideally suited for this study because there are several controllable factors of interest as well as many uncontrollable factors. The test is designed to determine how sensitive the detector is to voids located between the electrodes (essentially the efficacy of the detector). Therefore, the “presence of a void” was used as a factor in the design of experiments. Since the presence of a void is binary in nature (it is either present or not present), a 2^k factorial design was chosen. The factors used in the DoX were the Teflon sleeve thickness, axial position on the surrogate fuel pin, the presence of the sleeve, and the temperature of the surrounding water. The high and low values for these factors can be seen in Table 1. The complex impedance between the electrodes is the measured output from the experiment.

Table 1 Factor levels used in design of experiments

| <i>Factor</i> | <i>Low (-)</i> | <i>High (+)</i> |
|----------------------------------|--------------------------|-----------------------------|
| <i>(A) Sleeve Wall Thickness</i> | <i>0.065"</i> | <i>0.261"</i> |
| <i>(B) Sleeve Axial Location</i> | <i>Top of Electrodes</i> | <i>Center of Electrodes</i> |
| <i>(C) Presence of a Sleeve</i> | <i>Not Present</i> | <i>Present</i> |
| <i>(D) Water Temperature</i> | <i>19° C</i> | <i>70° C</i> |

The design, setup, and evaluation of the design of experiments was conducted in the manner described by Montgomery [19]. The four factors given in Table 1 were used in a 2^4 factorial in which the treatment combinations can be seen in Table 2. Three replications were conducted for each of the 16 treatment combinations resulting in a total of 48 experiments.

Table 2 Table showing the different treatment combinations used in the design of experiments. The negative and positive ones correspond to the low and high levels of that factor, which are provided in Table 1.

| Treatment # | (A) | (B) | (C) | (D) |
|-------------|-----|-----|-----|-----|
| 1 | -1 | -1 | -1 | -1 |
| 2 | 1 | -1 | -1 | -1 |
| 3 | -1 | 1 | -1 | -1 |
| 4 | 1 | 1 | -1 | -1 |
| 5 | -1 | -1 | 1 | -1 |
| 6 | 1 | -1 | 1 | -1 |
| 7 | -1 | 1 | 1 | -1 |
| 8 | 1 | 1 | 1 | -1 |
| 9 | -1 | -1 | -1 | 1 |
| 10 | 1 | -1 | -1 | 1 |
| 11 | -1 | 1 | -1 | 1 |
| 12 | 1 | 1 | -1 | 1 |
| 13 | -1 | -1 | 1 | 1 |
| 14 | 1 | -1 | 1 | 1 |
| 15 | -1 | 1 | 1 | 1 |
| 16 | 1 | 1 | 1 | 1 |

From the experiments the main and interaction effects between factors were calculated. The presence of a void (C) and water temperature (D) effects had the largest influence, followed by the interaction of those two (CD), as can be seen in Table 3. All other interaction effects are insignificant in comparison. The sleeve wall thickness (A) and sleeve axial location (B) influenced the results, but their main effects were measured to be approximately an order of magnitude less than the other factors.

These main and interaction effects are indicative of the sensors ability to detect voids between the electrodes. The presence of a void has the largest impact on the result, nearly a factor of two larger than the effect of temperature. This provides proof of the efficacy of the instrument to detect voids located between the electrodes. These results also show the sensors ability to detect voids is only minimally influenced by the location and size of the void. Therefore, the boiling detector shows a promising capability to detect a vapor film surrounding the fuel rodlet during in-pile testing as may occur in RIA testing.

Table 3 The magnitude of the main and interaction effects calculated from the design of experiments results

| Effect | Amplitude | Phase | Real | Imaginary |
|--------|-----------|---------|----------|-----------|
| A | 2198.8 | 0.0025 | 619.7 | 2148.0 |
| B | 323.6 | 0.0286 | -884.2 | 669.0 |
| AB | -236.2 | 0.0008 | -201.5 | -209.3 |
| C | -26556.0 | -0.2502 | 7431.9 | -28001.2 |
| AC | 2292.4 | 0.0058 | 421.6 | 2234.5 |
| BC | 442.5 | 0.0333 | -1162.4 | 772.8 |
| ABC | -329.8 | -0.0006 | -116.4 | -297.0 |
| D | -13426.4 | 0.1345 | -10055.8 | -12378.7 |
| AD | 190.4 | -0.0034 | 189.8 | 167.1 |
| BD | -94.4 | 0.0092 | -206.9 | -11.8 |
| ABD | 56.2 | 0.0022 | -123.2 | 77.5 |
| CD | 4677.8 | -0.0779 | 5201.2 | 4727.5 |
| ACD | 279.3 | -0.0004 | 13.5 | 245.2 |
| BCD | 21.9 | 0.0142 | -504.5 | 92.8 |
| ABCD | -41.0 | 0.0006 | -26.6 | -15.8 |

In addition to the calculation of the main and interaction effects, an Analysis of Variance (ANOVA) study was conducted for each of the output values. From the ANOVA tables, it was determined that all of the factors main effects in addition to the CD interaction were significant regardless of the output parameter analyzed, see Table 4 through Table 7. Other interaction effects were shown to be significant (AC, BC, AD), but their effects, shown in Table 3, were small compared to the other main effects and the CD interaction. Therefore, while they are statistically significant their influence can be considered negligible compared to the other factors. The rest of the factors (AB, ABC, BD, ABD, ACD, BCD, ABCD) have small influence over the results, and their statistical significance depended on the output parameter chosen.

Table 4 ANOVA table for the impedance amplitude calculated from the design of experiments

| <i>Factor</i> | <i>Sum of Squares</i> | <i>Degrees of Freedom</i> | <i>Mean Square</i> | <i>F₀</i> | <i>p-value</i> |
|---------------|-----------------------|---------------------------|--------------------|----------------------|----------------|
| A | 58014980 | 1 | 58014980.0 | 3613.9 | <0.001 |
| B | 1256750 | 1 | 1256750.2 | 78.3 | <0.001 |
| AB | 669379 | 1 | 669379.5 | 41.7 | <0.001 |
| C | 8462631997 | 1 | 8462631996.5 | 527156.4 | <0.001 |
| AC | 63060699 | 1 | 63060698.7 | 3928.2 | <0.001 |
| BC | 2349415 | 1 | 2349414.6 | 146.4 | <0.001 |
| ABC | 1305516 | 1 | 1305515.5 | 81.3 | <0.001 |
| D | 2163218311 | 1 | 2163218311.2 | 134751.8 | <0.001 |
| AD | 435224 | 1 | 435224.4 | 27.1 | <0.001 |
| BD | 106990 | 1 | 106990.3 | 6.7 | 0.01462 |
| ABD | 37956 | 1 | 37956.2 | 2.4 | 0.13396 |
| CD | 262586228 | 1 | 262586228.2 | 16357.1 | <0.001 |
| ACD | 936220 | 1 | 936220.2 | 58.3 | <0.001 |
| BCD | 5767 | 1 | 5766.9 | 0.4 | 0.55315 |
| ABCD | 20214 | 1 | 20213.8 | 1.3 | 0.27016 |
| Error | 513708 | 32 | 16053.4 | 1.3 | |
| Total | 11017149354 | 47 | | | |

Table 5 ANOVA table for the phase of the impedance calculated from the design of experiments

| <i>Factor</i> | <i>Sum of Squares</i> | <i>Degrees of Freedom</i> | <i>Mean Square</i> | <i>F₀</i> | <i>p-value</i> |
|---------------|-----------------------|---------------------------|--------------------|----------------------|----------------|
| A | 0.000 | 1 | 0 | 10.40 | 0.0029 |
| B | 0.010 | 1 | 0.01 | 1310.87 | <0.001 |
| AB | 0.000 | 1 | 0 | 1.15 | 0.2925 |
| C | 0.750 | 1 | 0.75 | 100583.31 | <0.001 |
| AC | 0.000 | 1 | 0 | 54.88 | <0.001 |
| BC | 0.010 | 1 | 0.01 | 1782.74 | <0.001 |
| ABC | 0.000 | 1 | 0 | 0.49 | 0.48784 |
| D | 0.220 | 1 | 0.22 | 29047.69 | <0.001 |
| AD | 0.000 | 1 | 0 | 18.45 | 0.00015 |
| BD | 0.000 | 1 | 0 | 135.98 | <0.001 |
| ABD | 0.000 | 1 | 0 | 7.71 | 0.00911 |
| CD | 0.070 | 1 | 0.07 | 9759.40 | <0.001 |
| ACD | 0.000 | 1 | 0 | 0.24 | 0.62578 |
| BCD | 0.000 | 1 | 0 | 323.99 | <0.001 |
| ABCD | 0.000 | 1 | 0 | 0.64 | 0.42941 |
| Error | 0.000 | 32 | 0 | 0.64 | |
| Total | 1.070 | 47 | | | |

Table 6 ANOVA table for the real impedance calculated from the design of experiments

| <i>Factor</i> | <i>Sum of Squares</i> | <i>Degrees of Freedom</i> | <i>Mean Square</i> | <i>F₀</i> | <i>p-value</i> |
|---------------|-----------------------|---------------------------|--------------------|----------------------|----------------|
| A | 4607641 | 1 | 4607641.0 | 189.52 | <0.001 |
| B | 9382104 | 1 | 9382104.1 | 385.91 | <0.001 |
| AB | 487058 | 1 | 487058.3 | 20.03 | <0.001 |
| C | 662788755 | 1 | 662788754.6 | 27262.31 | <0.001 |
| AC | 2133326 | 1 | 2133326.1 | 87.75 | <0.001 |
| BC | 16214834 | 1 | 16214833.6 | 666.96 | <0.001 |
| ABC | 162554 | 1 | 162554.3 | 6.69 | 0.01447 |
| D | 1213432328 | 1 | 1213432327.9 | 49911.78 | <0.001 |
| AD | 432503 | 1 | 432502.8 | 17.79 | 0.00019 |
| BD | 513485 | 1 | 513484.7 | 21.12 | <0.001 |
| ABD | 182026 | 1 | 182026.3 | 7.49 | 0.01005 |
| CD | 324635886 | 1 | 324635886.5 | 13353.16 | <0.001 |
| ACD | 2195 | 1 | 2194.8 | 0.09 | 0.76577 |
| BCD | 3054556 | 1 | 3054555.6 | 125.64 | <0.001 |
| ABCD | 8520 | 1 | 8519.9 | 0.35 | 0.55802 |
| Error | 777969 | 32 | 24311.5 | 0.35 | |
| Total | 2238815740 | 47 | | | |

Table 7 ANOVA table for the impedance real impedance calculated from the design of experiments

| <i>Factor</i> | <i>Sum of Squares</i> | <i>Degrees of Freedom</i> | <i>Mean Square</i> | <i>F₀</i> | <i>p-value</i> |
|---------------|-----------------------|---------------------------|--------------------|----------------------|----------------|
| A | 55365025 | 1 | 55365025.0 | 3701.25 | <0.001 |
| B | 5370105 | 1 | 5370104.8 | 359.00 | <0.001 |
| AB | 525531 | 1 | 525530.7 | 35.13 | <0.001 |
| C | 9408791537 | 1 | 9408791537.2 | 628995.03 | <0.001 |
| AC | 59915387 | 1 | 59915387.1 | 4005.45 | <0.001 |
| BC | 7167428 | 1 | 7167428.4 | 479.16 | <0.001 |
| ABC | 1058598 | 1 | 1058598.5 | 70.77 | <0.001 |
| D | 1838788799 | 1 | 1838788798.6 | 122926.42 | <0.001 |
| AD | 335109 | 1 | 335108.9 | 22.40 | <0.001 |
| BD | 1683 | 1 | 1683.4 | 0.11 | 0.73947 |
| ABD | 72127 | 1 | 72127.3 | 4.82 | 0.03547 |
| CD | 268188485 | 1 | 268188484.9 | 17928.89 | <0.001 |
| ACD | 721219 | 1 | 721219.3 | 48.21 | <0.001 |
| BCD | 103293 | 1 | 103293.5 | 6.91 | 0.01309 |
| ABCD | 3006 | 1 | 3006.3 | 0.20 | 0.65696 |
| Error | 478670 | 32 | 14958.5 | 0.20 | |
| Total | 11646886004 | 47 | | | |

5.2 Position sensitivity

From the design of experiments, it was shown the boiling detector was much more sensitive to the presence of a void and the water temperature than the position of the void. While it is obvious the void should be in close proximity to the electrodes, it was unclear how much influence the axial location of a void would have on the impedance measured by the system. In order to explore this aspect of the detector, a set of experiments was conducted to determine how the variation of impedance with axial position of a void. Similar to the design of experiments, a Teflon sleeve was used to simulate a gas film on the rodlet, having a wall thickness of 0.261" and 2" long. Impedance measurements were conducted with this Teflon sleeve at various axial positions along the rodlet. The measured impedance results from these tests can be seen in Figure 9. The "0" position is where the Teflon sleeve is resting on the brass piece holding the rodlet at the bottom.

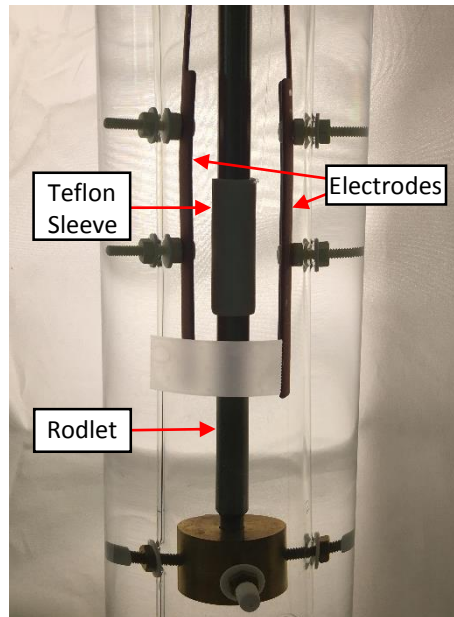


Figure 8 Photograph of experimental setup with the rodlet, Teflon sleeve and electrodes labeled.

Results show the imaginary component (influenced by capacitance) of the impedance is impacted more significantly than the real components. As predicted there is a symmetry to the position of the void as it starts below the electrodes, centered between the electrodes, and then is located above the electrodes. Some asymmetry can be seen in the plot presented in Figure 9. This is explained through the asymmetry in the electrode geometry. The "stem" of the electrode that leads out of the water acts as part of the electrode.

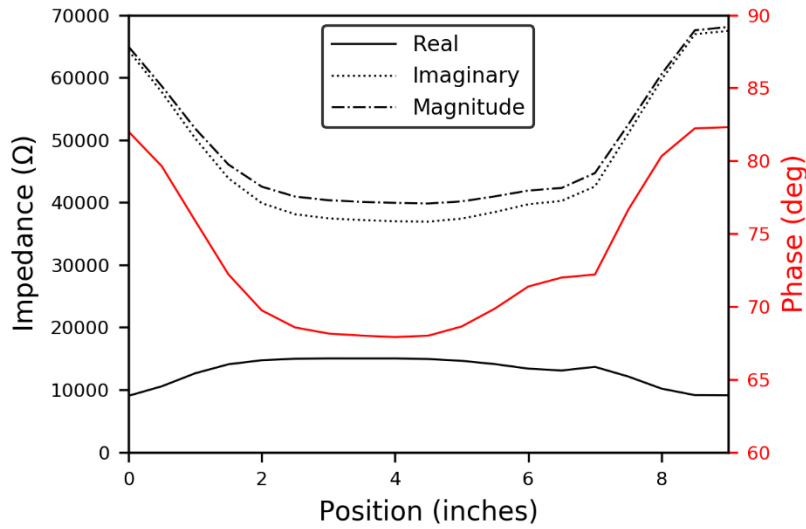


Figure 9 Measured electrical impedance between the sensor electrodes. The impedance is provided in both the imaginary and real components and alternatively as the magnitude and phase.

5.3 Transient Experiments

Significant effort was made in characterizing the time response of the detector. These tests were done using a Teflon sleeve that was quickly moved axially along the surrogate fuel pin. The Teflon sleeve began positioned centered between the bottom and top of the electrodes. The Teflon sleeve was quickly pulled from that position to a position far above the electrodes. This test was performed to simulate a step change in the dielectric properties of the material between the electrodes. From this step change the response time can be determined. This process was recorded with the use of a high speed camera such that the duration of the event can be easily recorded. This experiment is described in Figure 10 which shows the beginning and ending positions of the Teflon sleeve, respective to the electrodes.

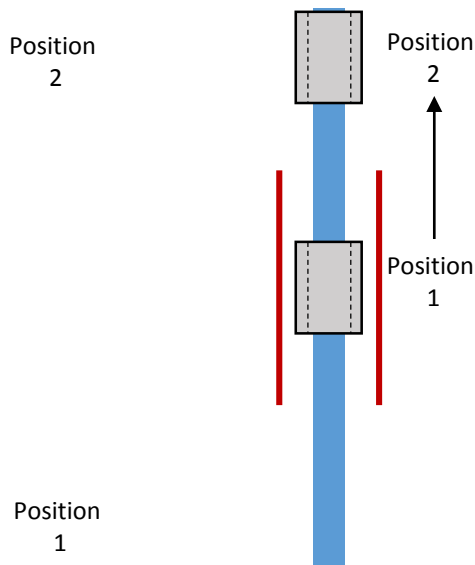


Figure 10 Diagram of the transient experiments performed to characterize the response time of the detector.

A thin monofilament nylon string was attached to the Teflon sleeve and rapidly pulled to move the Teflon sleeve from position 1 to position 2. These transient tests were conducted several times under the observation of a high speed camera. The temporal response of the detector was similar in all of the cases. A characteristic response of the system can be seen in Figure 11. The average time the Teflon sleeve took to move from position 1 to position 2 was 46 mS.

Some significant limitations for this test were found due to the fact that the position of the Teflon sleeve is not the only factor impacting the impedance between the electrodes. For example, the temperature and pressure of the water significantly impact its dielectric. The motion of the Teflon sleeve significantly mixes the water which can affect the impedance depending on the concentration of impurities or thermodynamic states at different locations. Even with these possible sources of error, important information can be obtained from the results shown in Figure 11. The first noticeable change in the impedance is seen around 6.7 seconds, and the system settles on a value at around 6.777 second. This results in a total response time of approximately 77 mS. This response time is approximately 30 mS longer than expected from the results seen in the high speed camera. The high speed camera measured a Teflon sleeve movement duration of 48 mS for the data set shown in Figure 11. In the first 48-50 mS after the transient began (6.7-6.75 s), the data increases to a value, and then appears to level off at a value before rapidly changing over the next 25 to 30 mS.

This initial transient is suspected to be due to the removal of the Teflon sleeve. While the cause of the large change at the end of transient is unknown, there are several possibilities. One possibility is the redistribution of ions in the water after the Teflon is removed. Several measurements were conducted, and all curves exhibited the same initial increasing period which appeared to level off corresponding to the duration of the Teflon removal followed by a rapid increase. All of the electronic components in the system respond much faster than any of the transients under measurement in this experiment. Therefore, it has been concluded that the measurement contains information about the actual impedance observed, likely influenced by water movement, and is not a limitation of the measurement system itself.

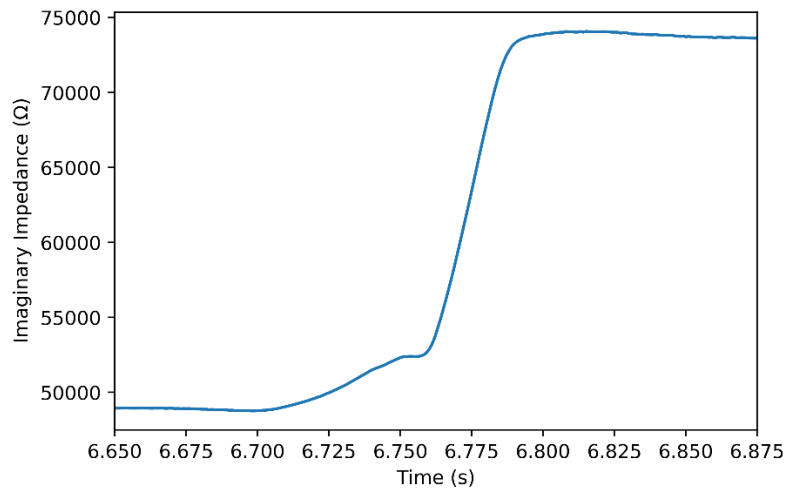


Figure 11 Measured imaginary impedance from the void sensor while the Teflon sleeve is moved from position 1 to position 2 as described in Figure 10

6. Summary & Conclusions

A complete boiling detector measurement system has been designed and built including sensor, electrical circuit design and setup, and data acquisition and processing software that will interface with the TREAT experiment DAS. The development and qualification of the boiling detector has progressed to an advanced stage of testing to characterize its performance using a unique, high-speed video boiling setup. An electrically insulating coating has been established through performance evaluation for use at PWR water conditions of a capsule-based experiment. This coating provides a significant enhancement of the sensor design by increasing the sensitivity of the detector to changes in the effective dielectric by reducing the sensitivity to water conductivity. A complete, packaged in-pile impedance measurement system has been designed, tested, and is now available for supporting TREAT experiments. This system is uniquely designed for in-pile use. Detailed performance characterization studies have been performed based on a design of experiments. Results quantitatively show the sensor is influenced most by the presence of a void and has significant sensitivity to the temperature of the water. Using a Teflon sleeve as a void film surrogate, good sensitivity was found when the film is located anywhere between the electrodes on the pin, with marginal sensitivity above and below the electrodes. Finally the transient response of the sensor was experimentally explored using the high speed video and quick removal of a Teflon sleeve. Though the results were not entirely conclusive, based on some assumptions, the results from this test indicate response time < 1 ms.

The boiling detector has been developed to a high level of maturity, capable of detecting changes in the dielectric properties of the material located between the electrodes. Some theoretical limitations of the instrument remain. Specifically, since the impedance is the measured quantity, any factor influencing the impedance introduces uncertainty on detecting boiling. In the interpretation of the results, all other measured data should be considered. Therefore, if the boiling detector results can be analyzed with the use of additional information, such as water temperature, more reliable results can be obtained.

Future work should continue sensor characterization to provide improved interpretation of measured results possibly providing additional information about void structure and/or void fractions. Though not reported here, finite element models of the experimental setup have been built and preliminary results show reasonable agreement with experimental results. Still, quantitative interpretation of the measurements will require more systematic investigation to quantify the impact of all contributing influences described in this report.

7. References

- [1] Beck, W., et al., Nuclear Fuel Safety Criteria Technical Review. 2 ed. 2012.
- [2] Fuangworawong, N. Local void fraction measurement by using reflected ultrasonic intensity and wire mesh tomography in air-water bubbly flow. 2007.
- [3] Hu, B., et al., Development of an X-ray computed tomography (CT) system with sparse sources: application to three-phase pipe flow visualization. *Experiments in fluids*, 2005. 39(4): p. 667-678.
- [4] Kendoush, A.A. and Z.A. Sarkis, Void fraction measurement by X-ray absorption. *Experimental thermal and fluid science*, 2002. 25(8): p. 615-621.
- [5] Buell, J., et al., A neutron scatterometer for void-fraction measurement in heated rod-bundle channels under CANDU LOCA conditions. *International journal of multiphase flow*, 2005. 31(4): p. 452-472.
- [6] Majors, P.D., R. Givler, and E. Fukushima, Velocity and concentration measurements in multiphase flows by NMR. *Journal of Magnetic Resonance* (1969), 1989. 85(2): p. 235-243.
- [7] Kiambi, S., et al., Measurements of bubble characteristics: comparison between double optical probe and imaging. *The Canadian Journal of Chemical Engineering*, 2003. 81(3-4): p. 764-770.

- [8] Fossa, M., Design and performance of a conductance probe for measuring the liquid fraction in two-phase gas-liquid flows. *Flow Measurement and Instrumentation*, 1998. 9(2): p. 103-109.
- [9] Song, C.-H., M.K. Chung, and H.C. No, Measurements of void fraction by an improved multi-channel conductance void meter. *Nuclear Engineering and Design*, 1998. 184(2): p. 269-285.
- [10] AESJ, *Advanced Measurement in Multiphase Flow*, ed. AESJ. 2003: Morikita Publishing Co., Ltd.
- [11] Xie, C., et al., Design of capacitance electrodes for concentration measurement of two-phase flow. *Measurement Science and Technology*, 1990. 1(1): p. 65.
- [12] Cimorelli, L. and R. Evangelisti, The application of the capacitance method for void fraction measurement in bulk boiling conditions. *International Journal of Heat and Mass Transfer*, 1967. 10(3): p. 277-288.
- [13] Reinecke, N. and D. Mewes, Recent developments and industrial/research applications of capacitance tomography. *Measurement Science and Technology*, 1996. 7(3): p. 233.
- [14] Abouelwafa, M.S.A. and E.J.M. Kendall, The use of capacitance sensors for phase percentage determination in multiphase pipelines. *Instrumentation and Measurement, IEEE Transactions on*, 1980. 29(1): p. 24-27.
- [15] Shu, M.T., C.B. Weinberger, and Y.H. Lee, A simple capacitance sensor for void fraction measurement in two-phase flow. *Industrial & Engineering Chemistry Fundamentals*, 1982. 21(2): p. 175-181.
- [16] Huang, S., *Capacitance transducers for concentration measurement in multi-component flow processes*. 1986, University of Manchester, Institute of Science and Technology.
- [17] Ceccio, S. and D. George, A review of electrical impedance techniques for the measurement of multiphase flows. *Journal of fluids engineering*, 1996. 118(2): p. 391-399.
- [18] Strizzolo, C.N. and J. Converti, *Capacitance sensors for measurement of phase volume fraction in two-phase pipelines*. *Instrumentation and Measurement, IEEE Transactions on*, 1993. 42(3): p. 726-729.
- [19] Montgomery, D.C., *Design and Analysis of Experiments* John Wiley & Sons (1996)